Technische Universität München
TUM School of Natural Sciences

Advancing Superconducting Nanowire Single-Photon Detectors via Helium Ion Irradiation

Stefan Strohauer

Vollständiger Abdruck der von der TUM School of Natural Sciences der Technischen Universität München zur Erlangung eines

Doktors der Naturwissenschaften (Dr. rer. nat.)

genehmigten Dissertation.

Vorsitz: Prof. Dr. Frank Pollmann

Prüfende der Dissertation:
1. Prof. Jonathan J. Finley, Ph.D.
2. Prof. Dr. Stefan Filipp

Die Dissertation wurde am 09.05.2025 bei der Technischen Universität München eingereicht und durch die TUM School of Natural Sciences am 25.06.2025 angenommen.

To my parents and in memory of my grandfather.

"It's not what you look at that matters, it's what you see."

— Henry David Thoreau

Abstract

Superconducting nanowire single-photon detectors (SNSPDs) have revolutionized numerous scientific and technological fields such as quantum science, astronomy, optical communication, biology, and medicine. With their ability to detect single photons with near-unity efficiency, subhertz dark count rates, picosecond timing resolution, and nanosecond reset times, these detectors have become indispensable tools for demanding applications such as photonic quantum computing, lidar, particle and dark matter detection, or infrared fluorescence microscopy for in vivo deep brain imaging. This thesis introduces local helium (He) ion irradiation as a versatile tool to engineer detector properties with nanoscale resolution to further advance photon detection efficiency, lower dark count rate, as well as improve timing jitter and the homogeneity of device performance in SNSPD arrays. We present three interconnected studies in which we develop novel irradiation strategies that fundamentally improve SNSPD performance and provide new insights into the physical mechanisms underlying these enhancements.

Firstly, we demonstrate site-selective He ion irradiation for post-fabrication tuning of individual detectors on the same chip. This approach transforms thick-film (12 nm) niobium titanium nitride (NbTiN) detectors from a detection efficiency of less than 0.05 % to $> 55\,\%$ following irradiation with 1800 ions nm^{-2}, while enabling individual tuning of detector properties to achieve uniform performance across detector arrays. Moreover, we develop a physical model accounting for defect generation and sputtering during irradiation, which shows good qualitative agreement with the experimental evolution of sheet resistance and critical temperature with the He ion fluence.

Building upon this foundation, we advance beyond full-device irradiation to address the persistent challenge of current crowding in meander-shaped SNSPDs. By selectively irradiating only the straight nanowire segments while leaving the bends unirradiated, we overcome performance limitations that remain even after full-device irradiation. Once the He ion fluence is sufficiently high, the critical current of the irradiated straight segments becomes lower than that of the bends. This effectively eliminates current crowding as a limiting factor. With this refined strategy, we observe an increase in the relative plateau width of saturating detection efficiency from 10 % to 37 % when comparing fully and locally irradiated devices at the same fluence of 2000 ions nm^{-2}, while maintaining higher critical currents. As a result, this larger operating range enables ultra-low dark count rates of 7 mHz at 94 % internal detection efficiency.

To understand the underlying physical mechanisms of the performance enhancement, we investigate how He ion irradiation modifies both the NbTiN film and the underlying SiO_2/Si substrate through comprehensive material characterization and transport measurements. Surprisingly, while the NbTiN film crystallinity remains largely unchanged, the irradiation transforms the crystalline Si substrate into an amorphous structure and creates He bubbles below the SiO_2/Si interface. These modifications substantially reduce the thermal conductance between film and substrate from 210 $W\,m^{-2}\,K^{-4}$ to 70 $W\,m^{-2}\,K^{-4}$ after irradiation with 2000 ions nm^{-2}, which plays a crucial role in enhancing detector sensitivity. By selectively irradiating only regions adjacent to the nanowire, we use the lateral ion straggle to modify the thermal properties beneath the wire whilst minimizing direct interaction with the superconducting film itself. This allows us to achieve enhanced sensitivity while maintaining high critical currents.

The three irradiation techniques developed in this thesis—which enable site-selective enhancement, current crowding elimination, and thermal conductance engineering—can be strategically combined to achieve complementary benefits and provide a comprehensive toolkit for optimizing SNSPD performance metrics such as detection efficiency, dark count rate, and timing jitter. Taken together, these studies establish local He ion irradiation as a powerful approach for advancing SNSPD technology through both direct modification of the superconducting properties and strategic control of the thermal conductance from the detector to the substrate. The irradiation strategies and physical insights presented here open new pathways for designing next-generation single-photon detectors with unprecedented performance for applications in diverse fields such as quantum information, astronomy, and biomedical imaging, while potentially inspiring similar approaches for other superconducting and quantum devices.

Zusammenfassung

Supraleitende Nanodraht-Einzelphotonendetektoren (SNSPDs) haben zahlreiche wissenschaftliche und technologische Bereiche wie die Quantenwissenschaft, Astronomie, optische Kommunikation, Biologie und Medizin revolutioniert. Mit ihrer Fähigkeit, einzelne Photonen mit einer Effizienz nahe 100 %, Dunkelzählraten unter einem Hertz, Zeitauflösung im Pikosekundenbereich und Reset-Zeiten im Nanosekundenbereich zu detektieren, sind diese Detektoren für anspruchsvolle Anwendungen wie photonisches Quantencomputing, Lidar, Detektion von Teilchen und Dunkler Materie, oder Infrarot-Fluoreszenzmikroskopie zur in vivo-Bildgebung tiefer Hirnstrukturen unverzichtbar geworden. Diese Dissertation führt lokale Helium (He)-Ionen-Bestrahlung als vielseitiges Werkzeug zur gezielten Modifikation von Detektoreigenschaften auf Nanometerskala ein, um die Photonendetektionseffizienz weiter zu steigern, die Dunkelzählrate zu senken, sowie die Zeitauflösung und die Homogenität der Detektorleistung in SNSPD-Arrays zu verbessern. Wir präsentieren drei eng miteinander verwobene Studien, in denen wir neuartige Bestrahlungsstrategien entwickeln, die die Leistung von SNSPDs grundlegend erhöhen und neue Erkenntnisse über die zugrunde liegenden physikalischen Mechanismen dieser Verbesserungen liefern.

Zunächst demonstrieren wir die ortsselektive He-Ionen-Bestrahlung zur Nachbearbeitung einzelner Detektoren auf demselben Chip. Diese Methode erhöht für dicke (12 nm) NbTiN-SNSPDs die Detektionseffizienz von weniger als 0.05 % auf > 55 % nach Bestrahlung mit 1800 ions nm^{-2}, und ermöglicht gleichzeitig die individuelle Anpassung der Detektoreigenschaften für eine gleichmäßige Leistung über Detektor-Arrays hinweg. Außerdem entwickeln wir ein physikalisches Modell, das Sputtern sowie die Generierung von Defekten während der Bestrahlung berücksichtigt und gute qualitative Übereinstimmung mit dem experimentellen Verlauf von Flächenwiderstand und kritischer Temperatur mit dem He-Ionen-Fluss zeigt.

Aufbauend auf diesen Erkenntnissen gehen wir über die vollständige Bestrahlung von Detektoren hinaus und widmen uns der Herausforderung der Stromverdichtung in mäanderförmigen SNSPDs. Indem wir selektiv nur die geraden Nanodraht-Segmente bestrahlen und die Biegungen unbestrahlt lassen, überwinden wir Leistungsbeschrän-

kungen, die auch nach der Bestrahlung des gesamten Detektors bestehen bleiben. Sobald der He-Ionen-Fluss ausreichend hoch ist, wird der kritische Strom der bestrahlten geraden Segmente niedriger als der der Biegungen. Als Folge dessen ist die Stromverdichtung in den Biegungen dann kein limitierender Faktor der Detektorleistung mehr. Diese verfeinerte Strategie erhöht die relative Plateaubreite saturierender Detektionseffizienz von 10 % auf 37 %, wenn man vollständig und lokal bestrahlte Detektoren bei demselben He-Ionen-Fluss von 2000 ions nm^{-2} vergleicht, wobei gleichzeitig höhere kritische Ströme erhalten bleiben. Dieser größere Betriebsbereich ermöglicht ultra-niedrige Dunkelzählraten von 7 mHz bei 94 % interner Detektionseffizienz.

Um die zugrunde liegenden physikalischen Mechanismen zu verstehen, untersuchen wir mittels umfassender Materialcharakterisierung und Transport-Messungen, wie He-Ionen-Bestrahlung den NbTiN-Film und das darunterliegende SiO_2/Si-Substrat verändert. Während die Kristallinität des Films überraschenderweise größtenteils unverändert bleibt, wandelt die Bestrahlung das kristalline Si-Substrat in eine amorphe Struktur um und erzeugt He-Blasen unter der SiO_2/Si-Grenzfläche. Diese Modifikationen reduzieren die thermische Leitfähigkeit zwischen Film und Substrat erheblich von 210 $W\,m^{-2}\,K^{-4}$ auf 70 $W\,m^{-2}\,K^{-4}$ nach Bestrahlung mit 2000 ions nm^{-2}, was eine entscheidende Rolle bei der Verbesserung der Detektorempfindlichkeit spielt. Durch selektive Bestrahlung der an den Nanodraht angrenzenden Regionen und unter Ausnutzung der lateralen Streuung der He-Ionen im Substrat, modifizieren wir die thermischen Eigenschaften unter dem Nanodraht und minimieren gleichzeitig die direkte Wechselwirkung der Ionen mit dem supraleitenden Film. Dies ermöglicht eine erhöhte Sensitivität unter Beibehaltung hoher kritischer Ströme.

Die drei in dieser Arbeit entwickelten Bestrahlungstechniken – die erlauben, Detektoren ortsselektiv zu verbessern, das Problem der Stromverdichtung zu beseitigen, sowie die thermische Leitfähigkeit gezielt zu modifizieren – können strategisch kombiniert werden, um komplementäre Vorteile zu erzielen, und bieten ein umfassendes Instrumentarium zur Optimierung von SNSPD-Leistungsmetriken wie Detektionseffizienz, Dunkelzählrate und Zeitauflösung. Zusammen etablieren diese Ergebnisse die lokale He-Ionen-Bestrahlung als leistungsfähigen Ansatz zur Weiterentwicklung der SNSPD-Technologie durch direkte Modifikation der supraleitenden Eigenschaften und strategische Kontrolle der thermischen Leitfähigkeit. Die hier vorgestellten Bestrahlungsstrategien und physikalischen Erkenntnisse eröffnen neue Möglichkeiten für die Entwicklung von Einzelphotonendetektoren der nächsten Generation mit beispielloser Leistung für Anwendungen in den verschiedensten Bereichen wie der Quanteninformation, Astronomie, sowie der biomedizinischen Bildgebung, und könnten als Inspiration für ähnliche Ansätze bei anderen Supraleitungs- und Quanten-Bauelementen dienen.

Contents

1 Introduction

Imagine a world where we can see individual cells in the brain, detect the faintest signals from deep space, or transmit unbreakable encrypted messages. These scenarios, once confined to science fiction, are now reality thanks to single-photon detection technology [1–8]. At the forefront of this technology are superconducting nanowire single-photon detectors (SNSPDs), which excel at detecting individual light particles with unprecedented efficiency and temporal resolution. This thesis presents novel methods to enhance these detectors through precisely controlled He ion irradiation, addressing longstanding challenges while unlocking new capabilities for applications in quantum technologies, astronomical observation, and biomedical imaging.

1.1 Applications and requirements of single-photon detection

The ability to detect individual photons has revolutionized numerous fields of science and technology. In quantum science and technology, single-photon detectors form the cornerstone for quantum key distribution [6–8], enabling secure communication through the detection of quantum states of light. Moreover, they are essential components in quantum computing [9–16], where quantum states must be measured with high fidelity. In astronomy, these detectors enable breakthrough observations by capturing the faintest signals from space [5] and are crucial components in deep space optical communication systems [4, 17, 18]. The detection of individual photons has also opened new frontiers in biomedical research, particularly in deep-brain imaging [1–3], where *in vivo* non-invasive imaging with cellular resolution requires high sensitivity to infrared fluorescence signals. Moreover, these detectors play an increasingly important role in fundamental physics, from dark matter searches [19, 20] to particle detection [21–23], where their exceptional sensitivity enables the observation of extremely rare events.

The common thread linking these diverse applications is their reliance on detecting extremely weak light signals—often at the single-photon level. For instance, in quantum key distribution, the security of the communication protocol depends on the ability to reliably detect individual photons that may have traveled through hundreds of kilometers of optical fiber [6–8]. Similarly, in deep-brain imaging, infrared photons from fluorescent markers must be detected with high efficiency at wavelengths beyond reach of conventional InGaAs detectors [1–3].

The diverse demands of these applications drive stringent requirements for single-photon detection technologies. Dark matter detection experiments require exceptionally low false detection rates to distinguish rare events from background noise [19, 20], while quantum key distribution demands high detection efficiency to ensure secure data transmission [24–26]. Meanwhile, biomedical imaging relies on efficient single-photon detection at infrared wavelengths to enable deep tissue penetration [1–3].

In general, single-photon detectors have several key performance metrics that are typically used for comparison and for rating their suitability for certain applications. Firstly, they must offer near-unity detection efficiency to capture the maximum number of incoming photons, particularly crucial for quantum computing and long-distance quantum communication where every photon counts [9, 24]. Secondly, they require extremely low dark count rates, often below 1 Hz, to minimize false detection events that could compromise measurement accuracy or communication security [19, 20, 25, 27]. Thirdly, timing resolution in the picosecond range is essential for applications requiring precise photon arrival times, such as quantum key distribution and lidar systems [28]. Finally, a fast reset time in the nanosecond range enables high-speed operation, critical for practical implementation in quantum computing and optical communication systems [29–31].

Meeting all of these requirements simultaneously in a single detection platform presents significant technical challenges. This has driven continuous innovation in single-photon detection technology, particularly in the development of superconducting devices that have achieved unprecedented performance metrics. SNSPDs offer near-unity detection efficiency even at infrared wavelengths, sub-Hz dark count rates, picosecond timing resolution, and nanosecond reset times [27–29, 32, 33]. Moreover, they can be integrated into complex photonic circuits [11, 12] and arranged into detector arrays containing hundreds or thousands of pixels [34, 35].

1.2 Evolution of single-photon detection technology

The quest for high-performance single-photon detection has a rich history, spanning several decades. Early technologies such as photomultiplier tubes (PMTs) enabled the first single-photon measurements through electron multiplication, while the subsequently developed semiconductor-based avalanche photodiodes (APDs) and single-photon avalanche diodes (SPADs) offer more compact solutions, and transition edge sensors (TESs) provide higher detection efficiency. However, these technologies face limitations in key metrics such as detection efficiency at infrared wavelengths, timing resolution, and dark count rate [36].

A breakthrough came in 2001, when Gol'tsman and colleagues demonstrated the first SNSPD [37]. Their device consisted of an ultrathin niobium nitride (NbN) nanowire that, when biased with a current close to its critical current, becomes normal conducting upon absorbing a single photon. This transition generates a voltage pulse that can be detected by room temperature electronics. This elegant detection mechanism, which utilizes the unique properties of superconducting materials, enables exceptional performance across multiple metrics simultaneously.

The development of SNSPDs has been marked by continuous innovation in materials and design. Following the initial demonstration with NbN, researchers explored alternative superconductors including niobium titanium nitride (NbTiN) [38], tungsten silicide (WSi) [39, 40], molybdenum germanium (MoGe) [41], and molybdenum silicide (MoSi) [42]. Each material brings distinct advantages: while polycrystalline materials like NbN and NbTiN offer higher operating temperatures and lower timing jitter, amorphous materials such as WSi and MoSi provide better fabrication uniformity and higher sensitivity to long-wavelength photons. Recent work has even demonstrated SNSPDs sensitive to single photons at a wavelength of 1550 nm and a temperature of 20 K using magnesium diboride (MgB_2) [43], expanding the potential for practical applications.

Integration of SNSPDs into complex photonic systems represents another major advancement. The development of waveguide-integrated detectors enables their use in integrated photonic circuits [11], crucial for quantum information applications. Meanwhile, advances in fiber coupling have simplified interfacing with external light sources, and integration with optical cavities has boosted detection efficiencies [44–46]. These integration capabilities, combined with the exceptional performance metrics of SNSPDs, have established them as a key technology for quantum and classical photonic systems.

Looking towards future applications such as dark matter and particle detection, space-based astronomy, and quantum imaging that require large SNSPD arrays, scaling up to large detector arrays presents significant challenges. One major hurdle is the readout architecture: traditional approaches require individual radio frequency (RF) lines for each detector, making it impractical to scale to thousands or millions of pixels due to the heat load and space constraints in cryogenic systems. Recent breakthroughs have addressed this challenge through innovative readout schemes. Row-column multiplexing has enabled the first demonstration of a kilopixel array (1024 pixels), while requiring only $2N$ readout lines for an $N \times N$ array [34]. Even more remarkably, novel architectures combining time-of-flight measurements with thermal coupling have demonstrated the potential for megapixel arrays using as few as four RF lines, independent of array size [35, 47]. These advancements in scaling SNSPD technology to large detector arrays, together with ongoing improvements in detector performance, are expanding the horizons of what is possible with single-photon detection.

1.3 Fundamentals and performance metrics of SNSPDs

In this section, we summarize the current understanding of the operating principle of SNSPDs, based on experimental evidence and theoretical frameworks, closely following the review of Engel *et al.* [48]. Moreover, we introduce the detector's key performance metrics, including optimization strategies and trade-offs, followed by highlighting current challenges in this active field of research.

1.3.1 Detection mechanism

The conversion of a single photon's energy into a detectable voltage pulse in an SNSPD involves multiple physical processes occurring on different timescales. Understanding these processes and their interplay has been the subject of extensive theoretical and experimental investigation. Several models have been proposed, each offering different insights into the detection mechanism. The simplest and most intuitive of these is the normal-core hotspot model.

Normal-core hotspot model

In the normal-core hotspot model [37, 48], the detection process begins when a photon is absorbed in the superconducting nanowire, which is biased with a current close to its critical current. The absorbed photon creates a highly excited electron with energy $E_{\mathrm{exc}} \gg \Delta$, where Δ is the superconducting energy gap. This excited electron undergoes a cascading thermalization process, creating multiple quasiparticle excitations and phonons. The created quasiparticles form a localized region of suppressed superconductivity—the so-called "hotspot"—in the nanowire. If this normal-conducting region becomes large enough (with a diameter exceeding the coherence length), the bias current is forced to flow through the remaining superconducting cross-section of the wire. This results in an increased current density in these regions. When the current density exceeds the critical current density of the superconductor, it triggers the transition of the entire cross-section into the normal state. Due to the kinetic inductance of the nanowire, the bias current is still forced through the now normal-conducting region. The resulting joule heating induces a growth of the resistive barrier. At the same time, a detectable voltage pulse is created due to the current flowing through the normal conducting domain of the SNSPD. Eventually, the high resistance leads to a significant reduction of the bias current, enabling restoration of superconductivity. Finally, the bias current returns to its original state and the detector is sensitive to the next photon.

While this model provides an intuitive picture of the detection process, it predicts an energy-current relation of the form

$$I_{\mathrm{th}} = I_{\mathrm{c}}(1 - \gamma' \sqrt{E}) \; , \tag{1.1}$$

where I_{th} is the threshold current required for single-photon detection, I_{c} is the critical current, E is the photon energy, and γ' is a device- and material-dependent constant. This square-root behavior is inconsistent with the experimentally observed linear relationship between photon energy and threshold current, indicating the need for more sophisticated models [48].

Advanced detection models

While the normal-core hotspot model provides an intuitive framework, several more sophisticated models have been developed to better explain experimental observations. The main ingredients for these models are (1) the consideration of quasiparticle diffusion dynamics, and (2) taking magnetic vortices into account.

Diffusion-based models consider the detailed dynamics of quasiparticle diffusion and their effect on the local superconducting properties. For example, the diffusion-based hotspot model [48, 49] treats the suppression of superconductivity as a continuous process rather than assuming an abrupt normal-conducting core. This model successfully explains several experimental observations, including the linear energy-current relation and the dependence of the detection threshold on nanowire width and thickness. However, the spatial dependence of the threshold current along the width of the nanowire cannot be explained by this model. Moreover, similar to the normal-core hotspot model, this model predicts a deterministic, threshold-like response to photons: all photons above a certain energy are detected, all others are not. Experiments, on the contrary, show that there is a slow decrease of the count rate when decreasing the bias current through the detector.

Vortex-based models introduce magnetic vortices as key component in the detection process. These models propose that the absorbed photon reduces the barrier for vortex entry or vortex-antivortex pair generation, which then trigger the formation of a normal-conducting domain. The importance of magnetic vortices is supported by systematic experimental studies of the magnetic field dependence of both dark count rate and photon count rate, and is particularly evident in the exponential increase of the dark count rate with increasing bias current [48, 50–52]. The most recent approaches combine aspects of both quasiparticle diffusion and vortices to numerically model the detection process [48, 53–56].

Despite these advances, no single model currently explains all experimental observations. However, the continued development of detection models provides valuable insights for optimizing detector performance for example via material choice and device engineering. Now that we have introduced the microscopic detection mechanism, we turn to how the resulting voltage pulse is further processed through the readout circuit.

1.3.2 Electronic readout

In this section we present the typical electrical readout circuit used for efficient extraction of the photon detection signal from an SNSPD [37, 57–59]. The detector is DC-biased through a bias tee, which separates the high-frequency detection signal from the DC bias current. The bias current is supplied through the DC port of the bias tee by applying a constant voltage across a large bias resistor (e. g., $50\,\mathrm{k}\Omega$) to provide a quasi constant current to the SNSPD. Additionally, a shunt resistor (e. g., $20\,\Omega$) can be placed in parallel with the detector to prevent latching in the normal state after a detection event. When a normal-conducting domain forms across the nanowire and the resistance of the nanowire gets much larger than the typically $50\,\Omega$ load resistance at the RF arm of the bias tee, the bias current is diverted to the $50\,\Omega$ readout line, creating a fast voltage pulse. This pulse is then amplified using broadband RF amplifiers, operating at room temperature or, for best signal-to-noise ratios, at cryogenic temperatures. The amplified signal can be processed for example by a threshold discriminator and counter for photon counting applications, a time tagger for time-correlated single-photon counting, or by a high-bandwidth oscilloscope for detailed analysis of the detection pulses.

1.3.3 Key performance metrics

The performance of SNSPDs is characterized by several key metrics that determine their suitability for different applications. Understanding these metrics and their interdependencies is crucial for optimizing detectors for specific use cases.

Detection efficiency

The system detection efficiency (SDE) describes the probability that a photon is detected by the SNSPD system, including all losses inside the system. It can be separated into

$$\mathrm{SDE} = \eta_{\mathrm{OCE}} \cdot \eta_{\mathrm{abs}} \cdot \eta_{\mathrm{IDE}}\ , \tag{1.2}$$

where η_{OCE} is the optical coupling efficiency of incident photons to the active detector area, η_{abs} is the absorption efficiency of photons coupled to the detector, and η_{IDE} is the intrinsic detection efficiency that describes the probability that an absorbed photon results in a voltage pulse. State-of-the-art SNSPDs achieve system detection efficiencies exceeding 90 % at wavelengths from visible to near-infrared [40]. The optical coupling efficiency can be enhanced through optimized fiber coupling or optical waveguide integration, while the absorption probability can be increased via optical cavity designs and optimized film thickness. The internal detection efficiency depends on the bias current and the device geometry.

Dark count rate

Dark counts are detection events that occur in the absence of incident photons. The dark count rate (DCR) can be as low as sub-Hz in optimized devices [27], and they originate for example from thermal fluctuations leading to vortex crossing, background radiation, or electronic noise. The DCR decreases exponentially with decreasing bias current. This results in a trade-off between low dark count rate and high detection efficiency.

Timing jitter

Timing jitter of SNSPDs is defined as the full width at half maximum (FWHM) of the temporal distribution of output signals with respect to the photon arrival times. It characterizes the temporal uncertainty in the detection of a photon, crucial for applications requiring precise timing information. Optimized SNSPDs can achieve timing jitter below 3 ps [28]. Improving the electronic noise floor of the readout circuit, impedance matching the nanowire to 50 Ω, or optimizing the nanowire geometry could further reduce the timing jitter [28, 30].

Maximum count rate

The maximum count rate is limited by the detector's reset time, which can be calculated by the kinetic inductance of the nanowire as

$$\tau_{\text{reset}} = \frac{L_{\text{k}}}{R_{\text{L}}} \tag{1.3}$$

where L_{k} is the kinetic inductance and R_{L} is the load resistance [60]. Since the kinetic inductance scales linearly with the nanowire length, shorter nanowires enable faster reset times [61]. Typical reset times are on the order of several nanoseconds, enabling count rates in the hundreds of MHz range [62]. However, using short nanowires integrated into a photonic crystal cavity allows efficient detection of single-photons at telecom wavelengths with sub-nanosecond reset times, showing potential for GHz count rates [63].

Spectral range

SNSPDs can detect photons over a spectral range extending from x-rays, over visible light, to far-infrared wavelengths [32, 64–66]. The detection efficiency generally decreases with increasing wavelength since long wavelength photons are challenging to detect due to their lower energy and associated smaller quantity of generated quasiparticles upon photon absorption. The long-wavelength cut-off is determined by quantities such as the superconducting energy gap, the operating temperature, the nanowire width and thickness, as well as the bias current relative to the critical current [49]. Taylor *et al.* [64] recently achieved a new record by demonstrating saturating internal detection efficiency for far-infrared photons of 29 µm wavelength.

Operating temperature

Most SNSPDs operate at temperatures well below their critical temperature, typically at $T_c/2$ or lower [40]. Higher operating temperatures are desirable for practical applications with integration in less demanding cooling systems, but generally result in a reduced detection efficiency and increased dark count rate [40, 67]. The current temperature record is held by Charaev *et al.* [43] who developed large-scale MgB_2 SNSPDs that exhibit single-photon sensitivity up to a temperature of 20 K.

The performance metrics described above are interdependent, often requiring trade-offs in detector optimization. For example, increasing the bias current improves detection efficiency but simultaneously raises the dark count rate. Similarly, for an SNSPD covering a fixed active area, reducing the nanowire width extends the spectral range, but reduces the system detection efficiency or increases the timing jitter. Understanding these relationships is crucial for designing detectors tailored to specific applications.

In the following chapters, we demonstrate how He ion irradiation techniques can overcome several of these long-standing trade-offs. Chapters 2 to 4 introduce novel approaches that expand the possibilities for detector optimization beyond conventional fabrication methods. With the key performance characteristics established, we now compare SNSPDs with alternative single-photon detection technologies to highlight their unique advantages for specific applications.

1.3.4 Comparison with other technologies

Single-photon detection can be achieved through various technologies, each with distinct advantages and limitations. The main competing technologies to SNSPDs are single-photon avalanche diodes (SPADs) and transition edge sensors (TESs).

SPADs are semiconductor-based detectors that operate through avalanche multiplication of photogenerated carriers. They offer several advantages such as operation at room temperature, easy integration with conventional electronics, and relatively low costs. However, they suffer from limitations including high dark count rates, significant afterpulsing, and rapidly decreasing detection efficiency beyond 1.7 µm wavelength [68].

TESs operate by measuring the temperature rise of a superconducting film upon photon absorption. Their key features include near-unity detection efficiency, photon number resolution, and a wide spectral range. However, the main drawbacks are their long reset time, large timing jitter, and requirement for sub-Kelvin operating temperatures [69–71].

In contrast, SNSPDs achieve several state-of-the-art performance metrics simultaneously. With near-unity detection efficiency from X-rays through visible light to far-infrared photons [32, 33, 64–66], sub-Hz dark count rate [27], picosecond timing jitter [28], and nanosecond reset time [29], they excel in demanding applications such as photonic quantum computing [9–15], lidar [28, 72–74], particle and dark matter detection [19–23], and infrared fluorescence microscopy for in vivo deep brain imaging [1–3]. Table 1.1 summarizes the key performance metrics of these competing single-photon detector technologies. The distinct advantages of SNSPDs have established them as the detector of choice for many quantum technology applications. However, several challenges remain to be addressed for wider adoption and continued performance improvements.

1.4 Current challenges in SNSPD development

Despite their exceptional performance, SNSPDs face several key challenges for wider adoption. The requirement for cryogenic operating temperatures, typically below the boiling point of He at 4.2 K, necessitates sophisticated cooling systems. While recent demonstrations with MgB_2 have pushed operation temperatures up to 20 K [43], achieving high-performance operation at elevated temperatures remains an ongoing challenge. On the system level, scalable readout solutions for large detector arrays face the challenge of keeping the thermal load from the readout circuitry as low as possible, while maintaining the exceptional timing performance of single-channel SNSPDs. Recent advances have demonstrated kilopixel and even 400 000-pixel arrays, with a

Table 1.1: Comparison of key performance metrics across three leading single-photon detection technologies: SNSPDs, single-photon avalanche diodes (SPADs), and transition edge sensors (TESs). Each entry presents typical/record value pairs with citations for record performances. Maximum wavelength is shown rather than spectral range because long-wavelength detection is typically the critical performance limitation, while shorter wavelengths are generally more readily detected by all three technologies. Some record values have been compiled from comprehensive reviews [75–77].

Parameter	SNSPD	SPAD	TES
Detection efficiency	90 % / 99.5 % [78]	50 % / 70 % [79]	95 % / 98 % [71]
Dark count rate	10 Hz / 0.1 mHz [27]	1 kHz / 1 Hz [80]	1 Hz / 0.36 mHz [81]
Timing jitter	20 ps / 2.6 ps [28]	100 ps / 30 ps [82]	100 ns / 2.3 ns [83]
Reset time	10 ns / 130 ps [29]	30 ns / 1.5 ns [84]	1 µs / 75 ns [85]
Operating temp.	$<$ 4 K / 20 K [43]	300 K / 350 K [86]	$<$ 0.1 K / 90 K [87]
Photon num. res.	Yes (emerging) [88]	No [89]	Yes [90]
Max. wavelength	2 µm / 29 µm [64]	1 µm / 1.7 µm [91]	500 µm / 2 mm [92]

clear path towards megapixel arrays [34, 35, 47]. However, both approaches suffer from relatively high timing jitter compared to single-channel SNSPDs. At the device level, a longstanding fundamental challenge in SNSPD design is the effect of current crowding in the bends of meander-shaped detectors. This local increase in current density near the turns limits the maximum applicable bias current to significantly below the critical current of straight nanowires [93, 94]. Since the detection efficiency and the dark count rate strongly depend on the ratio of bias current to critical current, current crowding effectively limits these key performance metrics. Various geometric solutions have been proposed to mitigate this effect [93–99], but they often require compromises in fill factor or device layout that limit the overall system detection efficiency or timing properties. Overcoming current crowding without such trade-offs remains an important challenge for which we develop a solution in Chapter 3.

Beyond these fundamental challenges, several technical limitations directly impact detector optimization and practical deployment. A key challenge is achieving uniform performance across detector arrays. While individual SNSPDs can achieve near-perfect detection efficiency, maintaining consistent performance across multiple pixels remains difficult due to variations in critical current and other superconducting properties [100–103]. This challenge is directly addressed in Chapter 2, where we demonstrate post-fabrication enhancement of individual SNSPDs by site-selective He ion irradiation.

Another significant challenge lies in optimizing the detection efficiency while maintaining other performance metrics. For example, using thicker superconducting films would increase photon absorption, but typically reduces the internal detection efficiency. Similarly, reducing the nanowire width can extend the spectral range but may compromise timing performance and fabrication yield. These trade-offs highlight the need for new approaches to enhance specific detector metrics without sacrificing other critical parameters.

Recent advances in materials science and nanofabrication techniques offer promising pathways to address these challenges. In particular, a recent study has shown that uniform He ion irradiation of superconducting films can modify their properties and enhance detector performance [104]. However, achieving precise control over local superconducting properties remains an open challenge.

New approaches to address these challenges require sophisticated nanofabrication and characterization tools. In the following section, we discuss the key fabrication methods for SNSPD development, with particular focus on the He ion microscope, which will emerge as a pivotal tool for addressing several of these challenges in the following chapters.

1.5 Nanofabrication of SNSPDs

The exceptional performance of SNSPDs relies heavily on precise nanofabrication techniques and sophisticated tools for material modification. This section provides a general and concise introduction to the fabrication methods essential for SNSPD development [105, 106], with particular focus on He ion microscopy as an emerging technology for nanoscale material modification. Experiment-specific fabrication details are discussed in their corresponding chapters.

1.5.1 Standard fabrication methods

The fabrication of high-performance SNSPDs typically involves three key steps: thin film deposition, nanowire patterning, and electrical contact formation. Thin film deposition of superconducting materials such as NbTiN is commonly achieved via DC reactive magnetron sputtering. This technique enables precise control over film stoichiometry and thickness, crucial parameters that influence the detector's critical temperature and detection efficiency. The quality of the deposited film, particularly its uniformity and crystal structure, directly impacts device performance and fabrication yield. After film fabrication, the nanowire pattern is defined via electron beam lithography due to its high spatial resolution and typically consists of 50 nm to 250 nm wide wires. Subsequently, the pattern is transferred to the superconducting film via reactive ion etching. Finally, contact pads for electrical connection are fabricated via photolithography and consecutive Ti/Au evaporation and liftoff.

1.5.2 The He ion microscope as a versatile tool

Among the tools available for nanoscale modification and characterization, the He ion microscope (HIM) has emerged as a particularly powerful instrument. Unlike traditional focused ion beam systems that typically use gallium ions, the HIM employs a focused beam of He ions, offering several unique advantages for nanoscale imaging and modification. The HIM operates by field ionization of He gas at an atomically sharp tungsten tip, creating a bright ion source [107, 108]. Combined with sophisticated ion optics, this enables both high-resolution imaging and precise material modification at the nanoscale. When used for imaging, the HIM achieves superior surface sensitivity and depth of field compared to the scanning electron microscope (SEM) [109, 110]. Beyond imaging capabilities, the HIM enables controlled modification of material properties via beam–sample interactions [110]. When He ions penetrate a material, they create defects through nuclear collisions and electronic excitations. The depth distribution and density of these modifications can be precisely controlled through the ion energy and fluence. Moreover, the achievable beam size of less than 1 nm allows for local material modification with nanometer precision [107].

Recently, modification of SNSPD properties via He ion irradiation was achieved using a He ion implanter, which enabled uniform, wafer-scale bombardment [104]. While this approach demonstrated the potential of He ion irradiation for enhancing detector performance, the capabilities for nanoscale, targeted modification remained unexplored. The HIM, with its precise beam control and nanometer resolution, offers new possibilities for local material engineering that are central to the techniques developed in Chapters 2 to 4, where we enhance detector performance by thermal conductance engineering (Chapter 4), and address fundamental challenges in SNSPD development such as current crowding (Chapter 3) and performance uniformity across detector arrays (Chapter 2).

1.6 Research objectives and thesis structure

The overarching goal of this thesis is to investigate how precisely controlled He ion irradiation can enhance the performance of SNSPDs while overcoming existing limitations. It addresses several key challenges in SNSPD development through a systematic progression of increasingly sophisticated irradiation techniques and detailed analysis of the underlying physical mechanisms. Specifically, this thesis aims to answer the following research questions:

Can site-selective He ion irradiation tune individual SNSPD performance? While wafer-scale irradiation has previously been demonstrated to improve detector performance, a detailed study of how He ion irradiation changes detector properties and a method to selectively modify individual detectors on the same chip have been lacking. However, these are crucial for achieving uniform performance across SNSPD arrays and optimizing detectors for specific applications post-fabrication.

Can local He ion irradiation eliminate the effects of current crowding? Current crowding at the bends of meander-shaped SNSPDs represents a fundamental limitation on detector performance, particularly at low temperatures where these devices operate optimally. Existing solutions to current crowding typically require compromises in fill factor or device layout that limit overall system detection efficiency or timing properties.

How does He ion irradiation enhance SNSPD performance? Understanding the physical mechanisms responsible for improved detector performance is essential for developing optimized irradiation strategies and predicting their effects across different material systems and device configurations.

These research questions are addressed through three interconnected experimental investigations, each of which has been published or submitted for publication as an independent research article. The experimental chapters in this thesis are based on these publications, with modifications to create a cohesive narrative and to highlight the connections between the studies. Together, these chapters provide a broader understanding of He ion irradiation for SNSPD enhancement than would be possible through the individual publications alone.

Chapter 2 establishes the foundation for this thesis by demonstrating site-selective enhancement of SNSPDs via He ion irradiation. By precisely controlling irradiation parameters, we transform thick-film (12 nm) detectors from a detection efficiency $< 0.05\,\%$ to $55.3\,\%$—all modifications performed on individual devices on the same chip. Through investigation of the scaling of device metrics with the He ion fluence, we develop a physical model that describes how irradiation modifies the superconducting properties, providing the framework for the more advanced techniques explored in subsequent chapters.

Chapter 3 builds upon these findings to address the long-standing challenge of current crowding in SNSPDs. By locally irradiating only the straight segments of meander-shaped detectors while leaving the bends unirradiated, we demonstrate a novel approach that eliminates current crowding as the limiting factor while simultaneously enhancing the detectors' sensitivity. This solution enables larger relative plateaus of saturating detection efficiency (37 % versus 10 %) and lower dark count rates compared to fully irradiated devices, while maintaining high critical currents.

Chapter 4 investigates the fundamental physical mechanisms behind the observed performance enhancements. Through comprehensive material characterization and transport measurements, we reveal that He ion irradiation not only modifies the superconducting film but also transforms the underlying substrate through amorphization and bubble formation. These modifications substantially reduce the thermal conductance between film and substrate from $210\,\mathrm{W\,m^{-2}\,K^{-4}}$ to $70\,\mathrm{W\,m^{-2}\,K^{-4}}$ after irradiation with $2000\,\mathrm{ions\,nm^{-2}}$, significantly enhancing detector sensitivity. By irradiating only regions adjacent to the nanowire, we exploit lateral ion straggle to modify thermal properties beneath the wire itself, achieving saturating detection efficiency with large plateau widths while maintaining high critical currents. These findings reveal that a reduction of the thermal conductance is a key mechanism behind the He ion irradiation-induced performance enhancement, and establish thermal conductance engineering as a powerful approach for SNSPD optimization.

The thesis concludes with Chapter 5, which synthesizes our key findings and discusses their implications for future SNSPD development. By combining our understanding of site-selective and irradiation-induced modification of SNSPDs and their underlying substrates, current crowding mitigation, and thermal conductance engineering, we identify promising future research directions. These include novel irradiation patterns, the combination of complementary irradiation techniques, acceleration voltage optimization, applications to different material systems and substrates, and potential extensions to other superconducting devices.

Together, the investigations presented in this thesis, as summarized in Figure 1.1, both advance the fundamental understanding of how He ion irradiation modifies SNSPDs and their substrates, and establish practical techniques for engineering next-generation single-photon detectors with unprecedented performance.

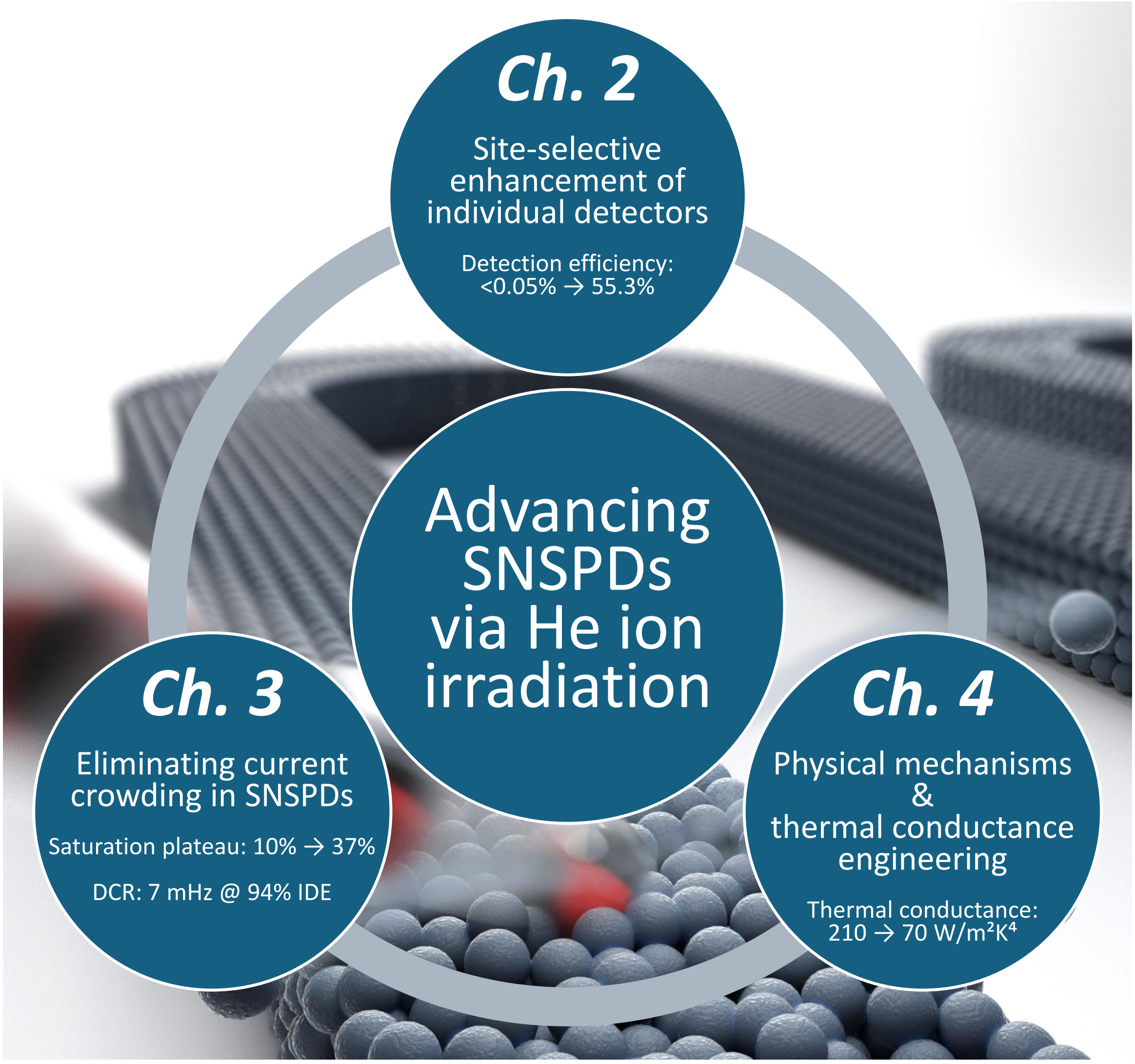

Figure 1.1: Overview of the thesis structure and key results. This thesis investigates the enhancement of SNSPDs by He ion irradiation through three interconnected chapters: site-selective enhancement of individual detectors (Chapter 2), elimination of current crowding in meander-shaped designs (Chapter 3), and understanding the underlying physical mechanisms with further applications for thermal conductance engineering (Chapter 4). Background image adapted from the front cover of Advanced Quantum Technologies, Volume 6, Issue 12 (2023), used with permission from John Wiley & Sons. The original research was published in [111].

2 Site-selective enhancement of SNSPDs via local He ion irradiation

This chapter presents the first step in our investigation of how He ion irradiation can enhance SNSPD performance. While SNSPDs exhibit exceptional performance metrics, it remains challenging to achieve uniform performance across detector arrays and to optimize thick-film detectors. We demonstrate a novel post-processing technique using site-selective He ion irradiation to tune the properties of individual NbTiN devices on the same chip. This approach allows modification of key parameters including detection efficiency, switching current, and critical temperature with unprecedented spatial control. For 12 nm thick highly absorptive SNSPDs, which are barely sensitive to single photons prior to irradiation, we observe an increase of the system detection efficiency from $< 0.05\,\%$ to $55.3\,\%$ following irradiation with $1800\,\mathrm{ions\,nm^{-2}}$. Irradiated thick detectors also show higher switching current compared to thinner devices with similar efficiency. Moreover, we present a physical model accounting for defect generation and sputtering during He ion irradiation, which shows good qualitative agreement with the observed increase of sheet resistance and decrease of critical temperature towards higher fluences. These findings establish site-selective He ion irradiation as a powerful technique for post-fabrication optimization of SNSPDs, setting the foundation for targeted applications and mechanistic investigations in subsequent chapters.

The research presented in this chapter has been published as Strohauer, S. et al. *Site-Selective Enhancement of Superconducting Nanowire Single-Photon Detectors via Local Helium Ion Irradiation.* Adv. Quantum Technol. ***6****, 2300139 (2023), under a CC BY 4.0 license. The chapter largely follows this publication, with modifications to integrate it into the broader context of this thesis.*

Contents

2.1 Introduction

As discussed in Section 1.1, SNSPDs play a significant role in diverse fields ranging from quantum technologies to general faint light detection. More recently, SNSPDs have also found application in research areas such as astronomy [5], dark matter detection [20], and particle detection [21, 23]. However, these applications typically require large detector arrays or even an SNSPD camera, which to date turns out to be challenging due to the necessary readout and homogeneity within arrays of hundreds to millions of detectors. Recently, row-column multiplexing of a 1024-pixel array [34], and a promising readout architecture based on thermal coupling and time-of-flight measurements [35] were demonstrated. For such pixel arrays, typically amorphous materials such as MoSi and WSi are used, although SNSPDs based on polycrystalline materials like NbN and NbTiN exhibit higher critical temperatures, larger critical currents, and lower timing jitter. Compared to polycrystalline materials and their spatial inhomogeneities of the superconducting energy gap [112–115], amorphous films achieve a better homogeneity and an associated higher yield of similarly performing detectors [40, 105, 116–118]. To enable the use of NbN for large pixel arrays, atomic layer deposition and molecular-beam epitaxy of highly homogeneous films have been investigated recently as alternatives to the common deposition of polycrystalline NbN and NbTiN films grown using reactive magnetron sputtering [100–103]. In addition to methods for obtaining better homogeneity during film deposition, a method to tune detector metrics of individual devices after fabrication would also be highly advantageous. Inspired by the recent work of Zhang *et al.* [104], which sparked interest in irradiating SNSPDs with He ions [119–121], we use a He ion microscope as a post-processing tool to tune detector metrics of individual NbTiN devices fabricated on the same chip. At the same time, we investigate how SNSPD properties such as detection efficiency and switching current depend on the He ion fluence. In addition to detector metrics, we explore the scaling of NbTiN thin film parameters such as sheet resistance and critical temperature with increasing irradiation.

The irradiation technique established in this chapter, with its ability to precisely tune the properties of SNSPDs, forms the foundation for the advanced irradiation strategies and mechanistic investigations in Chapters 3 and 4.

2.2 Sample fabrication and measurement techniques

To study the influence of He ion irradiation on the native transport properties of NbTiN thin films and the performance of SNSPDs, we deposited NbTiN films with thicknesses of 8 nm, 10 nm, and 12 nm using DC reactive magnetron sputtering onto Si substrates with a 130 nm thick thermally grown SiO_2 layer. The NbTiN thickness was controlled by measuring the sputtering rate and adjusting the sputtering time correspondingly. Subsequently, we patterned the NbTiN films into cloverleaf structures and SNSPDs using electron beam lithography and reactive ion etching, followed by optical lithography and gold evaporation for contact pad fabrication [105, 106, 122]. The detector design consists of a 100 nm wide wire in a meander form with a fill factor of 50 %, and a total active area of 10 µm × 10 µm. The cloverleaf structures were fabricated in order to perform magneto-transport measurements in van-der-Pauw geometry [123, 124] with an active area of 10 µm × 10 µm and to correlate the results of macroscopic transport with the He ion fluence dependent performance metrics of the corresponding SNSPDs. To ensure the best comparability, cloverleafs (CLs) and SNSPDs were fabricated on the same chip. For this study, they were subsequently irradiated with a He ion microscope (Zeiss Orion Nanofab) with He ion fluences ranging from 0 ions nm^{-2} to 2600 ions nm^{-2}. We chose an acceleration voltage of 30 kV, an aperture of 10 µm and 20 µm, and beam currents between 0.3 pA and 114 pA, with the largest aperture and beam current used for the largest He ion fluences to obtain irradiation times of less than 30 minutes per device also for the largest fluences. Despite the sub-nanometer resolution of the He ion microscope, which makes it also attractive as a patterning tool for SNSPD fabrication [125–127], focusing the He ion beam to the smallest beam sizes was not necessary in this chapter since we homogeneously irradiated an area slightly larger than the active area of the SNSPDs and CLs as shown in Figure 2.1 and the inset of Figure 2.8. The irradiation induced film surface roughness we measured with an atomic force microscope (Bruker Dimension Icon) in peak force tapping mode.

The magneto-transport measurements were performed by cooling the samples to 4.2 K before allowing them to slowly heat up to 20 K in external magnetic fields between −0.1 T and 1 T, applied perpendicular to the sample plane. From these measurements, we extract the sheet resistance of the superconducting thin film at 20 K and room temperature, the critical temperature of the superconducting thin film, and the Bogoliubov quasiparticle diffusivity. Also, by measuring the CLs in Hall geometry

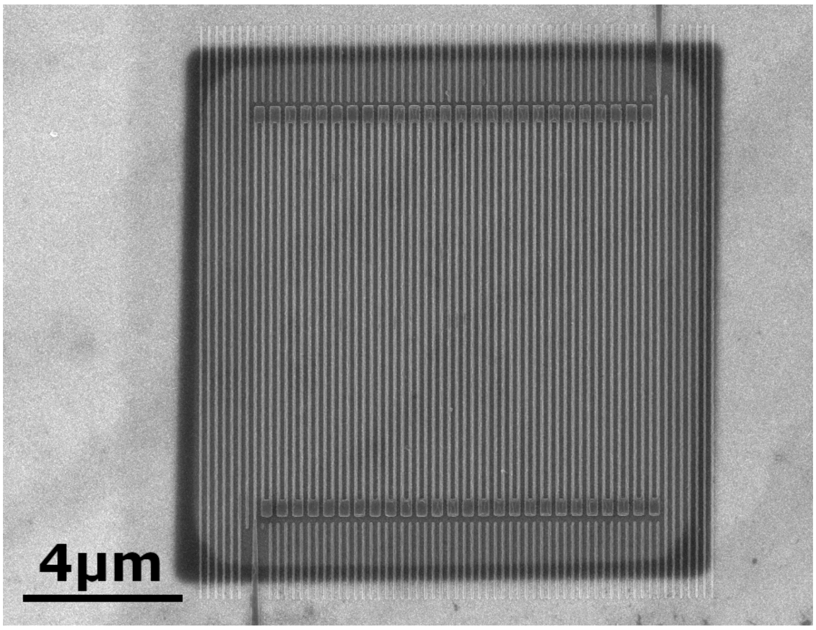

Figure 2.1: Scanning electron microscope image of an SNSPD after He ion irradiation. The irradiated area is visible as the dark shaded square region and was chosen to be slightly larger than the SNSPD to ensure homogeneous irradiation of the detector. Adapted from [111], used under CC BY 4.0.

and performing magnetic field sweeps, followed by a linear fit of the Hall voltage, we determine the Hall coefficient and electron density of the NbTiN films [128].

Switching current I_{sw} and system detection efficiency (SDE) of the SNSPDs were measured using a cryogenic probe station (Janis) at 4.5 K. To determine the switching current, we ramp up the voltage U_{app} applied across the SNSPD and a 50 kΩ resistor connected in series, while measuring the current I_{meas}. The switching current is then defined as the current at which the criterion $U_{\mathrm{app}}/I_{\mathrm{meas}} > 50.5\,\mathrm{k\Omega}$ is fulfilled for the first time. To calculate the SDE, we determined the dark count rate (DCR) before we measured the count rate (CR) by homogeneous illumination of the SNSPD with an attenuated and collimated 780 nm continuous wave diode laser with a spot size of (1.1 ± 0.1) mm (full width at half maximum of the intensity profile) and polarization parallel to the nanowire. The SDE is then defined as $\mathrm{SDE} = \frac{\mathrm{CR}-\mathrm{DCR}}{\mathrm{PR}}$ with the photon rate PR incident on the cryogenic probe station.

The bias current for all measurements in this thesis was supplied by applying a biasing voltage U_{bias} across the SNSPD and a 50 kΩ resistor using a Keithley 2450 source meter, which provides precise voltage control and current monitoring capabilities. For future experiments involving multiple detectors, we have also developed a custom four-channel biasing module described in Appendix D. This system not only offers the required voltage and current control but also implements automated switching current detection and bias percentage setting—features not available in commercial alternatives—while reducing costs significantly per channel.

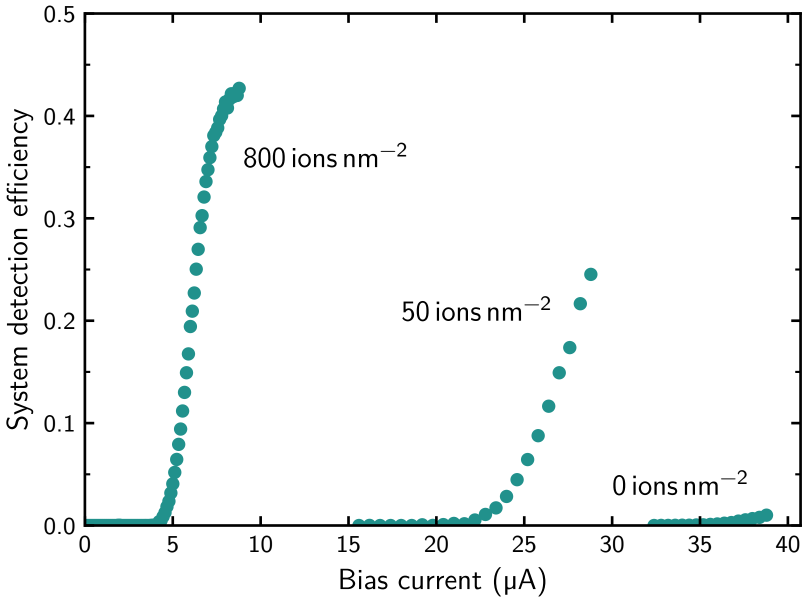

Figure 2.2: System detection efficiency vs. bias current of the same 10 nm thick detector for three different He ion fluences. The relative uncertainties of He ion fluence, SDE, and bias current are 5 %, 2 % and less than 1 %, respectively (error bars not shown for clarity). The measurements were performed at a temperature of 4.5 K and using photons with a wavelength of 780 nm. With increasing fluence the efficiency rises up to 43 % and shows the beginning of saturating internal detection efficiency, while the switching current decreases. The largest change in SDE and I_{sw} is induced by the first He ions that hit the detector. Adapted from [111], used under CC BY 4.0.

2.3 He ion irradiation of SNSPDs and thin films

In this section, we present the dependence of NbTiN thin film properties and detector metrics on He ion irradiation for film thicknesses of 8 nm, 10 nm, and 12 nm. Provided that the SNSPDs are sensitive to single photons, using larger thicknesses for SNSPDs generally results in stronger optical absorption [129, 130] and therefore enhances their overall system detection efficiency (SDE). Moreover, we aim for a better understanding of how He ion irradiation modifies the transport properties of the NbTiN film and focus on establishing structure-property relationships that link detector thickness, He ion fluence, and detector performance.

2.3.1 Performance of He ion irradiated SNSPDs

Figure 2.2 shows the increase in SDE and the simultaneous decrease of switching current of a representative 10 nm thick device measured before irradiation and after fluences of 50 ions nm^{-2} and 800 ions nm^{-2}. Irradiating the detector with 50 ions nm^{-2} already results in an increase in SDE from $< 2\,\%$ to 25 %. At a fluence of 800 ions nm^{-2} the detector shows the beginning of saturating SDE at 43 %, close to the maximum

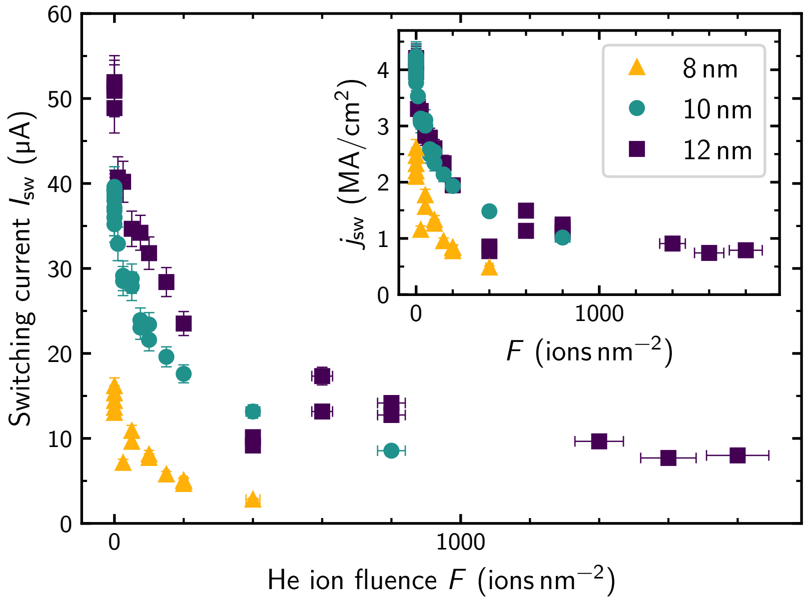

Figure 2.3: Switching current vs. He ion fluence for 8 nm, 10 nm, and 12 nm detector thickness, including statistical errors. I_{sw} decreases with the He ion fluence, showing the largest decrease for low fluences. A strong dependence of I_{sw} on the film thickness is apparent throughout the whole fluence range studied. The inset shows the switching current density j_{sw} as calculated from I_{sw} and the wire width and thickness, accounting for an effective thickness reduction due to surface sputtering during He ion irradiation as well as a 1.3 nm thick native NbTiN oxide. The large data point clusters at 0 ions nm^{-2} originate from measurements of a large subset of devices before irradiation. Adapted from [111], used under CC BY 4.0.

absorption of 53.1 % in the detector as determined by finite-difference time-domain (FDTD) simulations (Appendix A). Simultaneously, a decrease in switching current I_{sw}, which is defined as the maximum current the detector can sustain before switching to the normal conducting state, is apparent and ranges from 39.2 µA to 28.8 µA and 8.6 µA after irradiation.

To study the scaling of the switching current with He ion fluence, we irradiated multiple detectors that have thicknesses of 8 nm, 10 nm, and 12 nm using different He ion fluence values. Figure 2.3 shows the resulting data, revealing a clear trend of decreasing I_{sw} with He ion fluence. As expected, I_{sw} is higher for thicker devices of the same fluence due to the larger cross-sectional area of thicker nanowires. We explain the scattering of measured switching currents of nominally identical detectors by constrictions that limit I_{sw} to a lower value than non-constricted devices have [118]. Such scatter is particularly visible by the large variation of currents of the unirradiated devices and the small values of the two 12 nm detectors irradiated with 400 ions nm^{-2}. The inset of Figure 2.3 shows the switching current density j_{sw} as calculated from I_{sw} and the cross-sectional area of the wire, given by the width and the nominal wire thickness presented in Table A.1. Furthermore, we accounted for

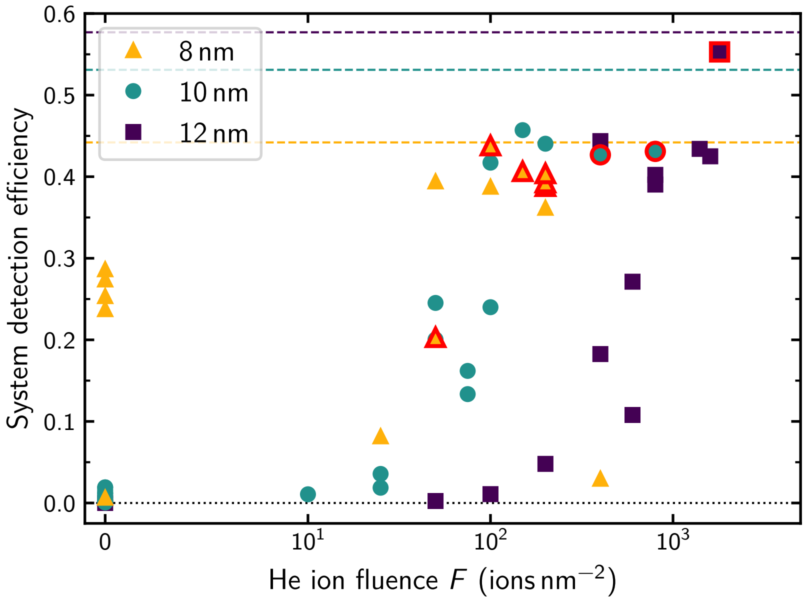

Figure 2.4: System detection efficiency vs. He ion fluence for the three detector thicknesses studied in this chapter. Dashed lines indicate the absorption in the SNSPD simulated with FDTD; data points with saturating SDE are highlighted with a red frame. The relative uncertainties of SDE and He ion fluence are 2 % and 5 %, respectively (error bars not shown for clarity). Each of the data points stems from a different detector that was irradiated once with the given dose except for two 10 nm and two 12 nm detectors that were irradiated twice; for some SNSPDs we measured the SDE in addition also before irradiation. The measurements were performed at a wavelength of 780 nm. Despite the large scattering of data points that can be explained by the strong variation of the initial SDE between individual devices, one clearly sees that the SDE increases with He ion fluence and that the total maximum SDE is reached by the largest detector thickness. Adapted from [111], used under CC BY 4.0.

an effective reduction of the nominal thickness due to surface sputtering during He ion irradiation as derived in Section 2.3.2 and for a native NbTiN oxide of 1.3 nm thickness [131]. The switching current density of our unirradiated NbTiN detectors is comparable to the data Korneeva *et al.* [132] present for 5.8 nm thick NbN devices. Moreover, we observe j_{sw} of the 8 nm film being smaller than for the 10 nm and 12 nm films. We note that for thin and narrow wires, the depairing current density [132, 133] can limit the measurable switching current density and reveals a dependence on the film thickness [134, 135]. Thus, an increased depairing current density for the thicker devices also likely contributes to their higher I_{sw} and j_{sw}. Furthermore, the limiting critical current of our devices presumably occurs at the hairpin turns of the nanowires due to current crowding, especially at temperatures well below the critical temperature [93, 136, 137].

Similar to I_{sw}, we investigated the scaling of SDE with the He ion fluence. As shown in Figure 2.4, we observe an increase of SDE with the He ion fluence for all detector thicknesses, despite the large scatter between data obtained from nominally identical SNSPDs. Most notably, the SDE for the 12 nm thick detectors increases from less than 0.05 % for the unirradiated case to 55.3 % and just saturating detection efficiency for a fluence of 1800 ions nm^{-2}. As expected, the SDE increases with detector thickness due to the higher absorption. The dashed horizontal lines in Figure 2.4 show the upper limit for the SDE, defined by the absorption of SNSPDs of the respective thicknesses that we obtained from FDTD simulations discussed in Appendix A. We note that one can further enhance the absorption and thus the SDE over a broad wavelength range by adding a metal mirror with an optical cavity underneath the SNSPD [46]. Recently, a similar approach for He ion irradiated detectors involving a narrowband cavity, realized with a distributed Bragg reflector, has shown to push the absorption to over 90 % [119]. The fact that the measured SDE of the highest irradiated 8 nm detector shown in Figure 2.4 is less than 3 % can be explained as follows: Due to the irradiation-induced reduction of the switching current (to 2.8 µA for this detector), which is also the maximum applicable bias current, the maximum voltage pulse amplitude decreases as well. However, the trigger level of the counter used to measure the efficiency can only be reduced correspondingly as long as it is well above the electrical noise floor. This implies that once the pulse amplitude becomes comparable to the electrical noise floor, a substantial fraction of detection pulses will not be registered by the counter anymore. Depending on the readout electronics used and on their noise floor, this sets the limit for meaningful He ion fluences when irradiating SNSPDs. Surprisingly, one of the 12 nm/400 ions nm^{-2} detectors shown in Figure 2.4 exhibits a high SDE although I_{sw} was lower than expected for these two SNSPDs. This hints to a relatively homogeneous current density within the nanowire that allows biasing close to the depairing current density and thus achieving high SDE. This understanding of how He ion irradiation influences detection efficiency and switching current is crucial to the local irradiation technique for current crowding mitigation developed in Chapter 3.

Another key metric for SNSPDs is their recovery time since it determines the detector's maximum count rate. It can be estimated from the time constant τ_{d} of the exponential decay of a detection voltage pulse [11, 60]. Figure 2.5 shows how the measured decay time increases with increasing He ion fluence and demonstrates that it is smaller for thicker detectors. These observations can be understood as follows: The decay time depends on the kinetic inductance L_{k} of the detector by $\tau_{\text{d}} = L_{\text{k}}/R_{\text{load}}$ with a typical load resistance of $R_{\text{load}} = 50\,\Omega$ for the readout electronics [60]. At the same time, the kinetic inductance L_{k} of a thin ($d \ll \lambda_{\text{eff}}$) and dirty ($\ell \ll \xi_0$) superconducting film of length l, width w, and thickness d is given by

$$L_{\text{k}} = \mu_0 \lambda_{\text{eff,tf}} \frac{l}{w} \,, \tag{2.1}$$

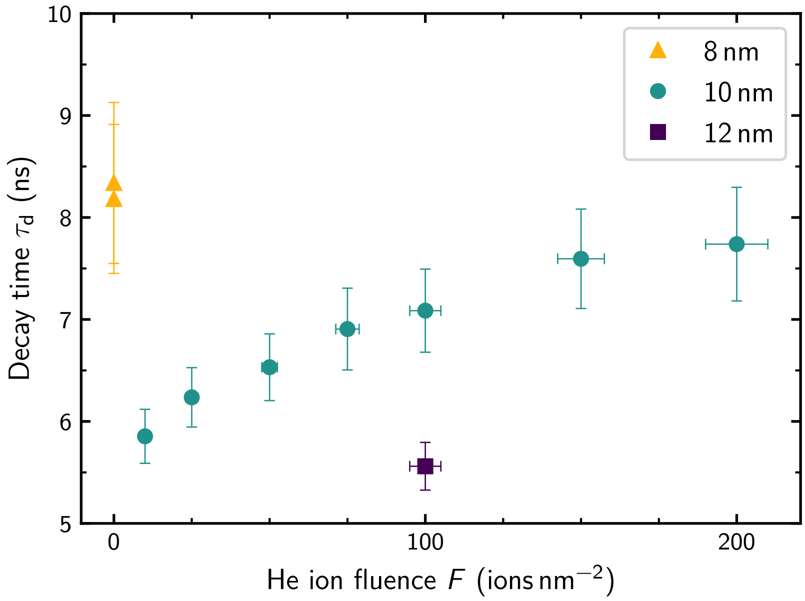

Figure 2.5: Decay time vs. He ion fluence, including statistical errors. τ_d increases with increasing fluence and decreasing thickness due to the resulting higher kinetic inductance of the detector. Adapted from [111], used under CC BY 4.0.

with the effective magnetic penetration depth for thin films $\lambda_{\mathrm{eff,tf}} = \lambda_{\mathrm{eff}}^2/d$ as introduced by Pearl [138], where λ_{eff} is the effective magnetic penetration depth of a dirty bulk superconductor like NbTiN, given by

$$\lambda_{\mathrm{eff}} = \lambda_{\mathrm{L}}\sqrt{\frac{\xi_0}{\ell}} = \sqrt{\frac{\hbar\rho}{\pi\mu_0 \Delta(0\,\mathrm{K})}} \tag{2.2}$$

according to Bartolf [139, Eq. (9.36)]. Here, λ_{L} is the London penetration depth, ξ_0 the BCS coherence length, ℓ the mean free path, ρ the specific resistivity of the superconducting film in the normal conducting state, and $\Delta(0\,\mathrm{K})$ the superconducting energy gap.[1] Hence, with the effective magnetic penetration depth one can express the kinetic inductance as

$$L_{\mathrm{k}} = \mu_0 \frac{\lambda_{\mathrm{eff}}^2}{d}\frac{l}{w} = \frac{\hbar R_{\mathrm{sheet}}}{\pi\Delta(0\,\mathrm{K})}\frac{l}{w}\,. \tag{2.3}$$

Thus, for detectors of similar length and width, the kinetic inductance and the decay time are smaller for detectors that exhibit a smaller sheet resistance, for example due to the use of a thicker film or due to less irradiation with He ions. In this way, we conclude that the increase of decay time due to irradiation can be compensated to a certain extent by using thicker films.

[1]For a detailed derivation of Equations (2.1) and (2.2) see also the book of Tinkham [140, Eqs. (3.120), (3.137), and (6.67b)].

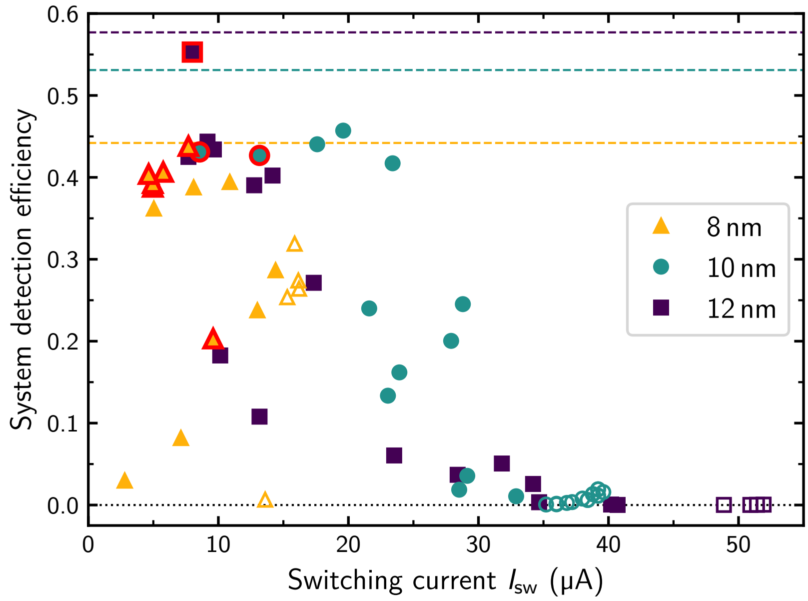

Figure 2.6: Maximum system detection efficiency vs. switching current for the three detector thicknesses studied in this chapter. The simulated maximum SDE of each thickness is indicated by dashed lines, while saturating SDE is highlighted by symbols with a red frame; open symbols represent unirradiated devices. The relative uncertainties of SDE and switching current are 2 % and 6 %, respectively (error bars not shown for clarity). Moreover, the SDE measurements were performed at a wavelength of 780 nm. Noteworthy are the data points at an SDE ≈ 45 % where the 10 nm SNSPDs provide a similar SDE like the 8 nm ones but offer the doubled switching current. Furthermore, for a similar I_{sw} of about 8 µA, one 12 nm SNSPD shows up to 55.3 % SDE, whereas the 8 nm ones provide only up to 43.8 % SDE. Adapted from [111], used under CC BY 4.0.

For practical applications beyond laboratory characterization, we developed a dipstick cryostat and a robust fiber-coupling solution that maintains optical alignment during thermal cycling to cryogenic temperatures. This plug-and-play fiber-coupled SNSPD system, detailed in Appendix F, enables reliable deployment of these enhanced detectors without requiring complex alignment procedures. Beyond stable optical coupling, simultaneously high SDE and I_{sw} are essential for practical applications since a higher I_{sw} yields larger voltage pulses, which reduces both the requirements for pulse detection with the readout electronics and the timing jitter induced by electrical noise [28, 122]. To compare these two performance metrics, Figure 2.6 shows the SDE against I_{sw} (open symbols representing the unirradiated detectors, a red frame highlighting saturating SDE, and dashed lines indicating the simulated SDE upper limit). It is interesting to note how I_{sw} and SDE compare between the 8 nm and the 10 nm devices with an SDE between 39 % and 46 %: While providing a similar efficiency, the 10 nm devices offer twice as much switching current, 20 µA instead of 10 µA. This I_{sw} is also higher than that of the unirradiated 8 nm detectors. Another comparison can be drawn between the 8 nm SNSPDs with saturating SDE close to

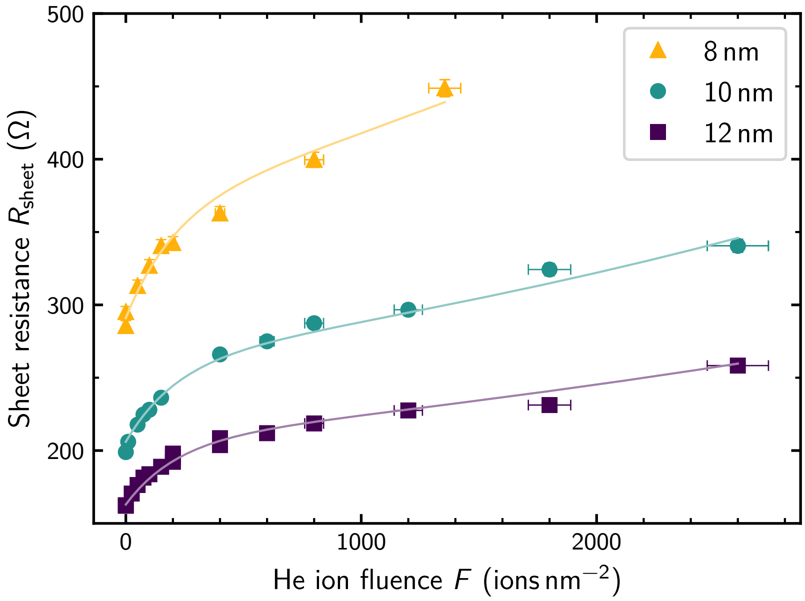

Figure 2.7: Sheet resistance vs. He ion fluence for 8 nm, 10 nm, and 12 nm film thickness, including statistical errors. The sheet resistance increases with He ion fluence and decreasing film thickness. All three data sets are described by the fit function given by Equation (2.7) with the parameters of Table 2.1. Adapted from [111], used under CC BY 4.0.

44 % and the 12 nm SNSPD showing 55.3 % SDE: at similar switching currents of about 8 µA, the 12 nm SNSPD provides a substantially higher SDE. Furthermore, it is noteworthy that the shift of the data point clouds in this two-dimensional parameter space is not monotonic to higher I_{sw} with higher thickness (except for the unirradiated devices). This could hint to the existence of an optimum thickness between 8 nm and 12 nm to reach simultaneous high SDE and I_{sw} via He ion irradiation: On the one hand, an increasing detector thickness results in an increase of switching current and absorption (see Appendix A). On the other hand, thicker films exhibit a lower sensitivity to actually detect an absorbed photon.

To conclude, by choosing a suitable detector thickness and He ion fluence, one can tune I_{sw} and SDE, even to better performance in both parameters simultaneously compared to unirradiated detectors. Moreover, by individual irradiation of NbTiN SNSPDs with a suitable He ion fluence, one can intentionally modify the performance of selected detectors or even mitigate differences between nominally identical devices.

2.3.2 Scaling of thin film metrics with He ion fluence

To investigate how He ion irradiation impacts upon the bare NbTiN film metrics such as critical temperature T_c, sheet resistance R_{sheet}, and electron density n_e, we fabricated cloverleaf structures together with the detectors on the same sample to perform magneto-transport measurements in van-der-Pauw geometry. In Figure 2.7

we present the dependence of the sheet resistance R_{sheet} on the He ion fluence. As expected, R_{sheet} is higher for thinner films and increases with increasing He ion fluence as the number of defects in the NbTiN film increases. Interestingly, the sheet resistance does not scale as $R_{\text{sheet}} = \rho/d_0$ with the nominal film thickness d_0 as expected if all samples had the same specific resistivity ρ. Even if one subtracts a 1.3 nm thick layer of oxidized NbTiN [131] from the nominal NbTiN thickness, the resulting resistivities of the unirradiated films are still lower for the thicker films than for the 8 nm film (1.94 µΩ m, 1.73 µΩ m, and 1.73 Ω m for the 8 nm, 10 nm, and 12 nm films, respectively). Although one might expect R_{sheet} to saturate at high fluences due to a saturating defect density in the film, we experimentally observe a continuous increase of R_{sheet} with He ion fluence. This could have its origin in noticeable surface sputtering [141] and intermixing [142] at the film/substrate interface by the impinging He ions and an associated reduction of the effective film thickness.

Based on these observations and taking the sheet resistance to be directly proportional to the defect density, we develop a simple physical model. In our model, each ion that passes through the film can create a defect cluster of an average volume v_{D} with an efficiency η. Moreover, we consider the film volume V as divided into many volume elements v_i with the same size as the average defect cluster volume v_{D}, and defect clusters may only be created in volume elements that do not already contain a defect cluster. Those considerations imply that irradiating a film of volume V, thickness d, and area A using a He ion fluence ΔF creates ΔN_{D} new defect clusters according to

$$\Delta N_{\text{D}} = \left(\frac{V - N_{\text{D}}\, v_{\text{D}}}{V}\right)\left(\frac{d}{\sqrt[3]{v_{\text{D}}}}\right)\eta\, A\, \Delta F\ . \tag{2.4}$$

The first fraction represents the fraction of V that does not yet contain defect clusters, the second fraction represents the number of potential defect clusters that an impinging ion could create when passing the film along its thickness. Dividing this equation by the total volume V to obtain an expression for the defect cluster density n_{D} and taking the limit $\Delta F \to 0$ yields

$$\frac{\mathrm{d}n_{\text{D}}}{\mathrm{d}F} = \frac{\eta}{\sqrt[3]{v_{\text{D}}}}\left(1 - v_{\text{D}}\, n_{\text{D}}(F)\right)\ . \tag{2.5}$$

This differential equation has the solution

$$n_{\text{D}}(F) = \frac{1}{v_{\text{D}}}\left(1 - (1 - n_{\text{D},0}\, v_{\text{D}})\, e^{-\eta v_{\text{D}}^{2/3} F}\right)\ , \tag{2.6}$$

where $n_{\text{D},0}$ is the defect cluster density of the unirradiated film. We relate the defect cluster density to the specific resistivity ρ via direct proportionality with a film-thickness dependent constant a_{d_0}. To arrive at a model for the sheet resistance,

Table 2.1: Fit parameters of the physical model according to Equation (2.7), describing the data in Figure 2.7. For each thickness, the fit function has its own fit parameter a_{d_0}/v_D, while the other parameters are independent of film thickness and therefore shared between the three fit functions. Reproduced from [111], used under CC BY 4.0.

d_0 (nm)	a_{d_0}/v_D (Ω)	$n_{\mathrm{D},0}\, v_\mathrm{D}$ (1)	$\eta v_\mathrm{D}^{2/3}$ (nm^2)	r_s (nm/(ions/nm^2))
8	2957 ± 36			
10	2618 ± 36	0.79 ± 0.01	$(4.7 \pm 0.7) \times 10^{-3}$	$(9.4 \pm 0.6) \times 10^{-4}$
12	2484 ± 32			

we further account for the previously mentioned surface sputtering due to He ion bombardment by including an effective reduction of the original film thickness d_0 with a sputtering rate r_s and conclude

$$R_\mathrm{sheet}(F) = \frac{1}{v_\mathrm{D}} \left(1 - (1 - n_{\mathrm{D},0}\, v_\mathrm{D})\, e^{-\eta v_\mathrm{D}^{2/3} F}\right) \frac{a_{d_0}}{d_0 - r_\mathrm{s} F} \,. \tag{2.7}$$

We fit this model to the experimental data and present the results of this fitting in Figure 2.7. Since the sputtering rate r_s and the factors $n_{\mathrm{D},0}\, v_\mathrm{D}$ and $\eta v_\mathrm{D}^{2/3}$ contain only thickness-independent quantities, we choose these factors as common fit parameters for all three thicknesses. In this way, a_{d_0}/v_D is the only individual fit parameter for each thickness, while the other three previously mentioned parameters are shared between all films. As such, we fit the three data sets with six parameters. Table 2.1 lists the parameters that result in the fit functions shown in Figure 2.7. Considering the volume V as divided into many volume elements v_i with the same size as the average defect cluster volume v_D, the parameter $n_{\mathrm{D},0}\, v_\mathrm{D}$ can be qualitatively interpreted as the fraction of volume elements of the unirradiated film that contains transport-related defective regions such as grain boundaries and scattering centers. We obtain $n_{\mathrm{D},0}\, v_\mathrm{D} = 0.79$, indicating that the initial defect cluster density is high and/or the average volume of a defect cluster induced by a single He ion collision is on the order of the NbTiN grain size. A high defect density is not unexpected for a polycrystalline material such as NbTiN, and a defect cascade induced by a single He ion can extend over a volume similar to the NbTiN grain size (few nm) according to a study of He ion irradiation induced defect clusters in copper [143]. Within this model, the high value of 0.79 for $n_{\mathrm{D},0}\, v_\mathrm{D}$ means that most of the volume elements v_i are not available for modification by He ion irradiation. Furthermore, the quantity $\eta v_\mathrm{D}^{2/3}$ can be understood as the cross-section determining the probability that an impinging He ion creates a defect cluster of volume v_D. Moreover, the sputtering rate of 9.4×10^{-4} nm/(ions/nm^2) implies that an irradiation by 1000 ions nm^{-2} leads to an effective reduction of the NbTiN film thickness by about 1 nm. Although Zhang *et al.* [104] did not observe a change in

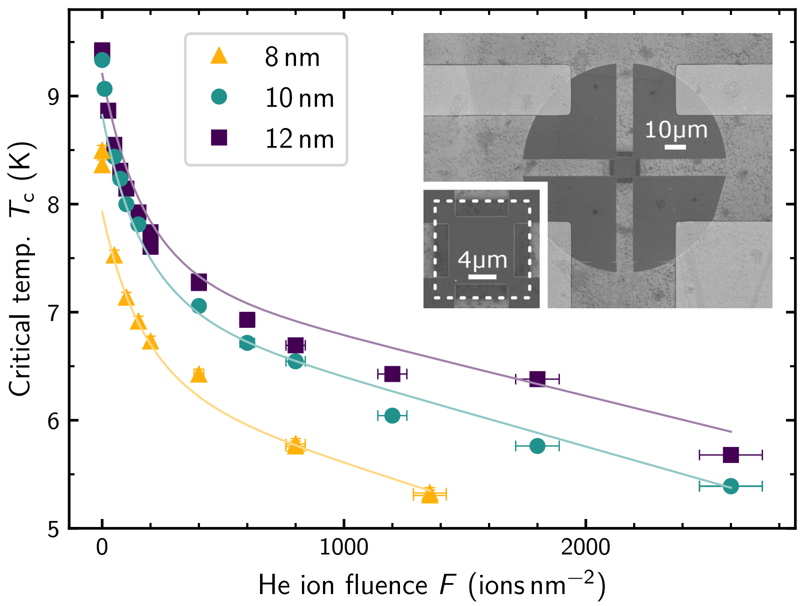

Figure 2.8: Critical temperature vs. He ion fluence, including statistical errors. T_c decreases with He ion fluence, with the reduction in T_c at small fluences being the strongest. Surprisingly, T_c for the unirradiated 10 nm and 12 nm films are similar for small fluences, although T_c is typically higher for thicker films. The continuous functions we determined by fitting the T_c and R_{sheet} data with the universal scaling law introduced by Ivry *et al.* [145], $d_0 T_c = A R_{sheet}^{-B}$, and subsequently using our physical model for R_{sheet}, given by Equation (2.7), as input to the universal scaling law. The inset shows an overview and a close-up view of the active area of an irradiated CL used for magneto-transport measurements (irradiated area highlighted by a white dashed square). Adapted from [111], used under CC BY 4.0.

thickness after irradiating their NbN film with 500 ions nm^{-2}, our observation agrees well with the simulated and experimentally observed sputtering yield of typically 1 nm per 1000 ions nm^{-2} found in literature [141, 144].

Figure 2.8 shows the dependence of the critical temperature T_c on the He ion fluence for 8 nm, 10 nm, and 12 nm thick films. Clearly, T_c decreases continuously by about 30 % from the unirradiated film to the film irradiated with 1200 ions nm^{-2}. Similarly to R_{sheet}, also T_c decreases most strongly for small He ion fluences. Interestingly, the measured values of T_c for the 10 nm and 12 nm films are very similar for low He ion fluences, although we would expect a lower T_c for the thinner film due to the suppression of superconducting properties when transitioning from bulk to the nanoscale [62, 146, 147]. Furthermore, we fit our experimental data for T_c and R_{sheet} with the universal scaling law introduced by Ivry *et al.* [145], $d_0 T_c = A R_{sheet}^{-B}$, which relates critical temperature, sheet resistance, and film thickness. Combining then the resulting fit function $T_c(R_{sheet}, d_0)$ with our physical fit function for R_{sheet}, Equation (2.7), we obtain the fits shown in Figure 2.8. Appendix B contains details of the fitting procedure used for T_c and discusses the subtleties involved in interpreting the effective film thickness change due to He ion irradiation for R_{sheet} and T_c. A recent publication by

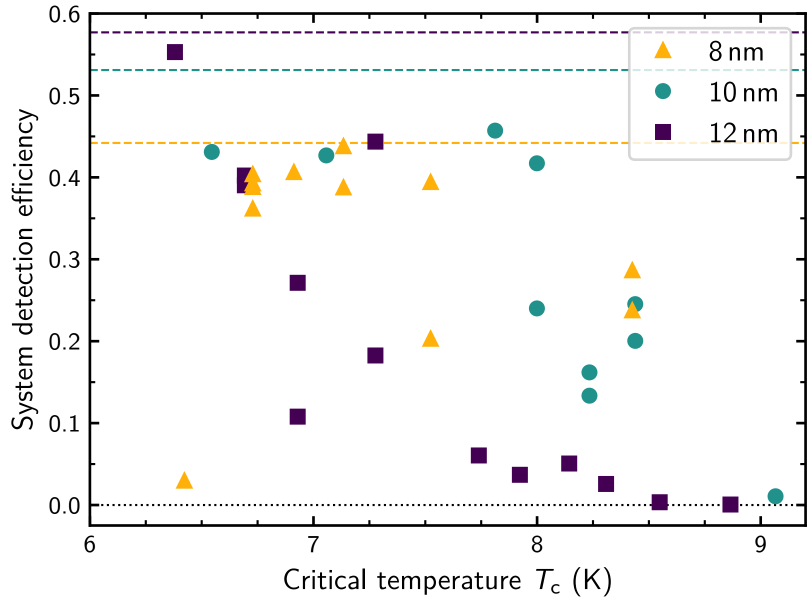

Figure 2.9: SDE of differently irradiated SNSPDs vs. T_c of corresponding CLs of three different thicknesses. The relative uncertainty of the SDE is 2 %, the uncertainty of the temperature amounts to 50 mK (error bars not shown for clarity). Furthermore, the SDE measurements were performed at a wavelength of 780 nm.

Ruhtinas & Maasilta [148] contains a study of the critical temperature and the critical current density of comparably thick, 35 nm and 100 nm, NbTiN bridges, in which they suppressed superconductivity by He ion irradiation of a narrow line perpendicular to the bridge. Empirically, they observed a logarithmic dependence of T_c and an exponential dependence of j_{sw} on the He ion fluence F. As shown in Figure B.3 in Appendix B, a fit of our data for the critical temperature with $T_c(F) = -a \log(F+b)+c$ and fit parameters a, b, and c for each of the three thicknesses describes our data even a bit better than the universal scaling law. However, using the universal scaling law, we need only the two fitting parameters A and B to describe all three data sets, while the empirical logarithmic fit function requires three fitting parameters for each thickness, a total of nine parameters for our three data sets. Moreover, our data for j_{sw} as shown in the inset of Figure 2.3 indicates that the switching current density does not follow the exponential dependence observed by Ruhtinas & Maasilta [148], especially for the smaller He ion fluences. However, we note that compared to our work, Ruhtinas & Maasilta [148] studied the switching current density for higher fluences, ranging from 2×10^4 ions nm^{-2} to 12×10^4 ions nm^{-2}. Furthermore, since the film thickness has a strong influence on T_c, an interesting question is how the detectors' T_c compares between a thicker, higher irradiated SNSPD with a thinner, lower irradiated detector that both show a similar SDE. To this aim, we compare the detector's SDE with the thin-film T_c in Figure 2.9. The data suggests that with 44 % the 10 nm detectors can actually reach an SDE comparable to the 8 nm SNSPDs, while retaining a T_c of 8 K

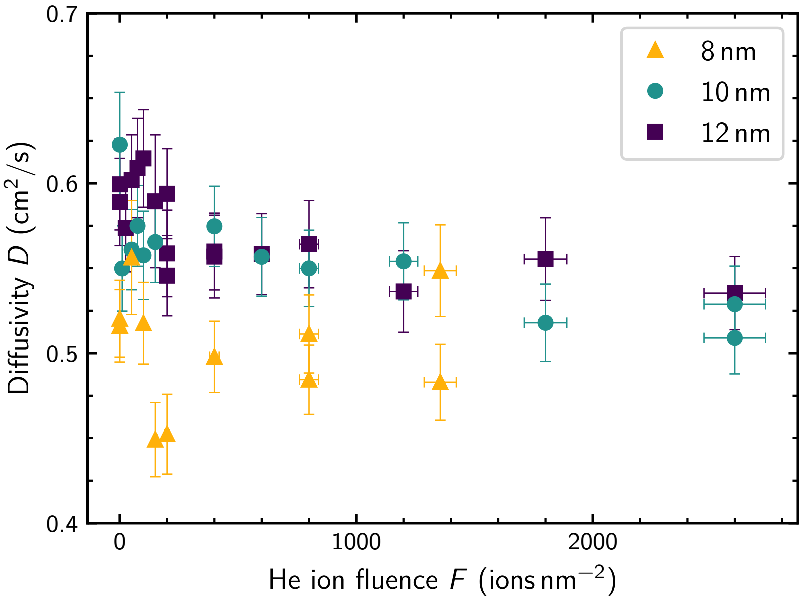

Figure 2.10: Quasiparticle diffusivity vs. He ion fluence, including statistical errors. D is almost constant within the error bars, and averaging over all fluences reveals the thickness dependence of D. One might see a slight decrease of D with increasing fluence, which could be explained by the thickness reduction due to sputtering during He ion irradiation and the thickness dependence of D. Adapted from [111], used under CC BY 4.0.

instead of 7.5 K. This can be particularly useful for applications because a higher T_c reduces the requirements for the cooling system to operate the SNSPDs.

Next, we investigate whether there is a systematic change of quasiparticle diffusivity D or electron density n_e with increasing He ion fluence. In addition to D and n_e being fundamental properties of the film, a reduction in diffusivity for example would result in a higher cut-off wavelength of photons detectable with the SNSPD and increase its sensitivity to single photons [49, 149]. For this, we measured the temperature dependence of the upper critical magnetic field $B_{c2}(T)$ by performing magneto-transport measurements while varying the temperature. From linear fits of $B_{c2}(T)$ close to T_c, we extract the slope $\mathrm{d}B_{c2}/\,\mathrm{d}T$ and calculate the diffusivity [129]

$$D = \frac{4k_B}{\pi e}\left[\frac{\mathrm{d}B_{c2}}{\mathrm{d}T}\right]^{-1}_{T\to T_c} . \qquad (2.8)$$

Magnetic field sweeps were also performed with the film in the normal conducting state and at constant temperature, while measuring the Hall voltage V_H. Since V_H varies linearly with the applied magnetic field B and measurement current I, we determine the Hall coefficient $R_H = V_H d_0/(IB)$ using the slope of a linear fit of the $V_H(B)$ data. From this, we estimate the electron density n_e according to $R_H = -1/(n_e e)$ within the free electron model (see also [128, 129, 150]). Figures 2.10 and 2.11 show the

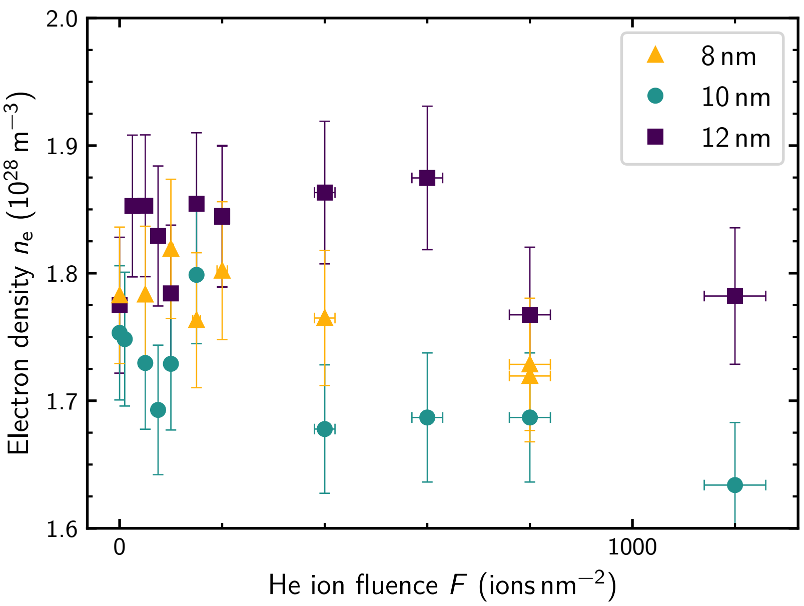

Figure 2.11: Electron density vs. He ion fluence, including statistical errors. Despite fluctuations between measurements, n_e seems almost constant. One might see a slight decrease with increasing He ion fluence, which could be explained by the thickness dependence of n_e and the reduction of the effective film thickness during irradiation due to sputtering. Adapted from [111], used under CC BY 4.0.

quasiparticle diffusivity and the electron density as a function of the He ion fluence. Both are almost constant within the experimental error bars, although one might see a slight decrease of the diffusivity and the electron density with increasing He ion fluence. Since we usually observe decreasing electron density and diffusivity with decreasing film thickness like Sidorova *et al.* [128], this may be related to the observed effective thickness reduction of 0.94 nm per 1000 ions nm^{-2} due to sputtering during He ion irradiation.

2.4 Summary and outlook

In summary, this chapter demonstrated the use of a He ion microscope for precise, site-selective tuning of the performance metrics of individual SNSPDs fabricated on the same chip. At the same time, our results demonstrated the possibilities of using thick (up to 12 nm) NbTiN films and He ion irradiation to enhance performance metrics such as system detection efficiency, switching current, decay time, and operating temperature compared to SNSPDs of smaller thicknesses. Thicker detectors exhibit higher optical absorption efficiency and shorter decay times as compared to similar SNSPDs fabricated from thinner films. However, due to the reduction of single-photon sensitivity with detector thickness, such SNSPDs typically offer only small detection efficiencies. Here, we have shown how He ion irradiation can boost the initially negligible SDE ($< 0.05\,\%$) of 12 nm thick SNSPDs by three orders of magnitude to 55.3 % for a wavelength of 780 nm and at 4.5 K, resulting in an internal detection efficiency just within the saturated regime. This enables the use of thicker films and the associated advantages—at temperatures reachable with standard pulse-tube or Gifford-McMahon cryocoolers [151]. Furthermore, we found that by combining He ion irradiation and detectors fabricated from thicker films, one can enhance SDE and I_{sw} while reducing the decay time compared to unirradiated smaller-thickness SNSPDs. While reduced decay times result in increased maximum count rates, higher I_{sw} and the associated higher detection voltage pulse imply a higher signal-to-noise ratio, which reduces the electrical noise induced timing jitter [28] and the necessary amplification of the electrical readout circuit.

Using a He ion microscope to irradiate individual detectors and cloverleaf structures on the same chip with different fluences allowed us to precisely study SNSPD and film properties over He ion fluences ranging from $0\,\mathrm{ions\,nm^{-2}}$ to $2600\,\mathrm{ions\,nm^{-2}}$, avoiding any errors that could arise from the high sensitivity of device properties on the exact sputtering or the subsequent fabrication process. We found that the increase of sheet resistance with the He ion fluence can be well described by a simple physical model that includes defect generation in the NbTiN film and an effective reduction of thickness due to sputtering during He ion bombardment. Moreover, the decrease of critical temperature with the He ion fluence can be described by combining our physical model for R_{sheet} with the universal scaling law from Ivry *et al.* [145], which relates critical temperature, film thickness, and sheet resistance. At the same time, the quasiparticle diffusivity and electron density stay almost constant for the He ion fluences studied in this chapter. These magneto-transport measurements also show that irradiation of SNSPDs with He ions continuously changes their properties—although one can employ irradiation to enhance the SNSPD performance, excessive He ion irradiation ultimately leads to a vanishing, non-detectable signal when a photon is absorbed, rendering the SNSPD inoperative. These findings could be particularly interesting for applications where SNSPDs are exposed to radiation and high-energy particles [21].

Besides the general enhancement of performance metrics of NbTiN SNSPDs by using thicker films combined with He ion irradiation, one can use targeted irradiation of individual devices with a He ion microscope for example in large SNSPD arrays to mitigate inhomogeneities of detector performance between pixels (or even dark pixels). This would be challenging without a post-processing technique such as site-selective He ion irradiation. Furthermore, targeted He ion irradiation enables the optimization of detectors for different performance metrics on the same chip, also after fabrication.

Having established site-selective He ion irradiation as a powerful technique for enhancing individual SNSPDs, Chapter 3 extends this approach to the sub-device level, specifically addressing the long-standing challenge of current crowding. Chapter 4 then unravels the physical mechanisms underlying these irradiation-induced enhancements, revealing the unexpected and significant role of substrate modification in detector performance.

3 Eliminating current crowding in SNSPDs via local He ion irradiation

Building upon the enhancement of SNSPDs via He ion irradiation established in Chapter 2, this chapter addresses current crowding—a fundamental limitation where increased current density in the bends of meander-shaped SNSPDs restricts the maximum applicable bias current and consequently limits detection efficiency, dark count rate, and timing resolution. We demonstrate a novel approach that not only eliminates current crowding but simultaneously enhances detector sensitivity. By locally irradiating the straight segments of SNSPDs sufficiently with He ions while leaving the bends unirradiated, the critical current of the straight segments becomes lower than that of the bends, removing current crowding as the limiting factor on detector performance. Our approach yields significantly wider detection efficiency plateaus compared to fully irradiated devices, allowing operation at lower bias currents with reduced dark count rates while maintaining high efficiency (e. g., 94 % efficiency with 7 mHz dark count rate). Unlike other techniques that require compromises in device geometry, our method is compatible with arbitrary designs. These findings demonstrate how precisely controlled irradiation patterns can overcome longstanding physical limitations in SNSPD design. The microscopic mechanisms behind these enhancements will be explored in Chapter 4.

The research presented in this chapter has been published as Strohauer, S. et al. *Current Crowding–Free Superconducting Nanowire Single-Photon Detectors.* Sci. Adv. ***11,*** *eadt0502 (2025), under a CC BY 4.0 license. The chapter largely follows this publication, with modifications to integrate it into the broader context of this thesis.*

Contents

3.1 Introduction

As elaborated in Section 1.1, SNSPDs are used in numerous disciplines due to their exceptional performance metrics. One strategy to further enhance their detection efficiency, dark count rate, and timing jitter is to reduce the effect of current crowding in their bends. Current crowding locally increases the current density in the bends, limiting the maximum applicable bias current through the detector, and thus limiting also the maximum achievable detection efficiency, dark count rate, and timing jitter [93, 94]. In literature, methods to reduce the effect of current crowding consist of optimized bend geometries [93–97], or increased superconductor thickness in the bends [98, 99]. The use of optimized bend geometries is either limited to relatively low-fill factor SNSPDs, which have lower absorption and detection efficiency, or requires a spiral or special meander design with significant wire length overhead, which is incompatible with dense SNSPD arrays and limits the timing properties of the detector. In contrast, variable thickness SNSPDs successfully reduce current crowding also for highly efficient and compact large fill factor SNSPDs. Building upon the site-selective He ion irradiation technique established in Chapter 2, this chapter introduces a novel method to obtain not only current crowding–free SNSPDs of arbitrary geometry and fill factor but also to simultaneously enhance their sensitivity.

3.2 Current crowding at low temperatures

Current crowding describes a non-uniform distribution of current density in an electrical conductor and has its origin for example in variations in material properties or device geometry. In the context of SNSPDs, current crowding leads to a local increase of the supercurrent density in the 180° bends and at kinks or discontinuities of the SNSPD. Once this current density exceeds the critical value for the superconductor, the SNSPD switches to the normal conducting state. This maximum current defines the switching

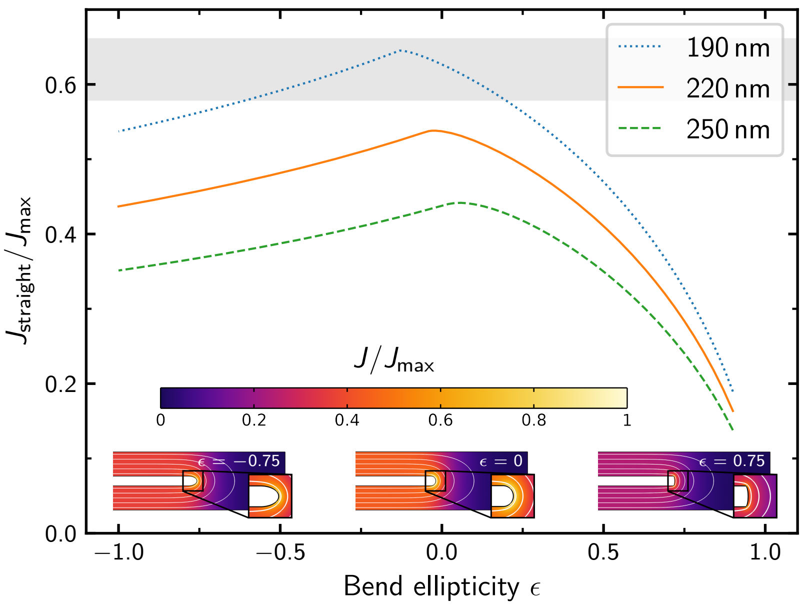

Figure 3.1: Simulated current crowding–induced reduction of the switching current in SNSPDs versus the ellipticity ϵ of the bends. The reduction is given by the ratio of the homogeneous current density in the straight parts and the maximum current density of the whole bend (located in the strongly curved regions). This ratio is calculated for three different wire widths ranging from 190 nm to 250 nm and a fixed pitch of 350 nm. The gray shaded area indicates the range between 58 % and 66 % to which the experimentally measured switching current of our SNSPDs is reduced compared to that of the straight wires. The three exemplary bend structures show the current density distribution throughout the bends for a wire width of 250 nm and different ellipticities. Adapted from [152], used under CC BY 4.0.

current I_{sw}. In other words, current crowding limits I_{sw} of the SNSPD.

To quantitatively understand this effect and since the shape of the 180° bends influences the severity of current crowding [93], we simulated how the ellipticity ϵ of the bends impacts the current distribution. Similar to the methodology described in the supporting information of [153], our approach is based on the fact that the supercurrent density fulfills the continuity equation for a steady current, $\nabla \cdot \mathbf{J} = 0$, and the London equation, $\nabla \times \mathbf{J} = 0$, in which the effects of the magnetic field are neglected [93, 153]. The supercurrent density can be described as the gradient $\mathbf{J} = \nabla u$ of a scalar potential u, since this specific formulation is generally valid when the current density satisfies the London equation ($\nabla \times (\nabla u) = 0$). Combining the definition $\mathbf{J} = \nabla u$ with the continuity equation, the scalar potential satisfies the Laplace equation $\Delta u = 0$. Since the electrostatics module of Comsol solves the Laplace equation for the electric potential, we use this module to calculate the supercurrent density $\mathbf{J}$. As boundary conditions we choose the gradient of the electric potential to match the bias current density at the inflow boundary (one end facet of the wire), $\nabla u = \mathbf{J}_{\text{bias}}$, and set $u = 0$ at the outflow boundary (the other end facet of the wire). For all other boundaries we set $\nabla u = 0$ to ensure no inward or outward current flow. For our simulations, we

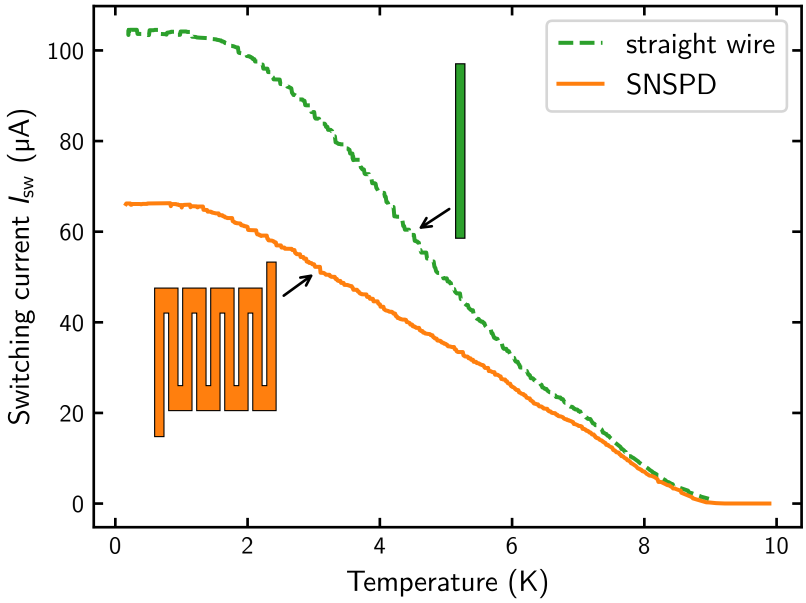

Figure 3.2: Switching current versus temperature for an SNSPD and a straight wire. Current crowding causes a reduced switching current for the SNSPD over the straight wire, especially towards low temperatures. Adapted from [152], used under CC BY 4.0.

define the ellipticity of the 180° bends of the SNSPD as $\epsilon = 1 - b/a$, with the semi-axis a being the vertical gap distance between the wires, and the semi-axis b defining the horizontal elongation of the bend. Moreover, we choose wire widths between 190 nm and 250 nm with a fixed pitch of 350 nm. While the detectors used in this chapter have a designed wire width of 250 nm, SEM measurements reveal an actual wire width of (220 ± 10) nm, as shown in the zoom-in of Figure 3.3b. Figure 3.1 shows the ratio of the homogeneous current density in the straight parts J_{straight} to the maximum current density of the whole bend J_{max}. The three exemplary bends of different ellipticity visualize the distribution of the normalized current density in the bend and show a maximum current density in the strongly curved regions. Especially as the bends approach a rectangular shape ($\epsilon \to 1$), these simulations show that current crowding drastically reduces this ratio, predicting a substantial limitation on the maximum achievable switching current.

It is worthwhile to note that the effect of current crowding is most pronounced at low temperatures ($< 0.7\,T_c$), while at temperatures close to T_c the switching current practically coincides for straight and bent wires due to the divergence of the coherence length at temperatures close to the critical temperature [136, 137]. To quantify the effect of current crowding for our devices, we measured the temperature dependence of the switching current for SNSPDs (in meander form with 180° bends) and straight wires (without any bend), both consisting of 250 nm wide and 8 nm thick NbTiN wires. As shown for two representative devices in Figure 3.2, the switching current increases and the effect of current crowding becomes more prominent towards low temperatures, reaching a saturating (relative) difference between I_{sw} of the straight wire and the SNSPD at temperatures below 1.6 K (1 K). In fact, at temperatures below 1 K, the switching current of NbTiN meander SNSPDs with a fill factor of 71 % and 250 nm wide wires is reduced to only 58 %–66 % of I_{sw} of corresponding straight wires.

Comparing the experimental measurements of our devices with the simulation results, we find that the measured reduction in switching current—indicated by the gray shaded area in Figure 3.1—aligns with our simulations for bends with near-zero ellipticity. Despite the fact that our detector design consists of rectangular bends in order to have a pronounced effect of current crowding for this study, SEM images such as the zoom-in of Figure 3.3b show that due to fabrication limitations, the actual bends have a relatively circular shape ($\epsilon \approx 0$). Comparing the corresponding simulation results with the experimentally measured reduction in switching current due to current crowding, we conclude that the experimental reduction is slightly smaller than expected. However, the effective wire width may be smaller than the width measured with the SEM due to oxidation [131] and fabrication limitations. Moreover, considering more streamline-shaped bends [93], the simulated ratio $J_{straight}/J_{max}$ would be a bit higher than in our simulations of elliptical bends. Both effects would result in a larger overlap between experiment and simulation. Furthermore, we conclude that SNSPDs with higher fill factors or sharper, more rectangular bends than those studied in our experiments would experience an even greater reduction in switching current due to increased current crowding.

At the same time, a high switching current, as close as possible to the limit set by the depairing current density, is desirable because it allows larger plateaus of saturating detection efficiency [28, 154]. This makes operation with high detection efficiency at simultaneously low dark count rates possible. Moreover, high switching currents allow high bias currents through the SNSPDs that yield high and easily detectable voltage pulses and low timing jitter [99]. Since high switching currents are reached for low temperatures where current crowding limits the maximum applicable bias current, a method to avoid current crowding would be highly advantageous. Moreover, current crowding–free SNSPDs are expected to exhibit fewer dark counts since they originate primarily from bends or constrictions with strong current crowding [95, 98, 155–157]. Compared to methods presented in literature that solely mitigate current crowding [93–99], this chapter introduces a solution to obtain current crowding–free SNSPDs of arbitrary geometry that simultaneously exhibit enhanced sensitivity.

3.3 Design and concept of current crowding–free SNSPDs with enhanced sensitivity

To demonstrate current crowding–free SNSPDs of enhanced sensitivity, we build on the relationship between He ion fluence and SNSPD properties established in Chapter 2. We combine the two effects of reduced switching current and enhanced sensitivity of SNSPDs after He ion irradiation [104, 111]. As discussed in the previous section, the 180° bends are the main contribution to current crowding in a meander-type SNSPD, thus limiting its switching current. By locally irradiating only the straight segments of the SNSPD while leaving its bends unirradiated, we reduce the critical current density of the straight segments while making them simultaneously more sensitive to single photons. Once the He ion fluence is large enough, the critical current of the straight segments with homogeneous current density will be lower than the critical current of the bends. Then, one can expect the overall critical current (or switching current) of the SNSPD to be given by the critical current of the straight segments and not being limited by current crowding anymore. To investigate this hypothesis, three types of devices as shown in Figure 3.3a were fabricated on the same chip: SNSPDs that were *locally* (only their straight segments) or *fully* irradiated, as well as *straight wires* without any bend. Following the methods in Sections 1.5 and 2.2, they were fabricated from an 8 nm thick NbTiN film on a Si substrate with 130 nm thermally grown SiO_2. The nominal design of the detectors consists of 250 nm wide nanowires in meander form with 100 nm gaps (fill factor 71 %) and covers an active area of 20 µm × 20 µm. The high fill factor of 71 % and a nominally rectangular design of the bends between neighboring nanowires of the SNSPDs were chosen to have a pronounced effect of current crowding. Although the actual bends have a relatively circular shape due to fabrication limitations (as shown in the zoom-in of Figure 3.3b), simulations in the previous section have demonstrated that this geometry is still strongly affected by current crowding. Similar to the detectors, the straight wires were designed to be 250 nm wide and fabricated on the same chip to ensure best comparability. All devices were pre-characterized in a cryogenic probe station (Janis) at 4.5 K. Subsequently, devices exhibiting a similar switching current were selected for wire bonding and further characterization at temperatures down to 150 mK in a closed cycle cryostat with adiabatic demagnetization refrigeration (kiutra GmbH). The development of the measurement platform and its design considerations used for this low-temperature regime is described in Appendix E, including the necessary special RF wiring and thermalization. Further characterization consisted of measuring the switching current of each device 10–250 times to determine a switching current distribution and its mean switching current at a temperature of 1 K. The switching current measurements were performed by ramping the bias voltage applied at a 50 kΩ resistor in series to the respective device and determining the current at which the total resistance increases by more than 1 kΩ. Temperature dependent switching current measurements were performed at temperature ramp rates of 0.075 K/min, ensuring that during one bias voltage sweep the temperature change was less than 0.1 K. After characterization of the unirradiated devices, a He ion microscope (Zeiss Orion Nanofab) with an acceleration voltage of 30 kV was used to irradiate them with He ions. An irradiation area of 25 µm × 15 µm was centered on the 20 µm × 20 µm detectors to homogeneously expose the straight segments of the nanowires while leaving the bends unirradiated. In this way, locally irradiated SNSPDs as shown in Figure 3.3a and b were obtained. For the reference straight wires, an irradiation area of 5 µm × 15 µm was chosen. Moreover, two detectors were fully irradiated (25 µm × 25 µm irradiation area). After irradiation, the devices were characterized again, and for several devices the process of irradiation and subsequent measurement was repeated multiple times.

3.4 Reducing current crowding by local He ion irradiation

As shown in Figure 3.3c and d, the mean switching current of locally irradiated SNSPDs stays constant for doses up to (90 ± 20) ions nm^{-2}, while it continuously decreases for fully irradiated SNSPDs and straight wires. As anticipated, locally irradiated SNSPDs exhibit a constant I_{sw} until the He ion fluence reaches a level that reduces I_{sw} of the straight wires to comparable values. Beyond this point, I_{sw} of locally irradiated SNSPDs and straight wires follow a similar curve. The slightly smaller I_{sw} of locally irradiated SNSPDs compared to that of the straight wires can be attributed to the higher likelihood of imperfections in one of the many straight segments of an SNSPD, unlike in a single straight wire.

Figure 3.4 shows the temperature dependence of the switching current for differently irradiated SNSPDs and straight wires. The data shown is the maximum of the switching current distribution measured at each temperature [59, 136]. The critical temperature decreases continuously with increasing He ion fluence in accordance with literature [104, 111] and does not depend on device type or irradiation type. For decreasing temperature, the $I_{sw}(T)$ curves start to differ and show a smaller slope for fully irradiated SNSPDs compared to that of locally irradiated SNSPDs and irradiated straight wires. Moreover, for similar He ion fluences and low temperatures, I_{sw} is much smaller for fully irradiated SNSPDs than for locally irradiated SNSPDs or straight wires. For example, at temperatures below 1 K and for a He ion fluence of 300 ions nm^{-2} it is only 30 µA instead of 40 µA. While for a He ion fluence of

Chapter 3

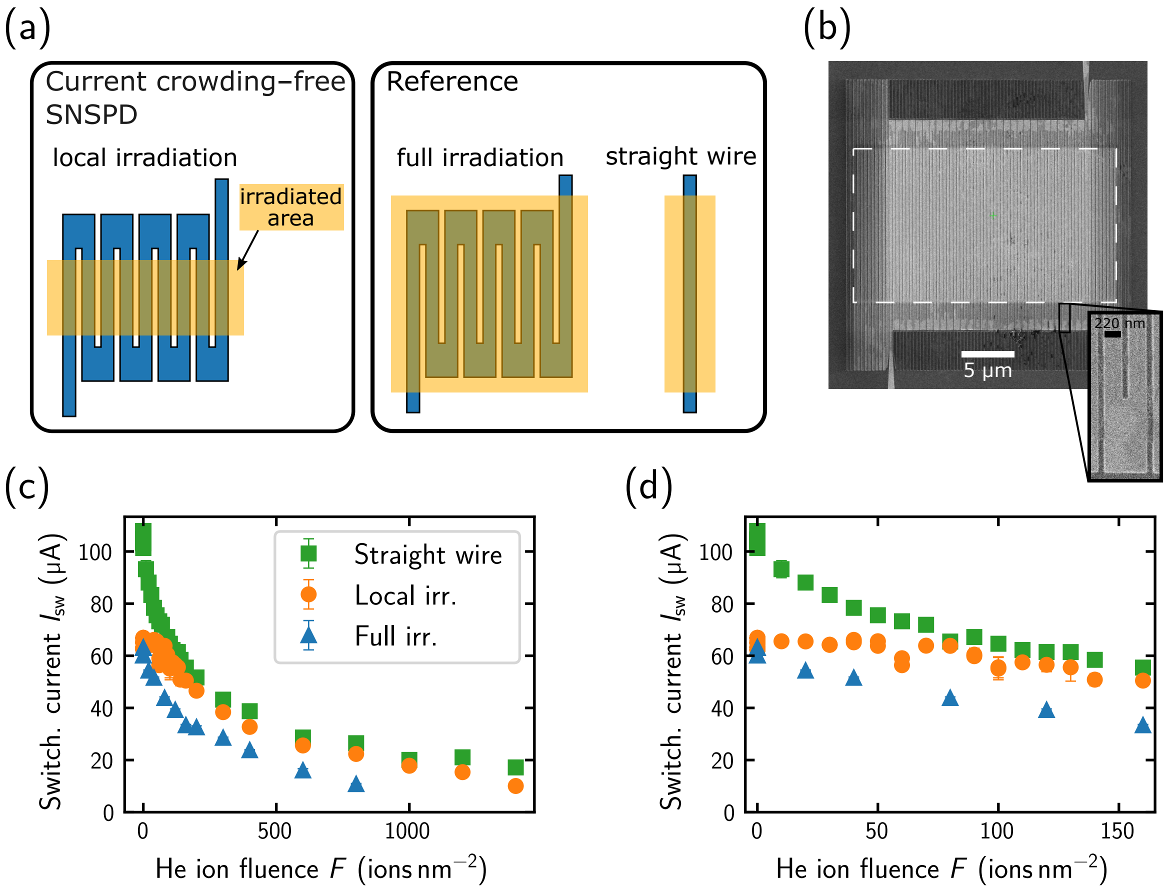

Figure 3.3: Current crowding–free SNSPDs. (a) Local irradiation of the straight detector segments is used to obtain current crowding–free SNSPDs. Fully irradiated SNSPDs and straight wires were fabricated as reference devices. (b) Scanning electron microscope image of an SNSPD after local irradiation. The irradiation area is indicated by the white dashed rectangle. (c), (d) Switching current versus He ion fluence for *locally* as well as *fully* irradiated SNSPDs and straight wires for the low fluence regime (c) and for the full measured range up a fluence of 1400 ions nm^{-2} (d). Adapted from [152], used under CC BY 4.0.

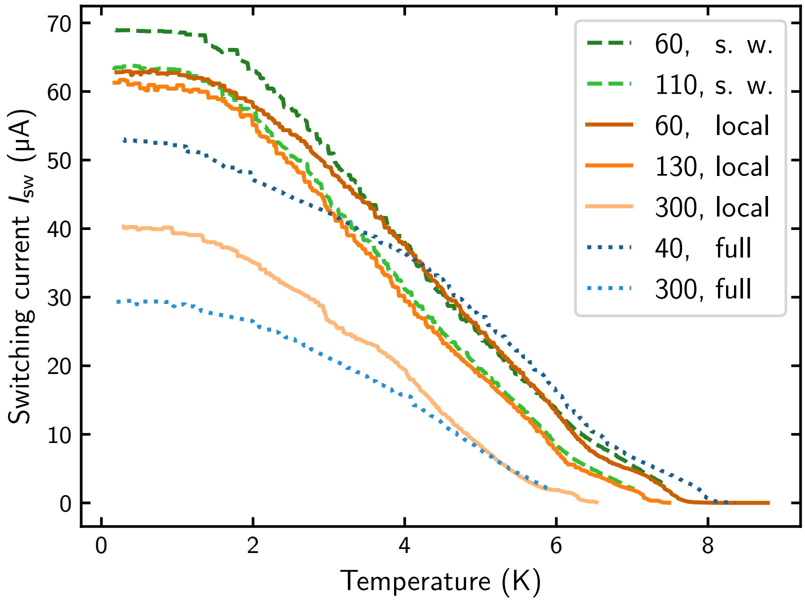

Figure 3.4: Switching current of straight wires (s. w.), locally irradiated SNSPDs (local), and fully irradiated SNSPDs (full) versus temperature. The He ion fluence used for irradiation is given by the numbers in front of the device type in units of ions nm^{-2}. Adapted from [152], used under CC BY 4.0.

60 ions nm^{-2} the switching current of the straight wire is still higher than that of the locally irradiated SNSPD, they almost coincide for the two fluences 110 ions nm^{-2} and 130 ions nm^{-2}. Those observations support the hypothesis that for small He ion fluences I_{sw} of the locally irradiated SNSPDs is not reduced, while it starts to coincide with that of the straight wires for fluences above (90 ± 20) ions nm^{-2}. In this case, the irradiation induced reduction of the switching current in the straight segments is the limiting factor for I_{sw} instead of current crowding in the bends. The stronger the effect of current crowding in the unirradiated device, the higher the He ion fluence required for local irradiation such that current crowding no longer plays a role. Since current crowding limits the switching current of SNSPDs more when the fill factor increases, this method is particularly useful for high fill factor or microscale SNSPDs, especially if the detector requires He ion irradiation anyway to become single-photon sensitive [43, 158].

3.5 Enhanced sensitivity of current crowding–free SNSPDs

In Chapter 2, we established that He ion irradiation enhances SNSPD sensitivity [104, 111]. The approach in this chapter, however, has an important distinction—by intentionally leaving the bends unirradiated while irradiating only the straight nanowire segments, we achieve enhanced performance through two complementary

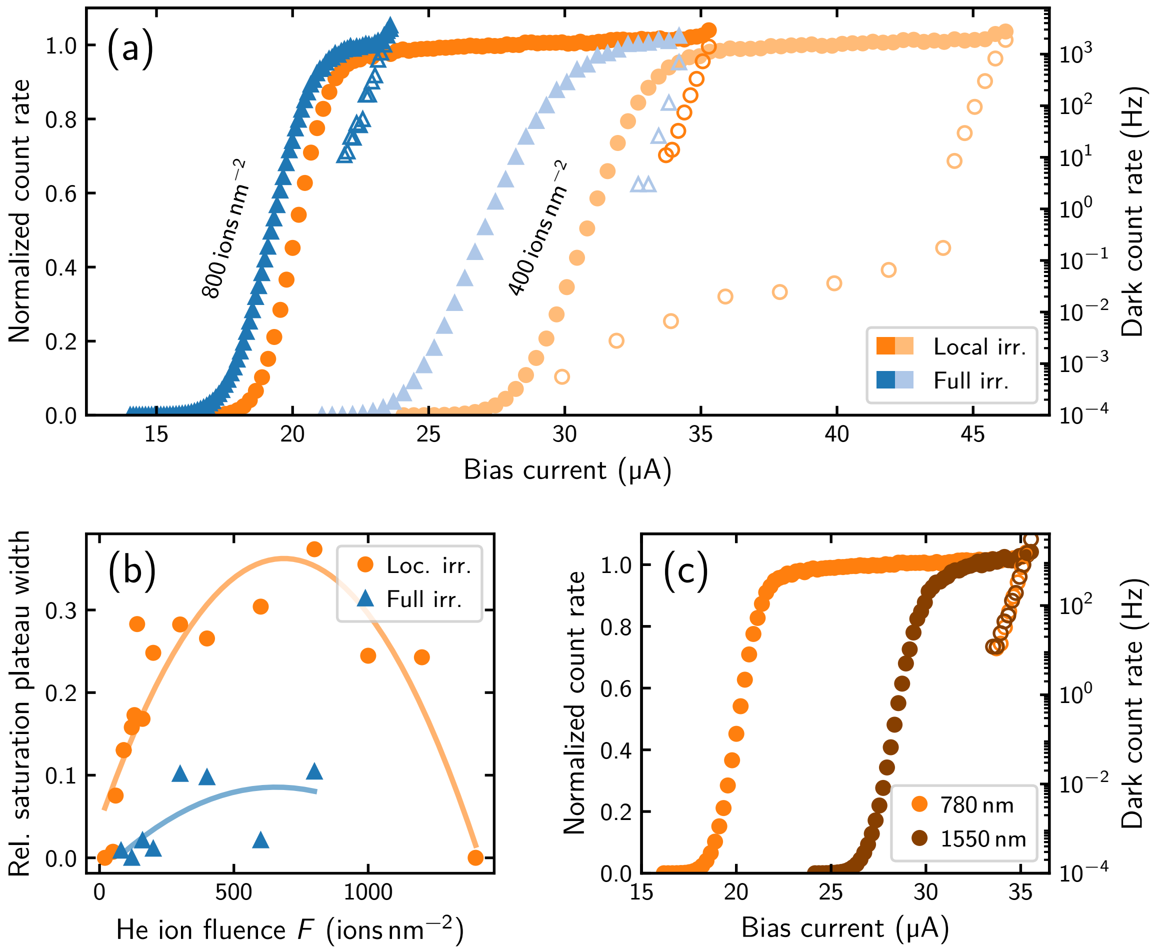

Figure 3.5: Detection performance of SNSPDs after local or full irradiation with He ions. (a) Normalized count rate (solid symbols) and dark count rate (open symbols) versus bias current after local (orange) or full (blue) irradiation with He ions. The He ion fluence used for irradiation is shown as annotations at the corresponding count rate curves. (b) Relative saturation plateau width versus He ion fluence after local or full irradiation, calculated according to Equation (3.1). The solid lines serve as a guide to the eye. (c) Comparison of the normalized count rate between photons of 780 nm and 1550 nm wavelength for a detector locally irradiated with 800 ions nm^{-2}. All shown dark count rate data was taken such that the integration time per data point was at least 10 times higher than the inverse of the measured dark count rate. All data shown was measured at a temperature of 1 K using photons with a wavelength of 780 nm, unless explicitly stated otherwise. Adapted from [152], used under CC BY 4.0.

effects: (1) the He ion irradiation induced higher sensitivity, and (2) the higher available bias currents compared to fully irradiated SNSPDs of the same He ion fluence. Figure 3.5a shows a comparison of the normalized count rates between two devices, one irradiated locally and one irradiated fully, both with the same He ion fluences. All data in Figure 3.5 was measured for photons of 780 nm wavelength and at a temperature of 1 K, unless explicitly stated otherwise. The locally irradiated SNSPD clearly shows higher switching currents and larger saturation plateaus of the count rates, for which the internal detection efficiency is unity. We note that, rather than a flat saturation plateau, the normalized count rate for the locally irradiated SNSPD shows a continuous, slight increase with increasing bias current. Due to scattering and recoil events of the He ions within the sample [110], we expect a gradual rather than abrupt decrease in sensitivity at the edges of the area scanned with the He ion microscope during irradiation. When the bias current is sufficiently high for the central region with homogeneous sensitivity to reach a saturating count rate, the edges of the irradiated area remain below saturation. As the bias current increases further, the count rate in these edge regions continues to increase, resulting in the observed slight increase in the overall count rate. The dark count rate at a certain bias current I_b mainly depends exponentially on the ratio $I_\mathrm{b}/I_\mathrm{sw}$. Therefore, the dark count rate of locally irradiated SNSPDs is lower than that of fully irradiated SNSPDs at similar absolute bias currents or normalized count rates. Since our SNSPDs exhibit very low dark count rates, we measured it over an extended period of time for selected devices. As shown in Figure 3.5a for the device locally irradiated with 400 ions nm^{-2}, we reach dark count rates of 7 mHz and 0.55 mHz at internal detection efficiencies of 94 % and 31 %, respectively. Also, the two regimes of intrinsic dark counts and dark counts originating from black body radiation are clearly visible: the first is given by the strongly current dependent contribution in the high current regime, while the second is the weaker current dependent contribution at lower currents [159]. The black body radiation induced dark count rate could be further suppressed by using cold band-pass filters [160].

In Figure 3.5b we present the relative count rate saturation plateau width, defined as

$$\sigma_\mathrm{rel} = \frac{I_\mathrm{c} - I_\mathrm{sat}}{I_\mathrm{c}} \,, \tag{3.1}$$

with the critical current I_c, and I_sat representing the current where the saturation plateau begins (where the normalized count rate reaches 0.95). The critical current is defined as the smallest bias current where the SNSPD shows non-zero resistance. Since we use a shunt resistor for the CR measurements to prevent latching of the detectors (20.4 Ω at 1 K), the SNSPDs transition to the relaxation oscillation regime at I_c before switching to the latching state [57]. Most importantly, the relative saturation

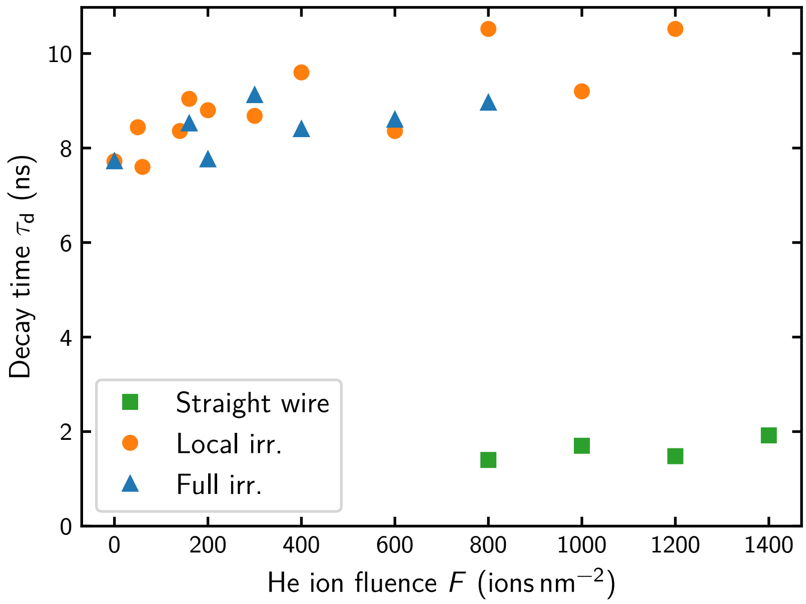

Figure 3.6: Decay time versus He ion fluence. The data shows locally irradiated SNSPDs together with fully irradiated SNSPDs and straight wires as reference devices. Adapted from [152], used under CC BY 4.0.

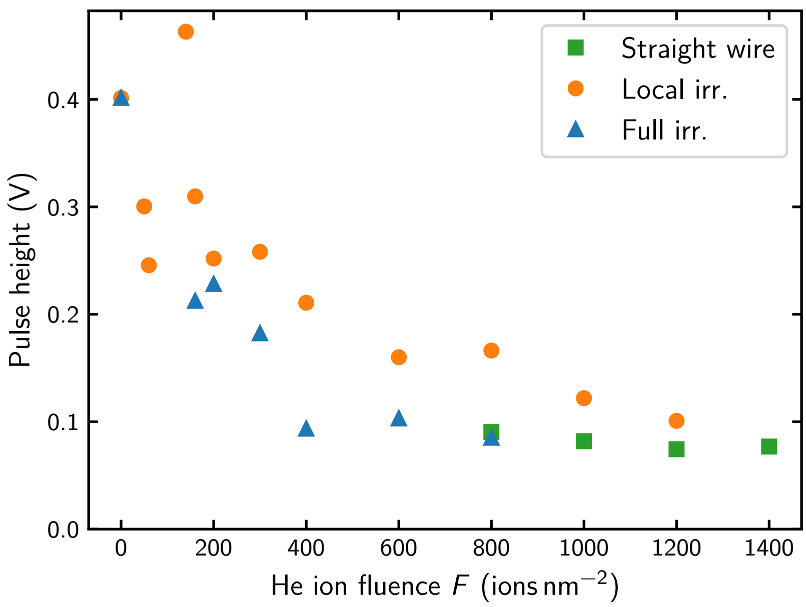

Figure 3.7: Pulse height versus He ion fluence. The data shows locally irradiated SNSPDs together with fully irradiated SNSPDs and straight wires as reference devices. Adapted from [152], used under CC BY 4.0.

plateau width is higher for locally irradiated SNSPDs compared to fully irradiated SNSPDs of the same He ion fluence. Furthermore, the relative saturation plateau width increases strongest as a function of He ion fluence for values smaller than 200 ions nm^{-2} and, as elaborated in more detail in Appendix C, it peaks between 600 ions nm^{-2} and 1000 ions nm^{-2} before it decreases again for higher fluences.

To assess the performance of the device locally irradiated with 800 ions nm^{-2} for optical communication in the C-band, we measured its normalized count rate for photons with a wavelength of 1550 nm and compare it in Figure 3.5c with its performance for 780 nm photons. For both wavelengths the detector shows saturating internal detection efficiency, even for 1550 nm where the onset of photon detection is shifted to higher bias currents due to the lower sensitivity to longer wavelength photons. Since it is the same device, the dark count rate is identical for both measurements.

The detection pulse height and the pulse decay time are further important performance parameters of single-photon detectors. More specifically, the recovery time determines the detector's maximum count rate and can be estimated from the time constant τ_d of the exponential decay of a detection voltage pulse [11, 60]. As shown in Figure 3.6, the decay time of all device types increases with increasing He ion fluence in agreement with previous measurements [111]. At the same time, the decay time of locally irradiated SNSPDs follows the same curve as that of fully irradiated SNSPDs, while pulses of straight wires show a significantly faster decay due their smaller kinetic inductance. Thus, local irradiation shows no drawback with respect to the decay time compared to full irradiation of SNSPDs. At the same time, the pulse height of locally irradiated SNSPDs, shown in Figure 3.7, is higher than that of fully irradiated SNSPDs due to higher available bias currents after irradiating only locally. This is beneficial since higher detection voltage pulses are easier to process for the readout electronics.

3.6 Summary and outlook

Current crowding strongly limits the maximum bias current, sensitivity, and dark count rate of SNSPDs at low temperatures. Therefore, reducing the effect of current crowding is crucial for applications that require low dark count rates and high detection efficiency. We demonstrated a method to obtain current crowding–free SNSPDs by irradiating the straight segments of SNSPDs locally with He ions while leaving their bends unirradiated. Up to a He ion fluence of (90 ± 20) ions nm^{-2} the critical current is not reduced, meaning the photon sensitivity is enhanced without sacrificing any of the SNSPD's critical current. Above this threshold, the straight segments of the locally irradiated SNSPDs show a critical current lower than that of the bends such that current crowding in the bends does not limit the overall critical current anymore.

The boost in performance for locally irradiated SNSPDs is twofold: (1) the sensitivity of the SNSPD is enhanced due to He ion irradiation, and (2) the sensitivity is higher than for fully irradiated SNSPDs due to the higher available bias currents. Using this approach, we achieved a relative saturation plateau width of 37 % for a locally irradiated SNSPD compared to 10 % for a fully irradiated SNSPD, both irradiated with 800 ions nm^{-2}. This larger relative plateau width means that the SNSPD can be operated at lower relative bias currents with lower dark count rates and still detect single photons efficiently (e. g., 7 mHz dark count rate at an internal detection efficiency of 94 %). Therefore, this method is particularly beneficial for applications that require high detection efficiency combined with low dark count rate, such as quantum key distribution, brain imaging, and dark matter detection [3, 19, 161]. Furthermore, it is ideally suited for high fill factor or microscale SNSPDs that are prone to current crowding, especially if the detectors require He ion irradiation anyway to become single-photon sensitive [43]. Compared to methods that avoid current crowding by special meander designs [93–97] or by variable thickness SNSPDs [98, 99], this solution not only yields current-crowding free SNSPDs of arbitrary geometry and fill factor but also simultaneously enhances their sensitivity. By combining site-selective [111] with local He ion irradiation, one can realize highly and homogeneously performing SNSPD arrays. Moreover, local He ion irradiation can be further used to study the effect of current crowding in different regions of superconducting devices, including SNSPDs and the influence of current crowding in their bends onto properties such as dark count rate, detection efficiency, and switching current.

Having demonstrated how local irradiation of the straight nanowire segments enables current crowding–free SNSPDs, Chapter 4 delves into the underlying physical mechanisms responsible for these performance enhancements and introduces a complementary irradiation pattern that further expands our toolkit for detector optimization.

4 Origin of performance enhancement of SNSPDs via He ion irradiation

Following our investigations of site-selective and local He ion irradiation for enhancing SNSPDs in Chapters 2 and 3, this chapter explores the fundamental mechanisms behind these improvements. Comprehensive material characterization reveals that He ion irradiation transforms the crystalline Si substrate into an amorphous structure with He bubbles, while the NbTiN films surprisingly show similar crystallinity before and after irradiation. These modifications significantly reduce the thermal conductance between the superconducting thin film and the substrate from $210\,\mathrm{W\,m^{-2}\,K^{-4}}$ to $70\,\mathrm{W\,m^{-2}\,K^{-4}}$ after irradiation with $2000\,\mathrm{ions\,nm^{-2}}$. By leveraging the lateral ion straggle in the substrate, we demonstrate that selectively irradiating regions adjacent to a nanowire modifies the thermal conductance underneath the wire while minimizing direct interaction with the superconducting film. With this approach, we achieved a larger plateau width of saturating detection efficiency compared to full irradiation with the same fluence, while maintaining a similar photon-assisted critical current as that of an unirradiated reference device. These findings reveal that the reduction of the thermal conductance is a primary mechanism responsible for the irradiation-induced enhancement of SNSPD sensitivity and provide the mechanistic foundation that explains the success of the techniques developed in earlier chapters and opens new avenues for detector optimization via substrate engineering.

The research presented in this chapter has been published as Strohauer, S. et al. *Origin of Performance Enhancement of Superconducting Nanowire Single-Photon Detectors by He-ion Irradiation*. APL Quantum ***2,*** *026131 (2025), under a CC BY 4.0 license. The chapter largely follows this publication, with modifications to integrate it into the broader context of this thesis.*

Chapter 4

Contents

4.1 Introduction

As discussed in Chapters 2 and 3, He ion irradiation has emerged as a valuable post-processing technique to further advance photon detection efficiency, lower dark count rate, as well as improving timing jitter and the homogeneity of device performance in SNSPD arrays [43, 104, 111, 152, 163]. Previous studies have found that He ion irradiation alters properties of the underlying superconducting films. For example, it increases the sheet resistance and decreases the critical temperature of NbN, NbTiN, and MgB_2 superconducting thin films due to the formation of defects [43, 104, 111, 163]. Since the critical temperature is directly proportional to the superconducting energy gap, this results in an enhanced sensitivity of SNSPDs [104]. Moreover, Charaev *et al.* [43] note that for their MgB_2 based single-photon detectors, He ion irradiation not only introduces defects but also amorphizes the underlying SiC substrate, likely affecting the thermal conductance between the superconducting thin film and the substrate. This leads to a prolonged lifetime of the normal conducting domain, thereby increasing the detection probability. However, it has remained unclear whether such mechanisms, in addition to irradiation-induced defect formation, play a significant role in the improved performance after irradiation [43, 163]. In this chapter, we investigate how He ion irradiation modifies the morphology of both the NbTiN film and the SiO_2/Si substrate and discuss mechanisms by which these changes influence detector performance.

4.2 Irradiation-induced changes of film and substrate morphology

To explore how He ion irradiation influences superconducting film and substrate properties, we fabricated nominally 12 nm thick NbTiN films via DC reactive magnetron sputtering onto two Si substrates (5 mm × 5 mm) with a nominally 130 nm thick thermally grown SiO_2 layer. The superconductor thickness was controlled by measuring the sputtering rate and choosing the sputtering time correspondingly. On the sample that was later used for AFM and TEM measurements, we deposited a nominally 12 nm thick NbTiN layer. Subsequent TEM images revealed an actual thickness of (11.3 ± 0.5) nm. On the other sample we deposited a nominally 8 nm thick NbTiN layer for fabricating SNSPDs in the form of straight nanowires of 250 nm width and 25.8 µm length to study the influence of He ion irradiation onto the thermal conductance between the superconducting thin film and the substrate and an associated change in detection efficiency. On the nanowire sample, we patterned the NbTiN film with electron beam lithography and reactive ion etching, followed by contact pad fabrication using optical lithography and gold evaporation. The process for contact pad fabrication was also used to fabricate gold marker structures on the sample for AFM and TEM measurements. After characterization of the unirradiated devices, we used a He ion microscope (Zeiss Orion Nanofab) with an acceleration voltage of 30 kV for irradiation with He ions. On the nanowire sample, we fabricated three types of devices: (1) unirradiated nanowires, (2) fully irradiated nanowires, and (3) nanowires for which only the surrounding area was irradiated, leaving the nanowire and a 150 nm wide stripe next to the nanowire unirradiated. On the AFM/TEM sample, we used the He ion microscope to irradiate 4 µm × 4 µm and 15 µm × 15 µm squares of the NbTiN film. Subsequently, we measured those irradiated areas with an AFM (Bruker Dimension Icon) using the ScanAsyst mode and an OTESPA tip. Cross-sectional TEM lamellae were prepared from three regions: an unirradiated square and squares irradiated with 500 ions nm^{-2} and 2000 ions nm^{-2}. Using a focused ion beam microscope (FEI Helios G3 UC), we thinned these sections to approximately 10 nm to 35 nm in the vicinity of the NbTiN film. The lamellae were characterized using a probe-corrected transmission electron microscope (FEI Titan Themis) operated at 300 kV, employing (scanning) transmission electron microscopy ((S)TEM), high-angle annular dark-field imaging (HAADF), and energy-dispersive X-ray spectroscopy (EDX).

4.2.1 Microstructure: TEM, EDX, and ion distribution analysis

Figure 4.1 shows high-angle annular dark-field scanning transmission electron microscopy (HAADF-STEM) images of the stack NbTiN/SiO_2/Si in its unirradiated

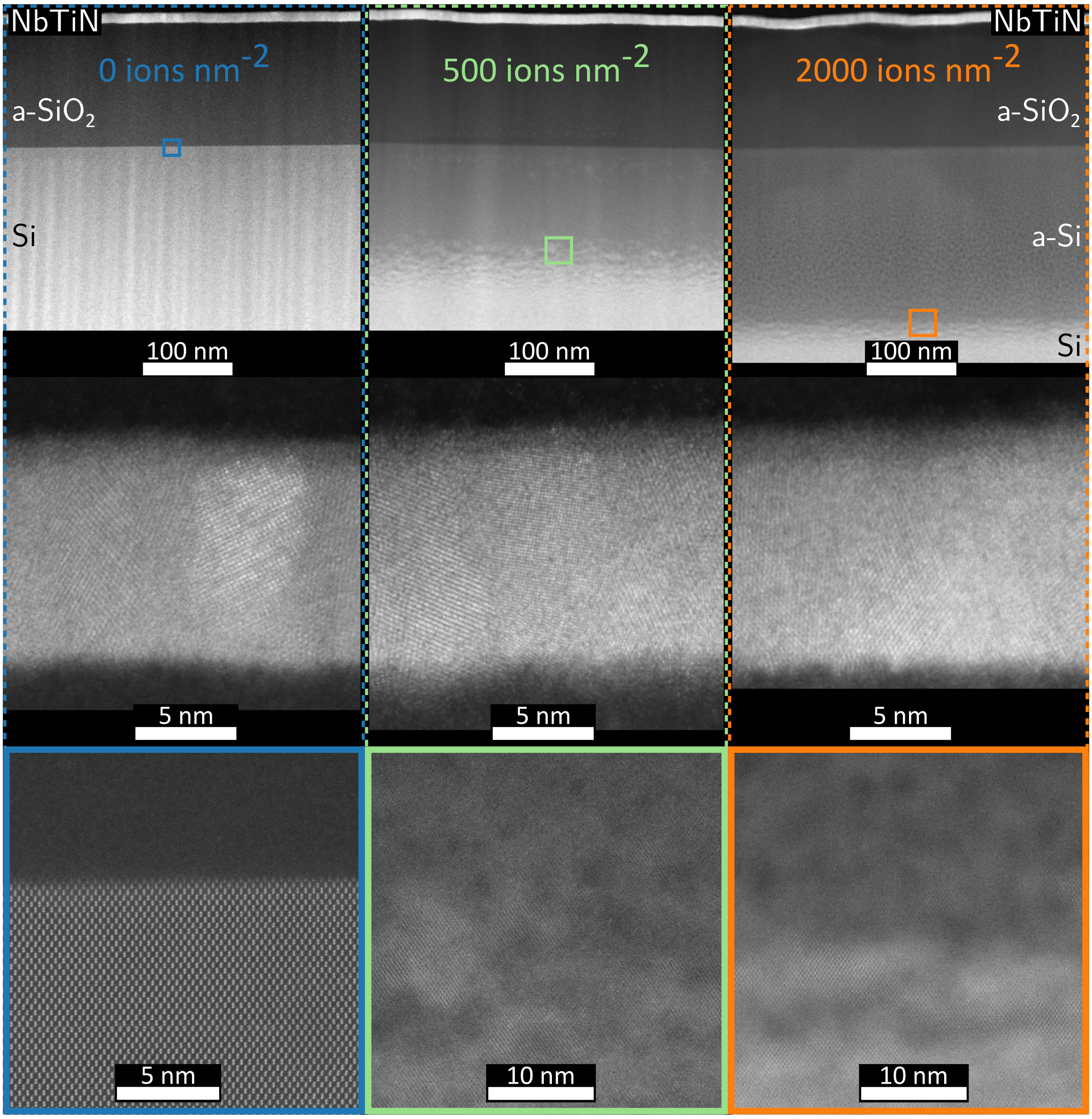

Figure 4.1: HAADF-STEM images of NbTiN/SiO_2/Si stacks before and after He ion irradiation: unirradiated (left column), irradiated with 500 ions nm^{-2} (middle column), and 2000 ions nm^{-2} (right column). Top row: Overview images showing the NbTiN film (light gray), the amorphous SiO_2 (dark gray), and the Si substrate. In the irradiated samples, the upper Si regions become amorphous (a-Si) with grayscale variations indicating porosity. The crystalline Si appears light gray. Middle row: High-resolution images of the NbTiN films reveal a similar thickness of 11.3 nm, 5 nm wide columnar δ-NbTiN domains, and a 1.5 nm thick amorphous oxygen-rich surface layer across all samples. Bottom row: Transition regions between amorphous and crystalline Si (locations marked by colored rectangles in the top row). The crystalline-amorphous interface coincides with the SiO_2/Si interface in the unirradiated sample, but lies 105 nm and 190 nm below the SiO_2/Si interface for the samples irradiated with 500 ions nm^{-2} and 2000 ions nm^{-2}, respectively. Dark contrasts in the amorphous Si regions are associated with pores. Adapted from [162], used under CC BY 4.0.

form, and after irradiation with 500 ions nm^{-2} and 2000 ions nm^{-2} (corresponding to 5×10^{16} ions cm^{-2} and 2×10^{17} ions cm^{-2}). Following He ion irradiation, we observe that the Si substrate becomes amorphous and contains He bubbles in a region extending from the SiO_2/Si interface at 150 nm depth to approximately 340 nm depth, consistent with previous studies [109, 110, 164–166].

This finding agrees with Monte Carlo simulations for the same NbTiN/SiO_2/Si stack, performed with the SRIM 2008 software [167]. Figure 4.2a–c shows the calculated lateral and depth resolved probability density function $f_{\mathrm{area}}(x, z)$ of stopping positions of the He ions originating from the focused beam of a He ion microscope, as well as the depth resolved FWHM of the lateral Gaussian distribution, and the probability density function $f_{\mathrm{line}}(z)$ of He ions stopping at a certain depth z. The lateral distribution was calculated by projecting the three-dimensional stopping positions of He ions onto a plane perpendicular to the surface. Most of the He ions penetrate deep into the substrate before they stop, with the maximum of the distribution of implanted He ions at a depth of 335 nm, which is in the range where we observe He bubble formation. At the same time, the He distribution is broadened laterally and in depth due to scattering and recoil events. Therefore, the simulated lateral Gaussian distribution has a FWHM of 266 nm when considering all He ion stopping positions, 241 nm for the layer where most He ions stop, and 400 nm within the NbTiN layer (although the fraction of ions that stop within each nm of this layer is more than an order of magnitude smaller than deep in the substrate).

As mentioned above, the HAADF-STEM images in Figure 4.1 reveal that He ion irradiation with 500 ions nm^{-2} (2000 ions nm^{-2}) transforms crystalline Si into an amorphous and porous structure with He bubbles. This extends to a depth of 105 nm (190 nm) below the SiO_2/Si interface, corresponding to a total depth of 255 nm (340 nm). Interestingly, the Si layer near the SiO_2/Si interface remains partially crystalline after irradiation with 500 ions nm^{-2}, while for the higher fluence of 2000 ions nm^{-2}, the amorphous region extends all the way to the SiO_2-Si interface. This partial preservation of crystallinity at moderate fluence is shown in Figure 4.3, which presents a high-resolution TEM image of the interfacial region between amorphous SiO_2 and Si after irradiation with 500 ions nm^{-2}. The interface, marked by a dashed white line, separates the uniformly amorphous SiO_2 from a transition region in the Si substrate. In this region, the crystalline and amorphous phases of Si coexist, and we observe a mixture of amorphous areas (light gray) and crystalline domains (darker areas). The high-resolution inset in Figure 4.3 reveals clear lattice fringes in the preserved crystalline domains, providing direct evidence of residual crystalline order in these regions. This partial preservation of crystallinity stands in contrast to the complete amorphization observed at 2000 ions nm^{-2}, indicating that the transformation process depends strongly on the He ion fluence. At the same time, the thickness of the SiO_2

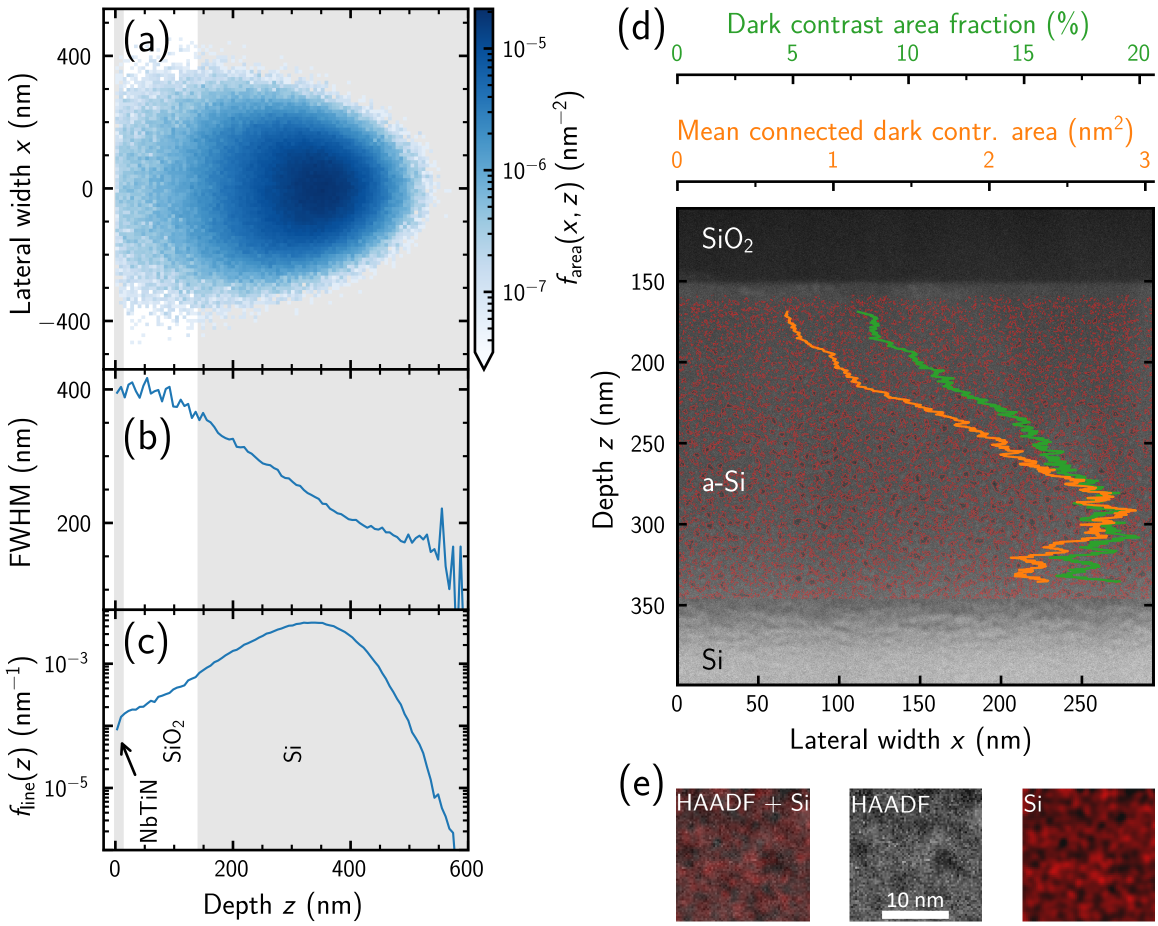

Figure 4.2: Simulated distribution of He ion stopping positions (a-c) and experimental analysis of structural modifications (d-e) in the irradiated NbTiN/SiO_2/Si stack. (a) Lateral and depth resolved probability density function $f_{\text{area}}(x, z)$ of the stopping positions. (b) Depth resolved FWHM of the lateral Gaussian distribution. (c) Probability density function $f_{\text{line}}(z)$ for He ions stopping at a certain depth z. (d) HAADF-STEM image of the sample irradiated with 2000 ions nm^{-2}, with dark contrast regions highlighted by red outlines. Overlaid curves show the dark contrast area fraction (green) and average size of connected dark contrast regions (orange) versus depth z. (e) High-magnification comparison of HAADF contrast with Si content: overlay of HAADF and Si EDX signal (left), HAADF image (center), and Si EDX map (right), demonstrating the correlation between dark HAADF contrast and reduced Si content. Adapted from [162], used under CC BY 4.0.

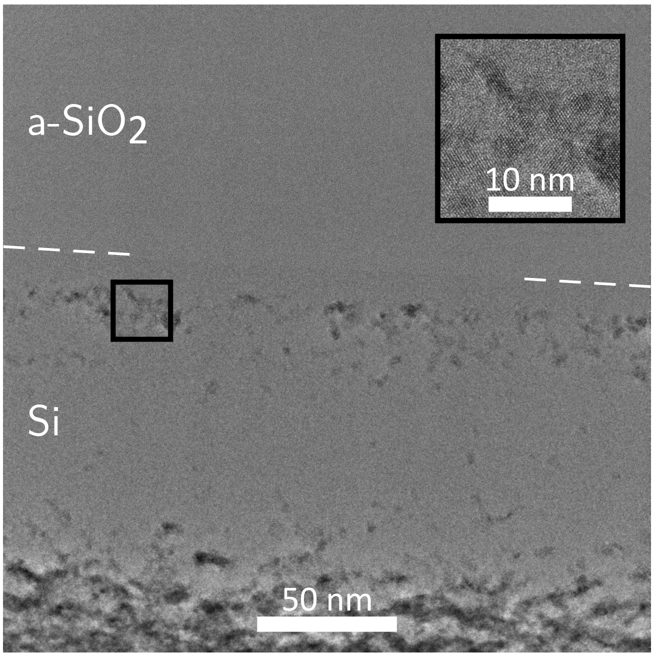

Figure 4.3: TEM image of the interfacial region between amorphous SiO_2 and Si in the NbTiN/SiO_2/Si stack after irradiation with 500 ions nm^{-2}. The interface is marked by a dashed white line. Light gray regions indicate amorphous material and darker areas reveal crystalline silicon. The inset (3× magnification) shows a partially crystalline region where lattice fringes are clearly visible, demonstrating the local crystalline order. Adapted from [162], used under CC BY 4.0.

layer remains unchanged at (137 ± 3) nm after irradiation. As shown in Figure 4.2e, complementary HAADF-STEM imaging and energy-dispersive X-ray spectroscopy (EDX) of the amorphous Si region reveal that areas of dark contrast correspond to reduced Si content. These dark contrasts, originating from local minima in the projected Si thickness, are associated with He bubble formation during irradiation. This interpretation is supported by the irradiation-induced surface elevation of the stack measured by AFM, as discussed later in this section. To quantify these observations, we analyzed the spatial distribution of dark contrast in the amorphous Si region in Figure 4.2d. At each depth, we calculated the dark contrast area fraction by identifying regions below a threshold value after local background subtraction. This analysis shows that both the area fraction and average size of dark contrast regions reach their maxima at approximately 300 nm depth, closely matching the simulated peak of He ion stopping positions at 335 nm shown in Figure 4.2c. We observe these dark contrast regions in a range extending from approximately the SiO_2/Si interface (located at 150 nm depth) to about 340 nm depth. While the projective nature of TEM imaging prevents direct interpretation of individual feature sizes, this spatial correlation between dark contrast regions and simulated ion stopping positions, combined with the observed surface elevation in AFM measurements, indicates the formation of He bubbles in the Si substrate, consistent with previous studies [109, 110, 164–166].

Moreover, the NbTiN film exhibits increased wrinkling at higher He ion fluences, while it maintains its original thickness of (11.3 ± 0.5) nm and shows no visible cracks or noticeable material loss from sputtering. We use the term "wrinkling" rather than "surface roughness" because the film undergoes a characteristic deformation where both its top and bottom surfaces exhibit synchronized undulations while maintaining constant thickness. Notably, despite the wrinkling of the NbTiN layer, the SiO_2/Si interface remains flat. Furthermore, at all fluences the NbTiN film retains its columnar crystalline domains (NaCl-type face centered cubic δ-phase of NbTiN) with an oxygen-rich top layer [168–170]. We do not see any substantial change in crystallinity or visible defects between the differently irradiated NbTiN films. This is surprising, since we expected the polycrystalline structure of the pristine NbTiN film to become more amorphous and exhibit an increasing number of defects with increasing He ion fluence. To further analyze the increased wrinkling of the irradiated NbTiN films and to correlate it to subsequent AFM measurements, Figure 4.4a shows the local deviation from the mean surface height of the NbTiN layer as determined from the TEM images. The analysis reveals that the local surface height varies within intervals of 1.8 nm, 2.5 nm and 8 nm around the mean surface height for the film before He ion irradiation and after exposure to 500 ions nm^{-2} and 2000 ions nm^{-2}, respectively. To complement these structural observations, we performed energy-dispersive X-ray spectroscopy (EDX) to confirm the elemental composition of the different layers and interfaces. Figure 4.5 shows the compositional profiles extracted from STEM-EDX maps, taken perpendicular to the interfaces with integration performed parallel to them. A high-resolution scan across the NbTiN film reveals the elemental distribution within the 12 nm thick film, confirming the presence of Nb, Ti, and N throughout the film with an oxygen-rich surface layer at the air interface. The profile also shows the SiO_2 support adjacent to the film and a protective carbon layer that was required for TEM sample preparation. A wide-area scan across the complete NbTiN/SiO_2/Si stack confirms the expected elemental distribution across all layers, including the SiO_2 and the Si substrate.

4.2.2 Surface morphology characterization via AFM

While TEM analysis provides valuable insights into the internal microstructure and subsurface modifications, complementary surface characterization offers important additional perspectives on how He ion irradiation affects the overall stack. To examine these surface-level changes and correlate them with the subsurface modifications observed in TEM, we investigated the irradiated surfaces using an AFM (Bruker Dimension Icon), providing quantitative information about surface morphology changes across different fluences and materials. Figure 4.6a shows the surface of an irradiated

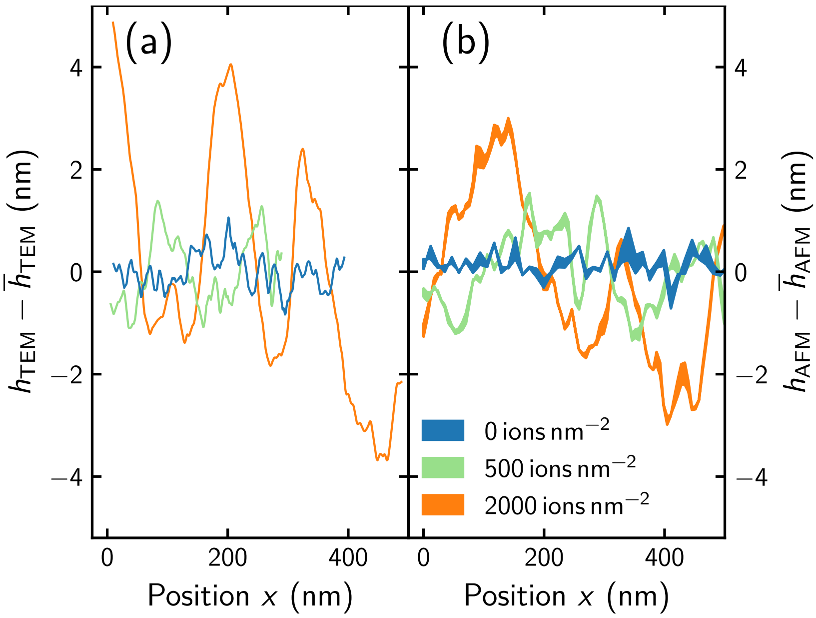

Figure 4.4: Local deviation from the surface height average, $h - \bar{h}$, as determined by (a) TEM and (b) AFM measurements of the unirradiated NbTiN film and after irradiation with 500 ions nm^{-2} and 2000 ions nm^{-2}. The local width of the lines in (b) is defined by the local height range bounded by the AFM line profiles obtained from the two averaging widths (12 nm and 35 nm). Adapted from [162], used under CC BY 4.0.

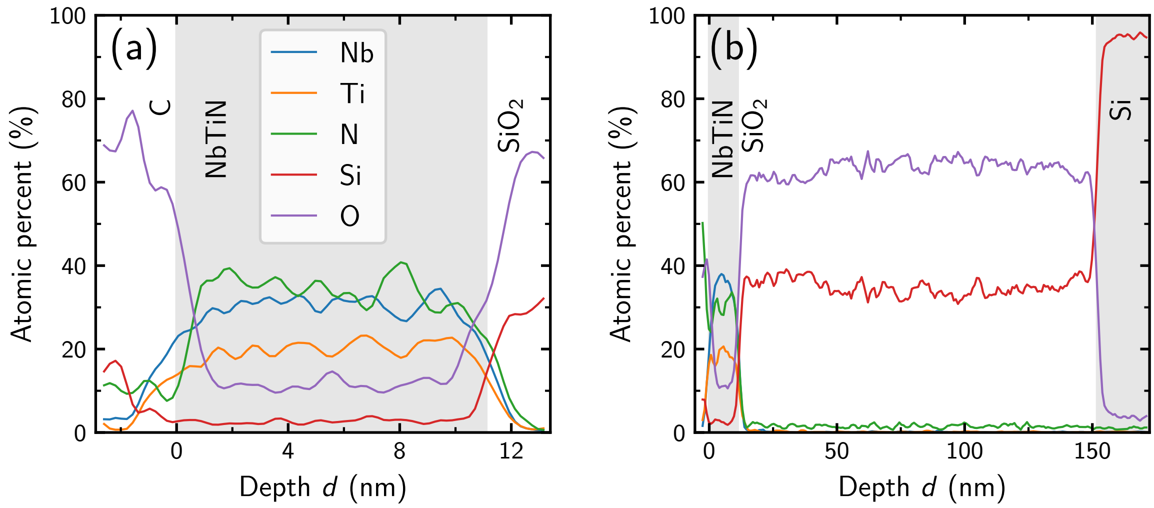

Figure 4.5: Energy dispersive X-ray spectroscopy (EDX) line profiles extracted from STEM-EDX maps of the unirradiated NbTiN/SiO_2/Si stack. The profiles were taken perpendicular to the interfaces, with integration performed parallel to them. (a) High-resolution scan across the NbTiN film (20 nm integration width), showing the SiO_2 support (right), the NbTiN film with its oxygen-rich surface layer (center), and a protective carbon layer required for sample preparation (left). Carbon was excluded from the elemental quantification to prevent distortion from its residual presence throughout the sample. (b) Wide-area scan across the complete NbTiN/SiO_2/Si stack (58 nm integration width). Adapted from [162], used under CC BY 4.0.

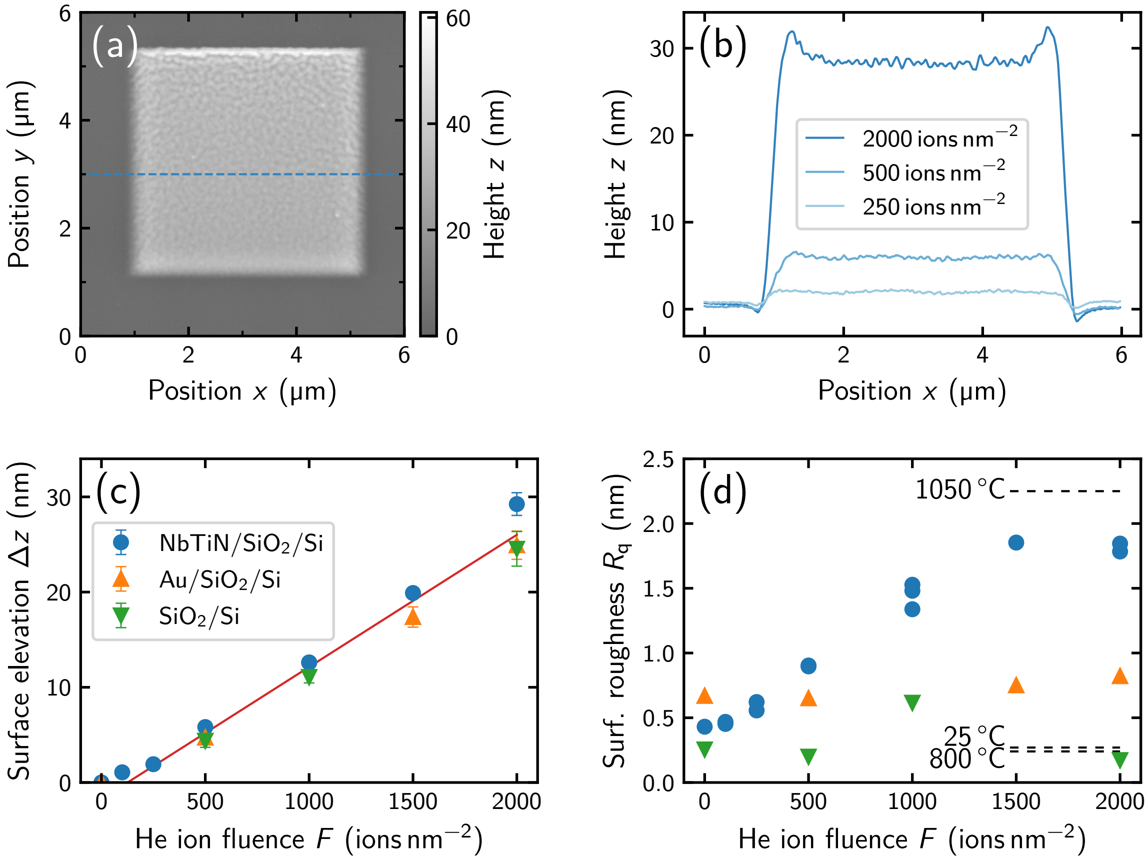

Figure 4.6: AFM characterization of irradiated NbTiN films. (a) A representative square structure obtained after irradiation with 2000 ions nm^{-2}. (b) Line profiles for three different He ion fluences. For 2000 ions nm^{-2}, the profile is also indicated as a blue dashed line in (a). (c) The fluence dependent surface elevation of the quasi-flat center of the irradiated area. Besides the stack NbTiN/SiO_2/Si, it was also measured for the reference stacks Au/SiO_2/Si and SiO_2/Si. The red line is a linear fit of all data with a fluence of 250 ions nm^{-2} or above. (d) Dependence of the RMS surface roughness on the He ion fluence for the same stacks as in (c). The dashed lines show the measured roughness before and after annealing a second NbTiN/SiO_2/Si sample at temperatures of 800 °C and 1050 °C (see Section 4.2.3 for details). Adapted from [162], used under CC BY 4.0.

4 µm × 4 µm NbTiN square. Upon irradiation with 2000 ions nm^{-2}, we observe a surface elevation of 28 nm and an increased surface roughness within the irradiated area. The elevation predominantly stems from He bubble formation in the silicon, as the density difference between amorphous and crystalline silicon is only 1.8 % [171]. During irradiation, the scan direction causes uneven redeposition of sputtered NbTiN, with more material accumulating at the starting edge (upper edge). This results in an increased height of that edge compared to the others [172, 173]. To quantify the dependence of the surface elevation and the surface roughness on the He ion fluence, we performed AFM measurements for multiple fluences and not only for the NbTiN/SiO_2/Si stack but also for two reference stacks, Au/SiO_2/Si and SiO_2/Si. Figure 4.6b shows the height profiles of three differently irradiated NbTiN/SiO_2/Si stacks, where each point represents the average height across a 1.5 µm wide strip perpendicular to the profile direction. As shown in Figure 4.6c, the surface elevation increases linearly with the He ion fluence for both Au and NbTiN thin films, as well as for the bare SiO_2/Si substrate. This behavior is consistent with expectations, since most He ions interact only weakly with the film and stop deep inside the substrate where they form He bubbles that cause the surface to rise. The linear fit (excluding fluences below 250 ions nm^{-2}) has a non-zero intercept at 120 ions nm^{-2}, from which we conclude that significant bubble formation and surface elevation begin just above a certain fluence, similar to an observation in [174]. To study the dependence of the root-mean-square (RMS) roughness of irradiated NbTiN films on the He ion fluence, we irradiated squares with dimensions of 4 µm × 4 µm and 15 µm × 15 µm with beam currents ranging from 10.6 pA to 119 pA, which were chosen to obtain irradiation times between 1 min and 10 min even for the highest fluences. As shown in Figure 4.6d, the surface roughness of the NbTiN film increases from 0.43 nm for the unirradiated film to 1.85 nm at 1500 ions nm^{-2}. On the contrary, the bare SiO_2/Si substrate and the sample with a 10 nm gold layer do not show a systematic increase in roughness after irradiation (0.31 nm and 0.72 nm average roughness, respectively). Moreover, while the different squares of 4 µm × 4 µm and 15 µm × 15 µm exhibit similar roughness in the homogeneously irradiated center regions, we observed a slightly higher surface roughness when using higher beam currents: Figure 4.7 shows the RMS surface roughness of the stack NbTiN/SiO_2/Si measured with an AFM after irradiation with beam currents ranging from 0.5 pA to 118 pA. The roughness increases from 0.43 nm before irradiation to 1.19 nm and 1.78 nm for the lowest and highest beam current, respectively. This difference we explain by an increased viscous flow of the SiO_2 at higher beam currents, allowing more relaxation of the stress that built up in the NbTiN during the sputtering process. However, even for the smallest beam currents, the roughness increased by a factor of three after irradiation with 2000 ions nm^{-2} compared to the unirradiated film.

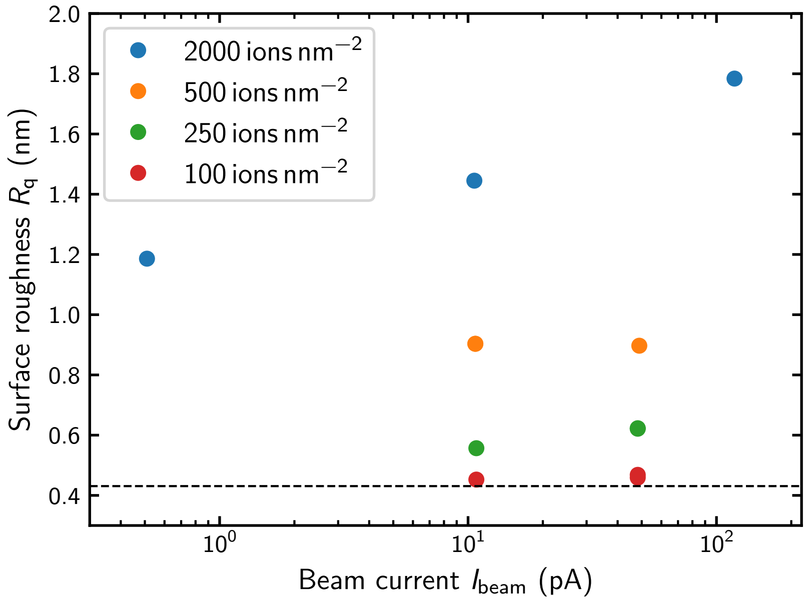

Figure 4.7: RMS surface roughness versus beam current that was used for irradiation with He ion fluences ranging from 100 ions nm^{-2} to 2000 ions nm^{-2}. The black dashed line indicates the RMS surface roughness before irradiation. Adapted from [162], used under CC BY 4.0.

To compare the surface roughness measured with the AFM with the wrinkling determined from the TEM images, Figure 4.4b shows line profiles from three AFM images for the same He ion fluences as those in the TEM profiles of Figure 4.4a. Each height value along the AFM profiles is the local average across a strip oriented perpendicular to the profile direction, using widths of 12 nm and 35 nm to match the thickness range of the TEM lamellae. The local width of the lines in Figure 4.4b is defined by the local height range, bounded by the profiles obtained from the two averaging widths, and indicates that both yield similar results. The AFM line profiles exhibit surface height variations within intervals of 1.6 nm, 3 nm and 6 nm around the mean surface height for the unirradiated film and after exposure to 500 ions nm^{-2} and 2000 ions nm^{-2}, respectively. These values, as well as their characteristic length scales of variation, closely match those derived from the TEM image analysis in Figure 4.4a, demonstrating quantitative agreement between both measurement techniques. Based on these results, we conclude that the AFM line profiles and RMS roughness not only show continuously increasing surface height variations with increasing He ion fluence, but can also be used to estimate the wrinkling of the NbTiN film observed in TEM images. To conclude, the increase of the AFM-measured surface roughness with increasing He ion fluence, combined with the correlation between surface roughness and wrinkling, indicate that the NbTiN film undergoes wrinkling rather than developing surface roughness with increasing He ion fluence.

4.2.3 Mechanisms of film wrinkling and stress relaxation

Measurements in the literature have shown that ion irradiation enables plastic flow in SiO_2 and Si [166, 175–178], and that sputtered NbTiN typically exhibits internal stress [179–183]. This agrees with our observation of an increasing wrinkling of the NbTiN film with increasing He ion fluence: When irradiating the NbTiN/SiO_2/Si stack, the stress in the NbTiN film can relax and deform the originally flat NbTiN film due to radiation-induced plastic flow of the underlying SiO_2. To test this hypothesis, we took a NbTiN film on a SiO_2/Si substrate of the same sputtering run and heated it to temperatures up to 1050 °C. Since viscous flow of thermally grown SiO_2 starts at 960 °C [184], we expected an increase of the NbTiN film wrinkling just above that temperature. We mounted the sample in a chamber that was purged with nitrogen and evacuated to a pressure range of 10^{-7} mbar to 10^{-8} mbar before ramping up the temperature and holding the target temperature for 30 min. Figure 4.8 shows the AFM images and line profiles across the surface before and after heating to 800 °C and 1050 °C. We note that the sample used in this heating experiment initially had many large grains (potentially from a non-clean surface before sputtering) that grew in size when heating to 1050 °C. Therefore, we placed the line profiles in regions without those grains. While the line profiles before and after heating the sample to 800 °C show a similar RMS roughness of 0.27 nm and 0.24 nm, it increases to 2.25 nm after heating to 1050 °C. This indicates that stress in the NbTiN film is already present after sputtering and that it relaxes when enabling viscous flow of the underlying substrate. To verify that the deformation does not originate from strain in the substrate material, we also obtained reference data by irradiating the unprocessed wafer (SiO_2/Si stack) and the wafer with an evaporated gold layer on top. Both do not show an increase of wrinkling/roughness with increasing He ion fluence, as can be seen in Figure 4.6d.

In summary, we observe an increased wrinkling of the NbTiN film as the He ion fluence increases, while its thickness and roughness remain unchanged. This wrinkling originates from relaxation of stress that builds up in the NbTiN film already during the sputtering process. When the NbTiN/SiO_2/Si stack is irradiated with He ions or heated to temperatures above 960 °C, viscous flow of the SiO_2 allows stress in the NbTiN layer to be released, causing the NbTiN to wrinkle. These structural modifications—particularly the substrate amorphization, He bubble formation, and changes at the film-substrate interface—are likely to significantly alter the thermal pathways between the superconducting film and the substrate. The impact of these changes on the thermal conductance, a critical parameter for SNSPD performance, is investigated in the following section.

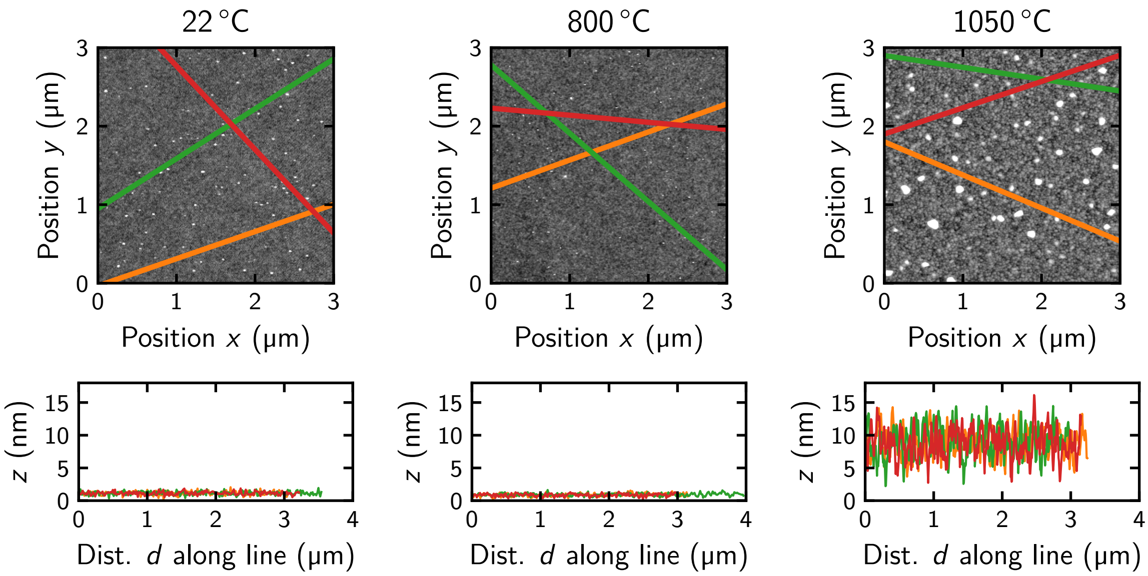

Figure 4.8: AFM measurements and corresponding line profiles of the stack NbTiN/SiO_2/Si after exposing it to three different temperatures. The as-sputtered film and the film after heating it to 800 °C exhibit a similar RMS roughness of 0.27 nm and 0.24 nm, respectively. This increases to 2.25 nm after heating the sample to 1050 °C. Adapted from [162], used under CC BY 4.0.

4.3 He ion irradiation impact on thermal conductance

We continue to link the He-ion induced changes in the superconducting thin film and the substrate to their thermal coupling, before showing in the subsequent section that this contributes substantially to the irradiation-induced performance enhancement of SNSPDs. The detection efficiency in SNSPDs is influenced not only by thin film properties such as critical temperature, sheet resistance, and diffusivity, but also by thermal properties of the thin film and the superconductor-substrate interface. This is highlighted by the improved detection efficiency that Xu *et al.* achieved after reducing the thermal conductance between the superconducting thin film and the substrate by underetching the SNSPD [185]. Simulations in this work showed that samples with lower thermal conductance exhibit a longer hotspot decay time, meaning that the heat loss from the hotspot to the substrate is suppressed, thereby increasing the fraction of the photon energy that contributes to hotspot formation. We expect that the effects of He ion irradiation, such as the formation of He bubbles and the modification of the crystallinity of the Si substrate, may similarly reduce the thermal conductance and play an important role in the observed increase in detection efficiency of SNSPDs following irradiation. Therefore, we continue by investigating the impact of He ion irradiation on the thermal conductance between the superconducting thin film and the substrate in the following.

The equation governing heat flow in a one-dimensional nanowire is

$$J^2\rho + \kappa\frac{\partial^2 T}{\partial x^2} - \frac{\sigma}{d}(T^4 - T_{\text{sub}}^4) = C\frac{\partial T}{\partial t}, \tag{4.1}$$

accounting for the heat flow along the nanowire, Joule heating from the resistive barrier when the nanowire is in the normal conducting state, and heat escaping from the superconducting thin film of thickness d to the substrate at a fixed substrate temperature T_{sub} [185–188]. Here, J is the current density, ρ is the normal-state resistivity, κ is the thermal conductivity of the superconducting nanowire, σ is the thermal conductance between the superconducting thin film and the substrate, and C is the specific heat per unit volume of NbTiN. According to the literature [189, 190], the thermal conductance σ can be obtained from the equation for the retrapping current density,

$$J_{\text{r}} = \sqrt{\frac{\sigma}{4d\rho}\left(T_{\text{c}}^4 - T_{\text{sub}}^4\right)}\,, \tag{4.2}$$

with the critical temperature T_{c}. To measure the retrapping current I_{r}, we pass a current above the switching current I_{sw} through the nanowire and then gradually reduce it until the normal conducting resistive domain within the nanowire can no longer sustain itself by Joule heating. This current, at which it switches back to the superconducting state, defines the retrapping current. We measured I_{r} for 25.8 µm long, 250 nm wide, and 8 nm thick nanowires at a temperature of 1 K, irradiated with He ion fluences ranging from 0 ions nm^{-2} to 2000 ions nm^{-2}. As shown in Figure 4.9a, the largest decrease of I_{r} occurs at fluences smaller than 250 ions nm^{-2}, and it reduced from 6.7 µA to 1.2 µA comparing the unirradiated device to the device after irradiation with 2000 ions nm^{-2}. Moreover, in the inset of Figure 4.9a we present the measured switching current of the same devices and observed the expected decrease with increasing He ion fluence that has already been reported in Chapter 2 and in the literature [104, 111]. In addition to the retrapping and the switching current, we measured the critical temperature and the sheet resistance of the irradiated films using the van der Pauw method as described in previous work [111, 123, 124]. As shown in Figure 4.9b and c, the critical temperature decreases, while the sheet resistance increases with increasing He ion fluence. We fitted the sheet resistance using the model introduced in Chapter 2 that accounts for defect formation in the NbTiN film, and relate the critical temperature to the ion fluence via the sheet resistance by using the universal scaling law of Ivry *et al.* [145]. While the sheet resistance fit closely matches the measured data, the critical temperature fit differs slightly from measurements at low and high He ion fluences. With these ingredients and the substrate temperature $T_{\text{sub}} = 1$ K, we calculate the thermal conductance σ via Equation (4.2). As shown in Figure 4.9d, it decreased from initially 210 W/m^{2}K^4 to 70 W/m^{2}K^4 after irradiation with 2000 ions nm^{-2}. Moreover,

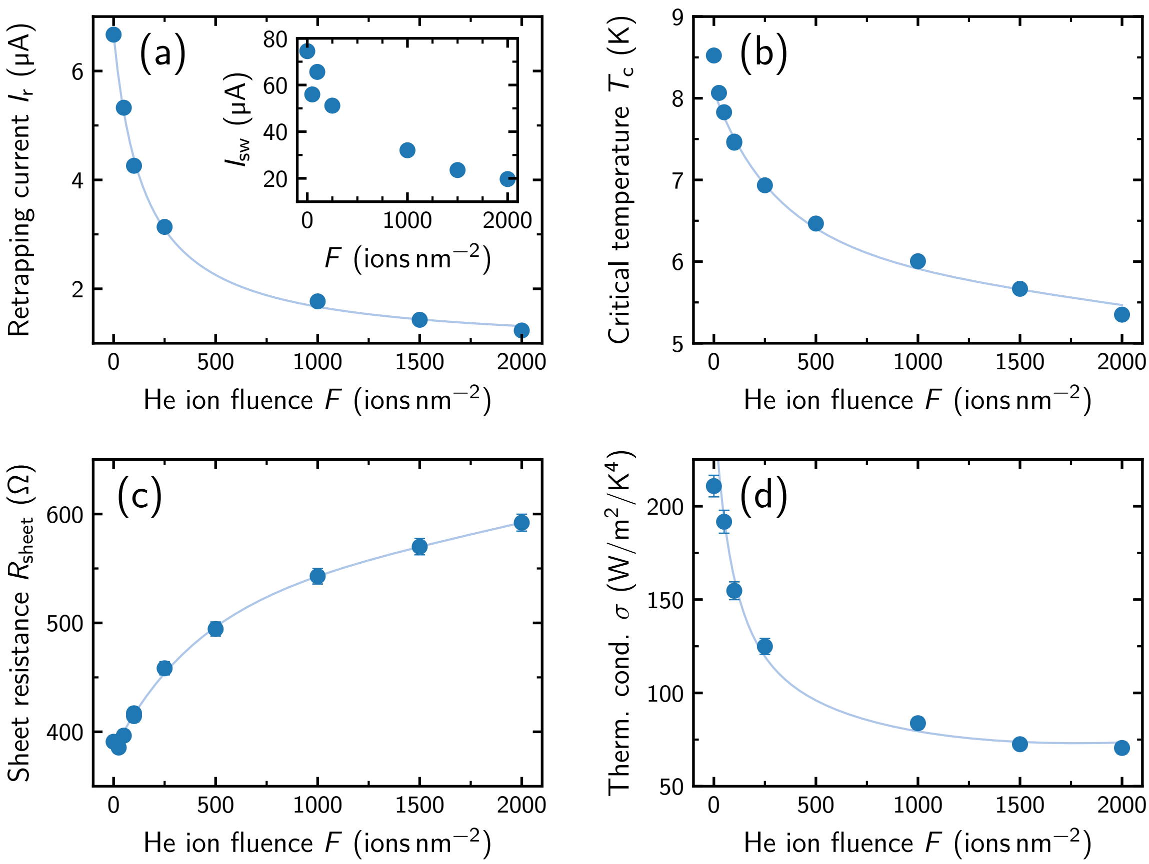

Figure 4.9: Modification of basic transport properties and of the thermal conductance from the SNSPD to the substrate by He ion irradiation. (a) The retrapping current I_r with the switching current I_{sw} as inset, both measured at a temperature of 1 K. (b) The critical temperature T_c. (c) The sheet resistance R_{sheet}. (d) The thermal conductance between the superconducting thin film and the substrate σ. While the curves for I_r and σ are solely guides to the eye, the curves for T_c and R_{sheet} were fitted with the models described in the main text. Error bars are in some cases smaller than the symbols. Adapted from [162], used under CC BY 4.0.

the data suggests a saturating thermal conductance for fluences above 1500 ions nm^{-2}. This can be explained by considering two paths contributing to the total thermal conductance: (1) a path where heat escapes normal to the wafer surface through the irradiated area, σ_{norm}, and (2) a path where heat flows in-plane, parallel to the wafer surface, $\sigma_{\text{in-plane}}$. Since the He bubbles form deep within the substrate and the He ions deposit most of their energy there, we expect that He ion irradiation primarily reduces σ_{norm} deep inside the substrate and underneath the irradiated area. At the same time, we expect $\sigma_{\text{in-plane}}$ in the NbTiN film and in the first nanometers underneath the film to be less affected by the irradiation. Above a sufficiently high He ion fluence, the in-plane thermal conductance starts to dominate and the total thermal conductance saturates at a value determined by the lateral dimensions of the irradiated area and the thickness of the thermally conducting channel. The thermal conductance values obtained in this work lie slightly below the range reported in literature for NbN (229 W/m^{2}K^4 to 711 W/m^{2}K^4) [185, 188, 189], which could be attributed to the different material properties of NbTiN versus NbN.

In summary, the thermal conductance between the superconducting thin film and the substrate decreases continuously with increasing He ion fluence, and after irradiation with 2000 ions nm^{-2} it saturates at only 33 % of the value for the unirradiated device. The reduced thermal conductance can have multiple origins such as (1) the He bubbles that form deep inside the substrate and act as a thermally insulating layer, (2) the irradiation-induced amorphization of the originally crystalline Si [191, 192], and (3) a modified superconductor-substrate interface due to the relaxation of internal stress in the NbTiN.

4.4 Enhancing detection efficiency via thermal conductance engineering

In the previous sections we elaborated that the most prominent irradiation-induced changes of the NbTiN film and the underlying SiO_2/Si substrate are the wrinkling of the NbTiN film, the amorphization of the first few hundred nanometers of Si, and the formation of He bubbles in a region extending from approximately the SiO_2/Si interface (located at 150 nm depth) to about 340 nm depth. Besides the fact that point defects are not visible in our TEM images of the NbTiN films, we also did not observe any changes of crystallinity or amorphization of the NbTiN film with increasing He ion fluence. Therefore, we conclude that in addition to the direct impact of irradiating the NbTiN film, a significant contribution to the enhanced sensitivity of SNSPDs following He ion irradiation [104, 111, 152] arises from a change in the thermal conductance between the superconducting thin film and the substrate. This we investigate in detail in the following sections.

4.4.1 Experimental design for local thermal conductance modification

To verify that changes in detector performance after irradiation cannot solely be explained by the direct irradiation effects of the NbTiN film, we compare three different irradiation schemes: (1) an unirradiated reference device, (2) a device fully irradiated with 2000 ions nm^{-2}, and (3) a device where we irradiated only the surrounding regions up to a distance of 150 nm to the superconducting wire with 2000 ions nm^{-2}. The focused He ion beam enters the substrate, where through scattering and recoil events, the He ions successively transfer their energy to the substrate while spreading laterally as they move through it. Due to this lateral straggle, we expect the He ions to amorphize the Si and create He bubbles deep inside the substrate not only in the directly irradiated regions, but also underneath the nanowire for the device where we irradiated only the regions next to the superconducting wire. This will modify the thermal conductance to the substrate, while keeping the direct effects of He ions on the NbTiN wire limited. We conclude that if a direct modification of the NbTiN wire by the He ion beam was the one and only cause for a change of detector properties, an irradiation of the surrounding area should have a very limited influence on them.

Before experimentally investigating this irradiation scheme, we firstly present simulations of the He ion distribution and energy deposition, accompanied by a critical analysis of the limitations of this specific irradiation strategy.

4.4.2 He ion and energy distribution for distant irradiation

To quantitatively assess the irradiation strategy introduced above, we estimate the relative amount of implanted He ions and deposited energy in and underneath a 250 nm wide NbTiN wire when selectively irradiating only the surrounding area (up to 150 nm from the wire edge) compared to full-wire irradiation. The average lateral spread of He ions when irradiating a single spot can be calculated by projecting the simulated three-dimensional stopping positions of He ions onto a line parallel to the surface, and results in a Gaussian distribution with a FWHM of 266 nm. When irradiating only the regions next to the superconducting wire, this lateral spread will result in a significant fraction of He ions underneath the nanowire. The relative fraction of implanted He ions f_{rel} along a line perpendicular to the nanowire can be calculated by taking the convolution of the Gaussian distribution of He ions with the one-dimensional profile of irradiation along this line,

$$f_{\text{rel}}(x) = \int_{-\infty}^{\infty} \frac{1}{\sqrt{2\pi\sigma^2}} e^{-\frac{(s-x)^2}{2\sigma^2}} \cdot \Theta\left(|s| - \frac{w_{\text{unirr}}}{2}\right) \mathrm{d}s \;, \tag{4.3}$$

with the standard deviation σ of the Gaussian distribution, the width w_{unirr} of the unirradiated area, and the Heaviside step function Θ. The resulting He ion distribution is shown as orange line in Figure 4.10a, with the minimum and maximum amount of He ions underneath the nanowire being 1.5 % and 9.3 %, and an average amount of 3.9 % of that in the fully irradiated area.

As shown in Figure 4.2b, the FWHM of the He ion stopping positions within the NbTiN layer is 400 nm due to recoil events and scattering. Following the same procedure as above but projecting only the stopping positions of He ions that end up in the 12 nm thick NbTiN film onto a line perpendicular to the nanowire, we calculate the convolution of the resulting Gaussian distribution with the one-dimensional irradiation profile and obtain the relative fraction of He ions implanted in the nanowire as presented as green line in Figure 4.10a. Since the FWHM of the implanted He distribution in the NbTiN layer is higher than that when considering the stopping positions of all He ions, also the minimum and maximum relative fractions, 10.9 % and 20.1 %, and the average fraction of 14.0 % are higher. This also means that the number of He ions that stop within the NbTiN wire is in the same order of magnitude when comparing full irradiation with irradiation up to a distance of 150 nm to the wire. This leads to the question of how the effects of direct irradiation differ from irradiation up to a distance of 150 nm to the wire, since according to the Bragg peak the He ions deposit most energy per nm shortly before they stop, as can be seen in Figure 4.10b. However, the energy loss per nm when entering the sample is still half of that at the maximum in 270 nm sample depth. Moreover, at the spots where the focused He ion beam hits the sample, all He ions deposit a fraction of their kinetic energy in the NbTiN film. Taking into account that only the fraction 10^{-4} of all ions end up in each nm of the NbTiN film, we conclude that the total energy deposited in the NbTiN wire when irradiating up to a distance of 150 nm to the wire, is approximately four orders of magnitude smaller than when irradiating the whole device. We note, however, that the small fraction 10^{-4} of the He ions that are implanted in the NbTiN wire per nm is similar when comparing fully irradiated devices with those irradiated up to a distance of 150 nm to the wire. At the same time, the total amount of He ions implanted in the SiO_2/Si substrate underneath the nanowire is still 3.9 % of that in the fully irradiated area, leading to substantial He bubble formation and a reduced superconductor-to-substrate thermal conductance underneath the nanowire.

Thus, when keeping the wire unirradiated and irradiating only its surroundings up to a distance of 150 nm to the wire, the NbTiN should be barely directly affected by the He ion beam (only by the small fraction of deflected or recoiled atoms/ions), while the reduced thermal conductance due to the amorphization of Si and the formation of He bubbles in the substrate extends under the nanowire.

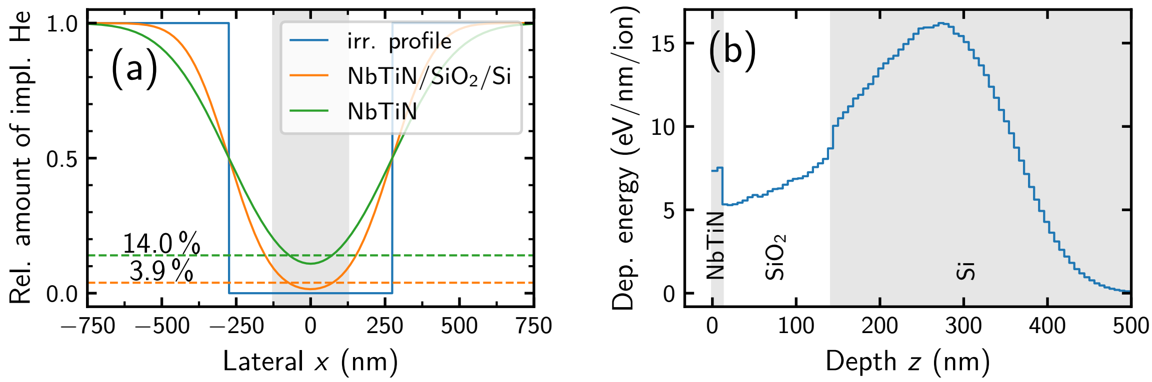

Figure 4.10: Simulated He ion and energy distribution after irradiation of the sample stack NbTiN/SiO_2/Si in the surrounding area of the wire up to a distance of 150 nm from the wire. (a) Normalized implanted He ion distribution. The irradiation profile is shown as a blue line (1 in the regions where the He ion beam hits the surface), while the width of the nanowire is indicated by the gray shaded area. The orange line is the distribution of He ions integrated along the full depth of the sample (over the whole stack NbTiN/SiO_2/Si), while the green line is the distribution when integrating only over the NbTiN layer. Both distributions are normalized to the amount of implanted He for full irradiation. The corresponding average amount of implanted He underneath the wire is indicated by the horizontal dashed lines. (b) Deposited energy per ion and per nm sample depth. The material stack NbTiN/SiO_2/Si is indicated by the differently shaded areas. Adapted from [162], used under CC BY 4.0.

We note that beside the amorphization of Si and the formation of He bubbles underneath the wire, we cannot completely exclude that the following two points also have some influence on the device performance: (1) The curved surface due to the different surface elevation in the center versus the edges of the nanowire, which is originating from smaller He bubbles underneath the center of the wire compared to underneath the wire edges. (2) A potential residual plastic flow of the SiO_2 near the NbTiN interface due to the small amount of energy deposited in this region from scattered/recoiled He ions. However, since the fraction of energy is only on the order of 10^{-4} compared to the fully irradiated regions, we expect this effect to be negligible. To fully isolate the change in device properties due to the modified superconductor-to-substrate thermal conductance after irradiation, future studies comparing the performance of devices fabricated on pre-irradiated substrate regions to similar devices fabricated on unirradiated regions of the same substrate would be useful.

In summary, by keeping the wire unirradiated while selectively irradiating only the surrounding regions, we minimize direct modification of the NbTiN film while substantially reducing the thermal conductance through substrate modification that extends beneath the wire. We now proceed to the experimental characterization of this irradiation strategy.

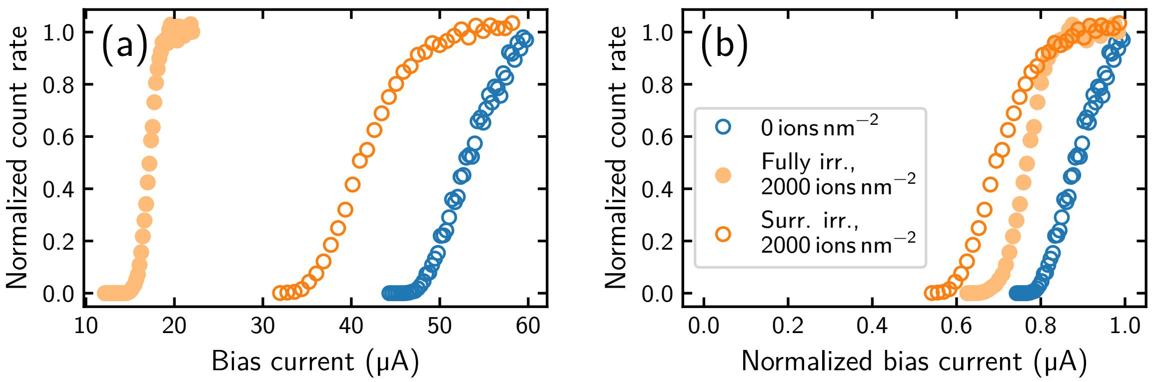

Figure 4.11: Normalized count rate versus bias current for three differently irradiated SNSPDs. (a) The count rate is normalized to the fit asymptote after fitting an error function [193], and plotted against the absolute bias current. (b) The same data as in (a) but with the bias current normalized to the photon-assisted critical current of the SNSPD. The measurements were performed at a wavelength of 780 nm and a temperature of 1 K. Adapted from [162], used under CC BY 4.0.

4.4.3 Enhanced detector performance via local thermal conductance modification

To experimentally investigate the irradiation strategy introduced in Section 4.4.1, we measure the detection efficiency of (1) an unirradiated reference device, (2) a device fully irradiated with 2000 ions nm^{-2}, and (3) a device where we irradiated only the surrounding regions up to a distance of 150 nm from the wire edge with 2000 ions nm^{-2}. The SNSPDs consist of 250 nm wide and 8 nm thick nanowires, with all experiments conducted at a temperature of 1 K using incident photons with a wavelength of 780 nm. The measurement platform development and design considerations for this low-temperature regime are detailed in Appendix E, including the special RF wiring and thermalization techniques necessary for cryogenic operation. Most importantly, Figure 4.11a and b show that both irradiated devices exhibit saturating detection efficiency, while the unirradiated device does not reach saturation.

To further characterize these detectors, we define what we term the *photon-assisted critical current*, $I_{c,pa}$, as the minimum current at which the SNSPD shows non-zero resistance under constant illumination with photons of 780 nm wavelength. We note that the conventional critical current is defined as the current where a superconductor transitions from the superconducting to the normal conducting state in dark conditions. However, in the context of SNSPDs operated with shunt resistors the critical current is typically defined as the current where the SNSPD transitions to a state where it shows on average a non-zero resistance in dark conditions—being either in a continuously normal conducting state, or a state where the SNSPD shows relaxation oscillations [57]. While we could measure the photon-assisted critical current for all devices in this section, the critical current in dark conditions could not be determined for all devices

	unirr.	surr. irr.	fully irr.
I_{sw} before irradiation	79.1	80.8	95.2
I_{sw} after irradiation	74.5	42.5	19.7
$I_{\mathrm{c,pa}}$ after irradiation	60.1	59.0	22.4

Table 4.1: Comparison of photon-assisted critical currents and switching currents (in µA) of the three devices discussed in Section 4.4.3. The unirradiated device was always measured as reference device and also in the rows "I_{sw} after irradiation" as well as "$I_{\mathrm{c,pa}}$ after irradiation" it was never irradiated. Reproduced from [162], used under CC BY 4.0.

since not all of them exhibited dark counts or relaxation oscillations with the 10.2 Ω shunt resistor and 1 s integration time used in these experiments. Nevertheless, the photon-assisted measurement ensures a consistent comparison across all devices, though we note that photon absorption can trigger the superconducting-to-normal transition at currents below the dark critical current. Using this definition, we observe that the photon-assisted critical current of the fully irradiated device is reduced to 22.4 µA, while the device where only the surrounding area was irradiated exhibits a similar value as the unirradiated device (59.0 µA and 60.1 µA, respectively). At the same time, we measured the switching current in these experiments without a shunt resistor (since a shunt resistor influences the nominal switching current [119]) and without illumination and observed its reduction not only for the fully irradiated device but also for the device where only the surrounding area was irradiated. Table 4.1 shows a comparison of these currents for the different devices before and after irradiation. The fact that the switching current is lower than the photon-assisted critical current for the devices with the full wire or the surrounding area irradiated might be explained by latching, since for switching current measurements no shunt resistor was connected. Surprisingly, the switching current for the unirradiated device is higher than its photon-assisted critical current. However, when comparing the two devices "surrounding irradiated" and "fully irradiated", a clear trend can be observed: Despite that the switching current for both devices is reduced after irradiation, the reduction is much less pronounced for the device with the surrounding irradiated (42.5 µA compared to 19.7 µA, corresponding to reductions by 47 % and 79 %). This is even more apparent when comparing the photon-assisted critical current after and the switching current before irradiation (a reduction by 27 % compared to 76 %). The fact that also the switching current of the device where only the surrounding area was irradiated is reduced might be explained by He ions that reach the nanowire due to back scattering and recoil events as elaborated in Section 4.4.2.

Examining the count rate curves in Figure 4.11 in more detail, it is noteworthy that the relative saturation plateau width is of similar size (16.6 %) and the absolute saturation plateau width is substantially larger for the wire with only the surrounding area irradiated compared to the fully irradiated wire (9.8 µA compared to 3.7 µA). This is particularly interesting since the wire itself was not irradiated and, moreover, the number of He atoms underneath the wire is on average only 3.9 % of that underneath the fully irradiated wire, as calculated in the previous section. We note that even if the photon-assisted critical current of the unirradiated device had been higher than and not similar to that of the surrounding irradiated device, the switching current and the photon-assisted critical current of the device for which the surrounding area was irradiated would still be substantially higher than those of the fully irradiated device, while their relative saturation plateau width is similar. These observations imply that irradiating only the surrounding area increases the sensitivity due to the reduced thermal conductance to the substrate, and simultaneously the sensitivity stays high since the photon-assisted critical current is barely reduced. In contrast, we typically observe a strong reduction of the critical current after full irradiation of SNSPDs [111]. This suggests that for devices where only the surrounding area is irradiated, higher He ion fluences might be explored in future work to potentially achieve even larger saturation plateau widths. The irradiation approach of this section complements the technique presented in Chapter 3, where the straight nanowire segments of meander-shaped SNSPDs are locally irradiated to mitigate current crowding. Together, these methods provide complementary strategies for enhancing detector performance while preserving high critical currents.

The most important conclusion of this experiment is that despite irradiating only the surrounding region of the nanowire, its sensitivity to single photons increased significantly. This would not be possible if a modification of the NbTiN via direct He ion irradiation was the only cause for a change in detector properties after irradiation. Thus, other mechanisms such as the irradiation-induced reduction of the thermal conductance from the detector to the substrate substantially contribute to the change in detector properties after irradiation.

4.5 Summary and outlook

Motivated by the significant improvement of SNSPD performance following He ion irradiation [104, 111, 152], we investigated the irradiation-induced changes of the superconducting NbTiN films and the underlying SiO_2/Si substrates. Through combined TEM and AFM analysis, we found that irradiating the NbTiN/SiO_2/Si stack with 30 kV He ions transforms the crystalline Si into an amorphous structure, with He bubbles forming between the SiO_2/Si interface (at 150 nm depth) and 340 nm depth, causing substrate swelling. At the same time, the NbTiN film remains polycrystalline with columnar crystalline domains and an oxygen-rich top layer. However, the originally flat NbTiN film exhibits an increasing wrinkling with increasing He ion fluence since stress in the as-sputtered NbTiN film can be released due to viscous flow of the SiO_2 that allows its plastic deformation during He ion irradiation.

Moreover, experiments revealed a decrease in the thermal conductance from the NbTiN to the substrate with increasing He ion fluence from initially $210\,\mathrm{W\,m^{-2}\,K^{-4}}$ to $70\,\mathrm{W\,m^{-2}\,K^{-4}}$ after irradiation with $2000\,\mathrm{ions\,nm^{-2}}$. Combined with the observations for the influence of He ion irradiation on film and substrate morphology, this suggests the following: in addition to the effects of direct He ion irradiation on the NbTiN film, a substantial contribution to the enhanced SNSPD performance originates from an irradiation-induced reduction of the thermal conductance. This reduction, caused by He bubbles, amorphization of crystalline Si, and a modified NbTiN-SiO_2 interface, leads to a prolonged lifetime of the normal-conducting domain, thereby increasing the detection probability. To verify this hypothesis, we irradiated the surrounding area of a straight nanowire up to a distance of 150 nm from the wire. Due to scattering, the He ions spread laterally when moving through the sample and result in a reduced thermal conductance also underneath the nanowire. Although we did not irradiate the nanowire directly, we observed a similar relative saturation plateau width (16.6 %), a significantly larger absolute saturation plateau width (9.8 µA compared to 3.7 µA), and a higher photon-assisted critical current (59.0 µA compared to 22.4 µA) after irradiation of the surrounding area of the nanowire with $2000\,\mathrm{ions\,nm^{-2}}$, compared to full irradiation with the same He ion fluence. This confirms that the reduced thermal conductance substantially contributes to the enhanced sensitivity following He ion irradiation. Moreover, irradiation of the area surrounding the nanowire provides a means to reduce the thermal conductance underneath the nanowire while maintaining a high photon-assisted critical current due to the limited interaction of He ions with the NbTiN film.

To further differentiate the effects of the He ions on the NbTiN film versus the substrate, it would be valuable to compare detectors fabricated on pre-irradiated substrate regions with those fabricated on unirradiated substrate regions and then irradiated. Moreover, since the He implantation depth, which also defines the thickness of the heat conducting channel, can be tuned via the acceleration voltage, investigating the influence of different acceleration voltages on both device and substrate properties could provide valuable insights for optimizing detector performance.

The investigations in this chapter identify a reduced thermal conductance as a major contributing factor to the performance enhancements observed in Chapters 2 and 3, providing a unifying explanation for our earlier findings. While advancing fundamental understanding of the effects of He ion irradiation on both films and substrates, this chapter also establishes substrate engineering as a powerful approach for SNSPD optimization beyond direct superconductor modification, opening new pathways for next-generation single-photon detectors.

5 Conclusions and future perspectives

In this thesis, we have demonstrated how precisely controlled helium (He) ion irradiation can fundamentally transform the performance of superconducting nanowire single-photon detectors (SNSPDs). Through the development and systematic investigation of three complementary irradiation techniques, we have achieved significant breakthroughs in detector improvement while advancing our understanding of the underlying physical mechanisms responsible for these enhancements.

Beginning with fundamental investigations, we provided the first demonstration of site-selective He ion irradiation for enhancing SNSPD performance. A key breakthrough was the substantial improvement of thick NbTiN detectors. While films of 8 nm to 10 nm thickness are typically used to maintain single-photon sensitivity, we showed that He ion irradiation could transform 12 nm thick detectors from their initially negligible detection efficiency ($< 0.05\,\%$) to 55.3 %. This represents a significant advance, as thicker films provide higher absorption efficiency, while traditionally suffering from reduced detection capability. Furthermore, site-selective irradiation enables post-fabrication optimization of individual SNSPDs on the same chip, allowing for more uniform performance across detector arrays. To qualitatively describe the evolution of sheet resistance and critical temperature with increasing He ion fluence, we developed a physical model accounting for defect generation and surface sputtering effects during He ion irradiation, allowing us to predict and optimize irradiation parameters. These results formed the foundation for our subsequent investigations of more sophisticated irradiation techniques.

To understand the mechanisms behind these improvements, we characterized samples irradiated with various He ion fluences via transmission electron microscopy, atomic force microscopy, and transport measurements. We found that He ion irradiation transforms the crystalline Si substrate into an amorphous structure and leads to the formation of He bubbles between the SiO_2/Si interface and 340 nm depth. These structural changes reduce the thermal conductance between the superconducting film and the substrate to only 33 % of its original value after irradiation with 2000 ions nm^{-2}, leading to a prolonged lifetime of the normal conducting domain during the photon

Chapter 5

detection process, which results in an increased detection probability. The significance of this thermal modification became particularly apparent when irradiating only the regions adjacent to a nanowire. Despite not directly irradiating the nanowire itself, we achieved saturating detection efficiency with substantially larger plateau widths compared to fully irradiated devices, while maintaining photon-assisted critical currents similar to unirradiated detectors. This enhancement stems from the lateral straggle of He ions deep in the substrate, which modifies the thermal conductance underneath the nanowire, while having only a small direct impact on the superconducting film. These findings highlight thermal conductance engineering as a powerful approach for SNSPD optimization.

Turning to a long-standing challenge in the field, we achieved a breakthrough in addressing current crowding, which fundamentally limits SNSPD performance particularly at low temperatures. We showed that current crowding in the 180° bends of meander-shaped SNSPDs (250 nm wire width, 71 % fill factor) reduces the maximum applicable bias current to only 60 % of that achievable in straight nanowires, thereby limiting detection efficiency and increasing dark count rates. To address this challenge, we demonstrated a novel solution by selectively irradiating only the straight segments of SNSPDs, while leaving their bends unirradiated. For He ion fluences above $(90 \pm 20)\,\mathrm{ions\,nm^{-2}}$, the critical current of the straight segments becomes lower than that of the bends, effectively eliminating current crowding as the limiting factor. Using this approach, we achieved a relative saturation plateau width of 37 % for locally irradiated SNSPDs compared to 10 % for fully irradiated devices at the same fluence. This larger plateau enables operation at lower relative bias currents, yielding dark count rates as low as 7 mHz while maintaining 94 % internal detection efficiency. Unlike other techniques for enhancing detection efficiency, this method uniquely achieves performance improvements without compromising critical device parameters such as switching current or critical temperature. More broadly, our achievements demonstrate how precise control of He ion irradiation patterns can modify detector properties both directly through changes to the superconducting film and indirectly via substrate modification, enabling unprecedented control over device performance.

Several promising research directions emerge from this work. A straightforward extension involves investigating the effects of the He ion acceleration voltage on detector performance. Since the acceleration voltage determines the implantation depth of He ions, this parameter could provide additional control over the thermal coupling between detector and substrate, potentially enabling further optimization of detection efficiency. The application of the techniques presented in this thesis to different materials and substrates presents another avenue for investigation. While our work focused on NbTiN films on SiO_2/Si substrates, exploring the effects of He ion irradiation on amorphous superconductors like MoSi or alternative substrate materials such as sapphire or AlN could reveal new optimization possibilities and physical insights. Particularly promising is an investigation and comparison of detectors fabricated on pre-irradiated substrate regions with those irradiated after fabrication. By this, we can separate the direct effects of irradiation on the superconducting film from those arising from substrate modification. This approach could lead to new fabrication strategies that optimize thermal properties without compromising superconducting film quality.

The most exciting possibilities arise from novel irradiation patterns. One particularly intriguing direction is the creation of nanoscale irradiation patterns across detector nanowires. By creating alternating irradiated and unirradiated regions with periods of a few tens of nanometers, we could potentially achieve quasiparticle trapping in irradiated areas due to their reduced superconducting energy gap [194]. This lateral confinement of quasiparticles could enhance sensitivity to longer-wavelength photons by promoting the formation of normal conducting domains across the nanowire width rather than along its length after photon absorption.

The combination of different irradiation techniques demonstrated in this work also holds significant potential. For instance, combining the irradiation of regions adjacent to nanowires for thermal conductance engineering with local irradiation of the straight segments for current crowding mitigation could potentially yield even better detector performance than either technique alone. While the benefits of such combinations remain to be fully explored, they exemplify the rich possibilities enabled by local He ion irradiation.

This thesis has significantly advanced the field of SNSPDs through systematic investigation and application of He ion irradiation. We demonstrated three complementary approaches to improve their performance: elimination of current crowding through local irradiation of the straight nanowire segments, reduction of thermal conductance through substrate modification, and transformation of thick detectors into efficient single-photon detectors through site-selective irradiation. Our investigation of the physical mechanisms behind these improvements revealed how He ion irradiation modifies both the critical temperature and sheet resistance of superconducting films through effects such as film wrinkling, while simultaneously altering substrate properties through amorphization and He bubble formation. These insights establish a framework for engineering substrates and superconducting devices through targeted modification of their material properties, opening new pathways for optimizing SNSPDs and other devices that rely on precise control of their local superconducting, electronic, and thermal properties.

A Simulation of optical absorption in SNSPDs

The optical absorption in a detector provides an upper limit for its SDE. To determine the absorption for the detectors fabricated in Chapter 2, we performed finite-difference time domain (FDTD) simulations (Ansys Lumerical). Input parameters for these simulations are the width and thickness of the nanowire and the optical constants of the superconducting film that provides the basis for the detector. We controlled the thickness of the films by measuring the sputter deposition rate and selecting the deposition time accordingly. The optical constants of the thin films were measured with a variable angle spectroscopic ellipsometer (M-2000, J.A. Woollam Co.) and, as shown in Table A.1, we observed an increase of the extinction coefficient with film thickness. Consequently, also for a thicker detector, the absorption does not only increase due to its larger thickness but also due to the higher extinction coefficient of the thicker film. After detector fabrication, we evaluated the width of 22 representative detectors (Genesys ProSEM) and determined their mean wire width as listed in Table A.1. Moreover, for the simulations we chose a plane-wave source with its polarization parallel to the nanowire, in line with the experiment. Table A.1 shows the simulation input parameters and results for the optical absorption of the detectors in Chapter 2. The design of all detectors in Chapter 2 consists of 100 nm wide wires and a fill factor of 50 % as described in Section 2.2. The measured width of the fabricated detectors deviates from this nominal value due to slight under-/overexposure during electron-beam lithography. This, however, does not change the reasoning within this work: For the same pitch, increased wire width (increased fill factor) or increased thickness both increase optical absorption and switching current, while reducing the detector's sensitivity to single photons.

Table A.1: Simulation parameters and results for the absorption in the 8 nm, 10 nm, and 12 nm thick detectors of Chapter 2. d_0 is the nominal thickness of the detector, while w represents its mean wire width. n and k are refractive index and extinction coefficient of the underlying *thin films*, respectively. The absorption fraction α denotes the percentage of light that is absorbed in the detector, obtained from FDTD simulations. Reproduced from [111], used under CC BY 4.0.

d_0 (nm)	w (nm)	n (1)	k (1)	α (%)
8	92.6 ± 4.0	2.47	3.18	44.2
10	107.3 ± 1.9	2.48	3.33	53.1
12	115.3 ± 3.4	2.48	3.54	57.7

B Critical temperature modeling using the universal scaling law

This appendix provides the details of the fitting procedure that we use to describe the dependence of the critical temperature T_c on the He ion fluence in Chapter 2 with the universal scaling law introduced by Ivry *et al.* [145]. Moreover, we explore various approaches to applying this scaling law to our experimental data, discuss the physical interpretation of model parameters, and compare alternative fitting methods. To describe the data for the critical temperature in Figure 2.8, we use the universal scaling law,

$$d\,T_c = A R_{sheet}^{-B} , \tag{B.1}$$

which relates film thickness, critical temperature, and sheet resistance [145]. Figure B.1 shows the critical temperature, multiplied with the thickness of the non-irradiated film, $d_0 T_c$. Evidently, this quantity exhibits a linear dependence on the sheet resistance on a log-log scale. As the data of the differently irradiated 8 nm, 10 nm, and 12 nm thick films approximately collapse on a single line, we choose one joint fitting function to determine the constants A and B of the universal scaling law and obtain the unitless constants $A = 1.44 \times 10^4$ and $B = 0.957$, provided that the data for d, T_c, and R_{sheet} are given in nm, K, and Ω, respectively. With these parameters, we obtain the fitting functions shown in Figure 2.8.

It is interesting to note that the linearity of the three data sets shown in the upper part of Figure B.1 is lost when multiplying T_c with the effective thickness $d_{eff} = d_0 - r_s F$ instead of the thickness before irradiation, as shown in the lower part of Figure B.1. As introduced in Section 2.3.2, this reduction of the effective thickness by 0.94 nm per 1000 ions nm^{-2} accounts for surface sputtering and intermixing at the film/substrate interface. At present, we can only give a qualitative explanation why the effective thickness is important to describe the continuous increase of R_{sheet} in Figure 2.7 and why it is not relevant for describing T_c: Via AFM measurements, we observed a surface roughening by He ion irradiation due to surface sputtering and redeposition. Considering now a thin slab of the rough surface parallel to the sample plane, it consists of many connected islands of NbTiN (or an oxide thereof). On the one hand, this slab has a higher resistivity in the normal conducting state due to the

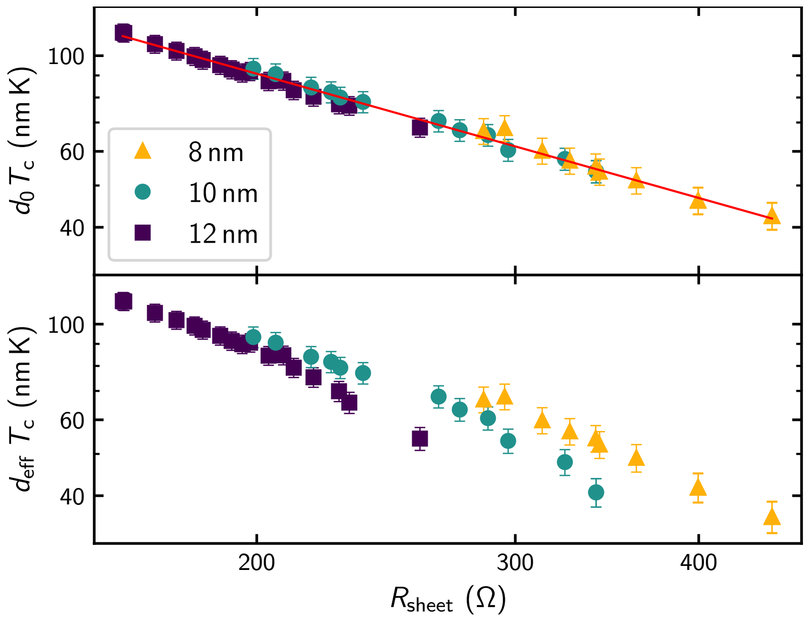

Figure B.1: Critical temperature multiplied with film thickness vs. sheet resistance, including statistical errors. In the upper plot the thickness of the non-irradiated film is used, while the effective thickness used in the lower plot accounts for surface sputtering and intermixing at the film/substrate interface due to He ion irradiation. The red line in the upper plot is a fit according to the universal scaling law introduced by Ivry *et al.* [145], $d_0 T_c = AR_{sheet}^{-B}$. Adapted from [111], used under CC BY 4.0.

voids; on the other hand, it should have a T_c similar to a slab without voids as long as the voids are smaller than the coherence length of the superconductor. Of course, further investigation is necessary to better understand the role of surface sputtering and intermixing at the film/substrate interface as well as their influence on thickness, sheet resistance, and critical temperature of the thin film.

Another approach to evaluate our data with the universal scaling law is based on the observation by Ivry *et al.* [145] that the parameters A and B are correlated and tend to be higher for amorphous films. Since He ion irradiation induces defects in the superconducting film, one might expect an increase in the parameters A and B with increasing He ion fluence. To investigate this in more detail, we fit the universal scaling law to the data in the lower part of Figure B.1, where an effective film thickness reduction was taken into account. However, this time we use an individual universal scaling law fit function for each set of data points that share the same He ion fluence (although this means that we only have 2–3 data points for each fit) and account for the thickness reduction with increasing He ion fluence,

$$d_{eff}\,T_c = AR_{sheet}^{-B}\ . \tag{B.2}$$

The resulting parameters A and B are shown in Figure B.2a. It is worth noting that we now have two fit parameters per He ion fluence, making a total of 24 parameters. We

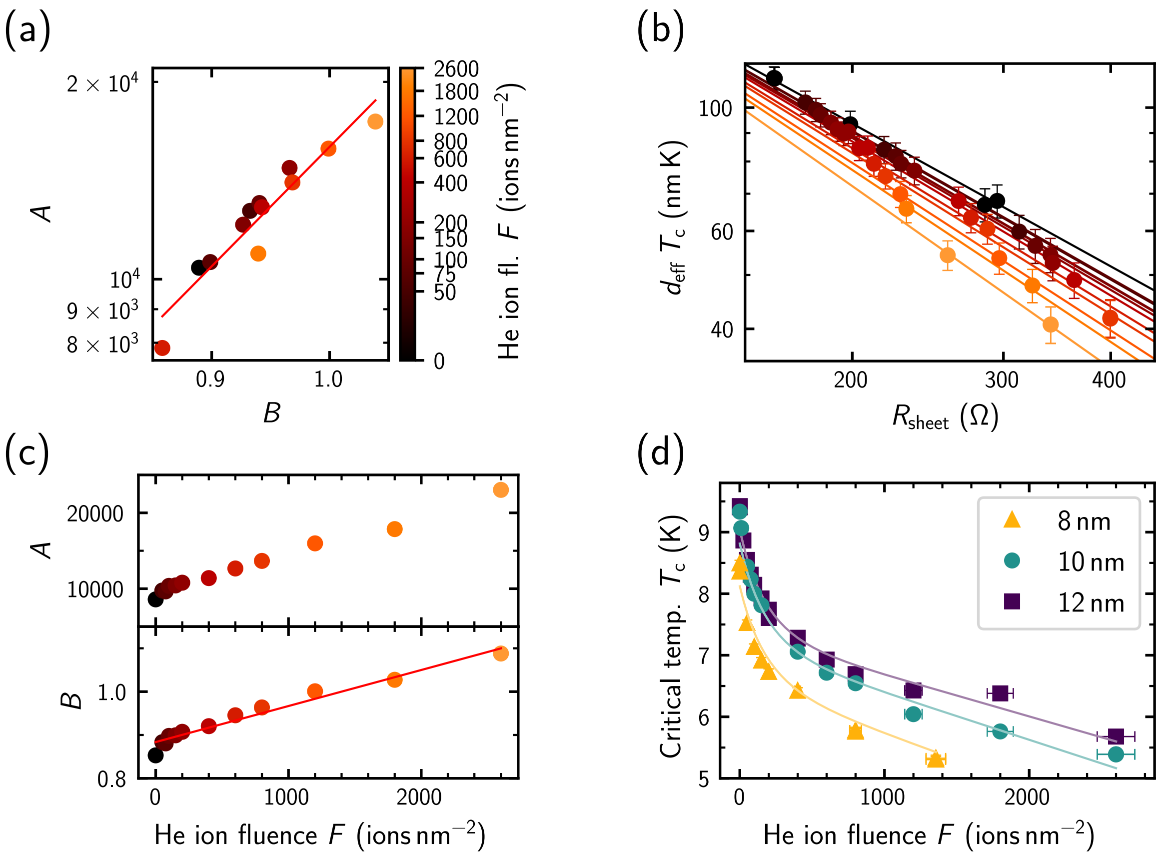

Figure B.2: Procedure for fitting the universal scaling law, Equation (B.2), to the data shown in the lower part of Figure B.1, where the effective thickness reduction due to surface sputtering during He ion bombardment is taken into account. (a) The resulting parameters A and B after performing a universal scaling law fit for each set of data points of devices irradiated with the same He ion fluence (color coded), given by the data in the lower part of Figure B.1. The red line is a linear fit of these correlated parameters in the log-linear plot. (b) Re-evaluation of the universal scaling law fits for each set of data points of the same He ion fluence after substituting A in Equation (B.2) by Equation (B.3). The resulting parameters A and B are shown in (c) along with a linear fit (red) to obtain an expression for the He ion fluence dependence of B. Finally, the expressions for $A(B)$ and $B(F)$, Equations (B.3) and (B.4), can be used with Equation (B.2) to obtain the continuous functions $T_c(F)$ shown in (d). Adapted from [111], used under CC BY 4.0.

observe a correlation between A and B similar to that in Figure 5a of the publication by Ivry *et al.* [145]. Therefore, we can reduce the number of fit parameters by performing a linear fit of the logarithmically plotted data and obtain the expression

$$A(B) = \exp(4.20B + 5.47924) \ , \tag{B.3}$$

shown as red line in Figure B.2a. Next, we re-evaluate our data in the lower part of Figure B.1 by fitting the universal scaling law to the same data as before, but using Equation (B.3) to express A by B, thereby reducing the number of fit parameters per He ion fluence to one (hence 12 instead of 24 fit parameters in total). The resulting fit functions and the parameters A and B for each He ion fluence are shown in Figure B.2b and Figure B.2c, respectively. The continuous increase of A and B with increasing He ion fluence agrees with the observation of Ivry *et al.* [145] that the more amorphous films have higher values for A and B. To obtain a continuous function for T_c similar to that in Figure 2.8, we use a linear fit as shown in Figure B.2c (red line) to describe the He ion fluence dependence of the parameter B by

$$B(F) = 8.31 \times 10^{-5} F + 0.88368 \ . \tag{B.4}$$

Finally, using Equations (B.2) to (B.4), we calculate $T_c(F)$ as shown in Figure B.2d. The advantages of this method compared to the simpler fitting procedure at the beginning of this section are, firstly, that we have taken into account the effective thickness reduction due to He ion irradiation and, secondly, that the increasing values for A and B with increasing He ion fluence support the model of defect cluster formation due to He ion irradiation. On the other hand, this method involves more fitting steps and more fitting parameters than the simpler procedure that yields all three fits in Figure B.3 with only two parameters.

In a recent publication, Ruhtinas & Maasilta [148] suggest an empirical logarithmic fit function as another alternative for the dependence of the critical temperature on the He ion fluence. As shown in Figure B.3, this fit function describes our data for the 12 nm thick film even a bit better than the universal scaling law in Figure 2.8. However, the logarithmic fit requires three fit parameters for each thickness (nine parameters in total), whereas the universal scaling law fit in Figure B.3 requires only two fit parameters to describe all three data sets.

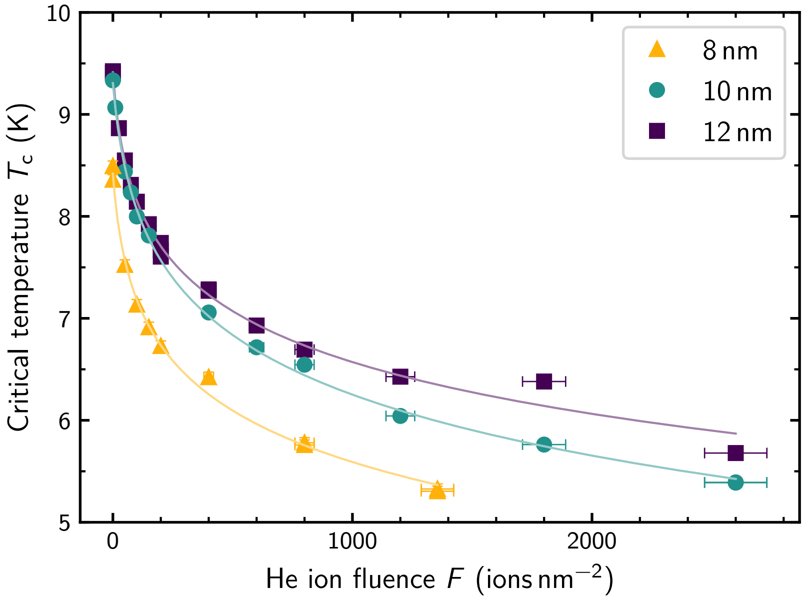

Figure B.3: Critical temperature vs. He ion fluence as shown in Figure 2.8, including statistical errors. In contrast to the fit with the universal scaling law in Figure 2.8, we fit our data here with a logarithmic function, $T_c(F) = -a \log(F + b) + c$, and fit parameters a, b, and c for each of the three thicknesses as suggested by Ruhtinas & Maasilta [148]. Adapted from [111], used under CC BY 4.0.

C Detailed analysis of count rate saturation plateau width

This appendix provides a detailed analysis of the absolute and the relative count rate saturation plateau width for locally and fully irradiated SNSPDs, expanding on the results presented in Section 3.5 of Chapter 3. The relative saturation plateau width is given by

$$\sigma_{\mathrm{rel}} = \frac{I_{\mathrm{c}} - I_{\mathrm{sat}}}{I_{\mathrm{c}}} , \tag{C.1}$$

with the absolute saturation plateau size given by the difference between the critical current I_{c} and the current I_{sat} where the saturation plateau begins. As noted in Section 3.5, we use a shunt resistor (20.4 Ω at 1 K) for the CR measurements to prevent latching of the detectors, causing the SNSPDs to transition to the relaxation oscillation regime at I_{c} before switching to the latching state. In this regime the SNSPD emits a periodic train of voltage pulses and the average voltage drop across the SNSPD increases with increasing bias current [57]. Figure C.1a shows the absolute saturation plateau width $I_{\mathrm{c}} - I_{\mathrm{sat}}$, where a steep increase in saturation plateau width is observed for He ion fluences up to 200 ions nm^{-2}, followed by a decrease beyond 600 ions nm^{-2}. At the same time, the critical current decreases with increasing He ion fluence. As shown in Figure C.1b, the resulting relative saturation plateau width increases for small He ion fluences, peaks between 600 ions nm^{-2} and 1000 ions nm^{-2} before it decreases again for higher fluences. This relation is even better visible in Figure C.1c after normalizing the saturation plateau width to the switching current of the devices without shunt resistor instead of the critical current during CR measurements.

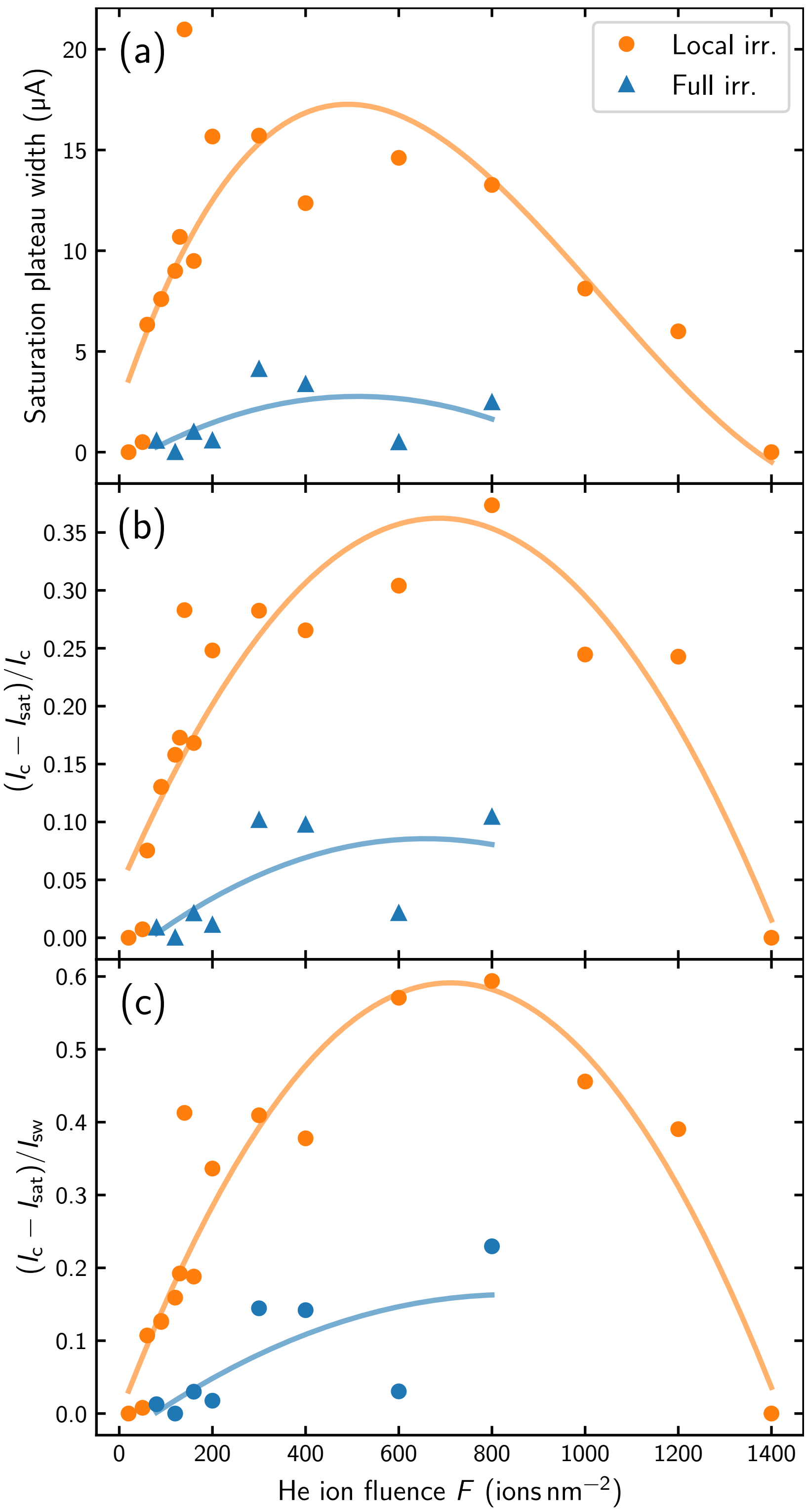

Figure C.1: Count rate saturation plateau width of locally and fully irradiated SNSPDs versus He ion fluence. (a) Absolute saturation plateau width. (b) Relative saturation plateau width as given in Equation (C.1). (c) Saturation plateau width, normalized to the switching current of the corresponding devices measured without shunt resistor. The solid lines serve as a guide to the eye. Adapted from [152], used under CC BY 4.0.

D Development of cost-effective multi-channel SNSPD biasing electronics

This appendix documents the design and implementation of a custom four-channel SNSPD biasing module developed to enable simultaneous operation of multiple detectors at significantly lower cost than commercial laboratory equipment. While standard laboratory setups typically require one Keithley 2450 source meter per channel (at approximately $7000 each), this custom module provides four independently controllable channels at a total component cost under $300, while maintaining precision voltage control and low noise characteristics.

D.1 Design overview

The SNSPD biasing module features a 16-bit digital-to-analog converter (DAC, Analog Devices AD5686) that provides four precision voltage output channels with an operating range of 0 V to 5 V and 16 bit resolution. Each output channel implements the following biasing principle: the DAC output voltage is applied across an integrated 50 kΩ series resistor connected to an SMA output, to which the user connects the DC arm of a bias-tee for the SNSPD. The module simultaneously measures the voltage drop across each series resistor using the Arduino's analog-to-digital converter (ADC), enabling real-time monitoring of the detector status while providing the bias current. During automated bias sweeps, the module incrementally increases the bias voltage while continuously monitoring this voltage drop. When a sudden change in voltage drop is detected—indicating the SNSPD has switched to its normal conducting state—the module identifies this point as the switching current. It then automatically calculates and applies the desired percentage of this switching current as the operating bias.

The system achieves excellent noise performance (< 2 mV with disconnected Arduino ADC and < 30 mV with connected ADC), and incorporates an internal voltage reference for stability. The voltage sensing capability not only enables automated switching current detection but also allows for continuous monitoring of detector performance during operation.

A key feature of the design is its scalability—the AD5686 DAC supports daisy-chaining, allowing expansion to any number of bias channels by adding additional

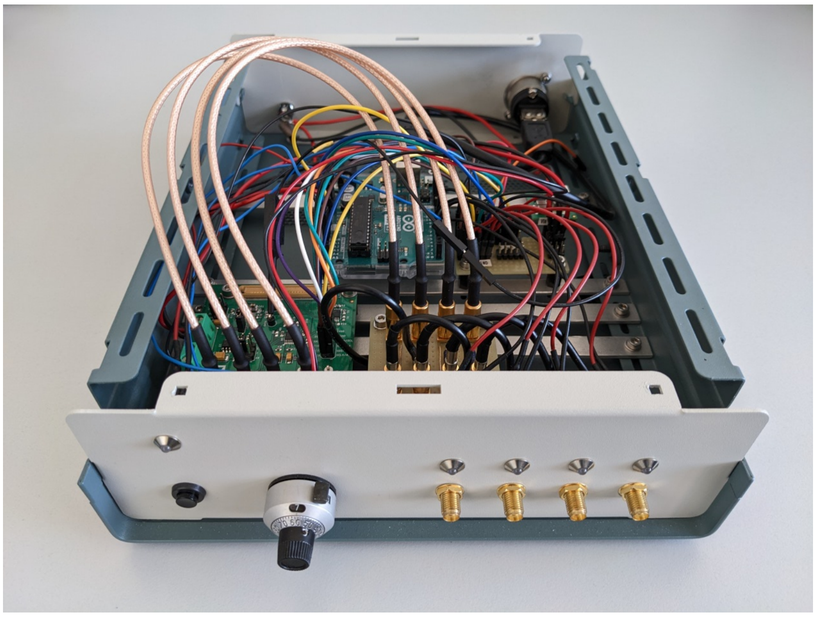

Figure D.1: The biasing module with open top cover, showing the EVAL-AD5686R evaluation board controlled with an Arduino UNO. The system provides simultaneous biasing of four individual channels, controllable either through standard SCPI commands via USB or through standalone operation using the integrated control interface.

DACs at a cost of less than \$30 per four channels. For scaling the simultaneous readout of the voltage drop across the integrated resistor, an external ADC such as the LTC2686 (Analog Devices, $<$ \$25 per 8 channels) can replace the integrated Arduino ADC. The module includes comprehensive firmware with dual control modes: computer operation via USB with standard SCPI commands, and standalone operation through an intuitive user interface consisting of a push button, potentiometer, and status LEDs.

D.2 Technical specifications

The biasing module has the following main specifications:

- Four independently controllable output channels
- Output voltage range: 0 V to 5 V (configurable to 0 V to 2.5 V), corresponding to bias currents ranging from 0 µA to 100 µA (0 µA to 50 µA)
- Resolution: 16 bit
- Noise performance: $<$ 2 mV (ADC disconnected), $<$ 30 mV (ADC connected)
- Communication: USB with SCPI command interface
- Integrated user interface for standalone operation
- Automatic bias sweeps for detection of SNSPD switching currents

D.3 Standalone operation

For standalone operation, the biasing module requires only a connection to a power supply. The integrated user interface provides complete functionality through the push button and potentiometer:

1. Use the potentiometer to select the percentage of switching current that should be applied for the bias current.
2. Press the push button briefly to select a channel. The currently selected channel is indicated by a blinking LED. Each additional brief press selects the next channel. Five brief presses selects all channels simultaneously.
3. Press the push button for a medium duration to confirm the channel selection. The module automatically performs a bias voltage sweep (0 V to 5 V) to determine the switching current of the connected SNSPD. After determining the switching current, the system automatically sets the bias current to the percentage selected via the potentiometer.
4. To reset all channels to 0 V, press the push button for a long duration until all LEDs turn off.

D.4 Computer control via USB

When connected to a computer via USB, the module accepts SCPI commands while still requiring a power supply connection to provide the full range of output voltages. The firmware interprets SCPI commands, enabling direct integration with existing laboratory control software and measurement automation scripts. This approach allows users to control the biasing module using the same command syntax as commercial instruments such as Keithley source meters, eliminating the need for specialized software development. The available SCPI commands are shown in Table D.1 and enable precise voltage control, automated measurement sequences, and detector characterization.

Command	Description
`*IDN?`	Requests identification string from the module.
`SOURce#:VOLTage`	Applies a specified voltage to output port #. Example to apply 2.1 V to output port 0: `SOURce0:VOLTage 2.1`
`SOURce#:VOLTage?`	Reads the voltage drop across the SNSPD on port #. Example to read the voltage drop over the SNSPD at output port 1: `SOURce1:VOLTage?`
`SOURce#:SWEep:VOLTage:LINear`	Performs a linear voltage sweep on channel # within specified parameters. Example to ramp channel 0 between 0 V to 5 V with 51 steps and a delay of 100 ms: `SOUR0:SWE:VOLT:LIN 0, 5, 51, 100`

`SOURce#:AUTObias`	Automatically determines the switching current and sets bias voltage to a specified percentage (default 80 %) of the switching voltage.
	Examples to perform voltage sweep between 0 V to 2.5 V in 4 s and 100 steps (default values):
	`SOUR0:AUTO 0.8, 0.0, 2.5, 4.0, 100`
	`SOUR0:AUTO`
	`SOUR:AUTO`

Table D.1: SCPI command set implemented for controlling the SNSPD biasing module via the USB interface. The command structure follows industry-standard SCPI syntax for compatibility with existing laboratory control systems.

D.5 Firmware implementation

The firmware is written in C/C++ and implements a finite state machine for user interface control and uses the SPI protocol for DAC control. Key components include:

- Finite state machine for intuitive user interaction
- Standardized SCPI command parser for computer control
- SPI communication with the AD5686 DAC
- Hardware timer-based debouncing for reliable button input
- Analog voltage readout for switching current detection

E Development of a measurement platform for SNSPDs in a sub-Kelvin cryostat

The He ion irradiation techniques explored in this thesis required extensive characterization of SNSPD performance at sub-Kelvin temperatures. This appendix documents the measurement platform developed to enable these experiments, with particular focus on the cryogenic wiring solutions implemented to minimize both thermal load and RF noise. These technical considerations were crucial for obtaining the high-quality detector performance data presented in Chapters 3 and 4. Additionally, we discuss future extensions of this platform to enable high-throughput characterization of multiple devices per cooldown using cryogenic RF switches, which will facilitate further studies of SNSPDs at sub-Kelvin temperatures.

E.1 Cryogenic wiring for low heat load and RF noise

To isolate the sample and the mK-stage from heat, several factors must be considered. Selecting cables with low thermal conductivity is crucial as this minimizes heat transfer from room temperature to each low-temperature stage. For this reason, we employ cupronickel cables (offering both low thermal conductivity and low attenuation) to connect the room-temperature stage to the 40 K stage, and the 40 K stage to the 4 K stage. For the connection between the 4 K stage and the mK stage, superconducting NbTi cables are used, providing low thermal conductivity and virtually no attenuation in their superconducting state.

Additionally, proper thermalization of cables at each stage is essential. For twisted-pair cables, this is typically accomplished by winding them around a copper bobbin. For coaxial cables, we utilize SMA female-female bulkheads at each stage to thermally connect the outer conductor to the stage. However, this approach alone is insufficient since the inner conductor remains both electrically and thermally isolated from the outer conductor. Consequently, even with a properly thermalized outer conductor, heat would still propagate through the inner conductor. To address this issue, we place an attenuator directly between the cable and SMA bulkhead at each stage, creating a thermal bridge between the inner and outer conductors. These measures ensure that the cables reach the lowest possible temperatures at each stage, minimizing heat transfer to subsequent stages.

Beyond thermal conduction, we must also consider black body radiation transmitted through the cables as thermal photons, commonly known as Johnson-Nyquist noise in electronics. Similar to thermal photons transmitted through optical fibers to the detector, they can trigger dark counts in the detector. As our measurements and literature [159, 160] demonstrate, thermal blackbody radiation significantly contributes to the dark count rate in SNSPDs, particularly when operating them at bias currents close to their switching current.

Following the approach described in [195, 196], the two-sided power spectral density of voltage fluctuations $\delta V(t)$ of Johnson-Nyquist noise—the one-dimensional analog to Planck's law of black-body radiation—for a resistor R or a coaxial cable with characteristic impedance R is given by

$$S_V^{\text{th}}(T,\omega) = \int_{-\infty}^{\infty} \mathrm{d}t \langle \delta V(0)\, \delta V(t) \rangle e^{-i\omega t} \tag{E.1}$$

$$= 2R\hbar\omega \, \frac{1}{\exp(\hbar\omega/k_{\mathrm{B}}T) - 1} \tag{E.2}$$

$$= 2R\hbar\omega \, n_{\mathrm{BE}}(T,\omega)\ . \tag{E.3}$$

The last factor represents the Bose-Einstein distribution $n_{\mathrm{BE}} = \frac{1}{\exp(\hbar\omega/k_{\mathrm{B}}T)-1}$, which can be interpreted as photon flux spectral density—the number of photons per Hertz frequency interval and second [195]. In the classical limit $\hbar\omega \ll k_{\mathrm{B}}T$, this reduces to the original Johnson-Nyquist formula

$$S_V^{\text{th}}(T,\omega) = 2k_{\mathrm{B}}TR\ . \tag{E.4}$$

These thermal photons cannot be eliminated merely by thermalizing the cable; they must be blocked either by RF isolators (similar to three-port RF circulators with one port terminated by a matched load) or by a series of attenuators providing sufficient damping. However, since RF isolators typically offer only narrow bandwidth (a few tens or hundreds of MHz), they are unsuitable for our application, which requires substantially wider bandwidth (up to several GHz) to accommodate the fast-rising signals from our SNSPDs.

To determine the necessary attenuation at each stage, we must ensure that the photon flux spectral density from higher temperature stages is reduced to a level no greater than that of the low-temperature stage itself. Given that lower-temperature electronics also emit thermal photons with their own spectral density, the occupation number n_i after an attenuator thermalized at stage i with temperature $T_{i,\text{att}}$ can be calculated from the previous stage's occupation number n_{i-1} and the attenuation A_i [195] via

$$n_i(\omega) = \frac{n_{i-1}(\omega)}{A_i} + \frac{A_i - 1}{A_i} n_{\mathrm{BE}}(T_{i,\mathrm{att}}, \omega) \tag{E.5}$$

or, in the classical limit where $\hbar\omega \ll k_{\mathrm{B}}T$,

$$T_i = \frac{T_{i-1}}{A_i} + \frac{A_i - 1}{A_i} T_{i,\mathrm{att}} \ , \tag{E.6}$$

with T_i being the effective noise temperature after stage i. Solving this equation for the attenuation A_i, we obtain

$$A_i = \frac{T_{i-1} - T_{i,\mathrm{att}}}{T_i - T_{i,\mathrm{att}}} \ . \tag{E.7}$$

This formula allows us to calculate the necessary attenuation between stages $i-1$ and i to reduce the effective noise temperature from T_{i-1} to T_i, when the attenuator is thermalized to stage i with temperature $T_{i,\mathrm{att}}$.

We have calculated the necessary attenuation for various configurations, as shown in Table E.1. It is important to note that the fraction of power not passing through the attenuator is dissipated within it, generating heat at the corresponding stage. Since cooling power is limited for each stage—especially for the coldest stages—it is standard practice to distribute the necessary total attenuation across different stages rather than concentrating it all at the coldest stage [195]. In our case, for example, a reasonable distribution would place 10 dB of attenuation at the 40 K stage and 15 dB at the 4 K stage.

However, our implementation takes advantage of the cryogenic amplifier CITLF3 (Cosmic Microwave Technology) used in our setup, which provides isolation in the reverse direction exceeding 35 dB. This isolation sufficiently dampens thermal photons traveling down the coaxial lines from higher temperature stages, ensuring that thermal contribution from room temperature is reduced below the level of thermal emission from the 4 K electronics themselves. Therefore, we employ 0 dB attenuators at the 40 K and 4 K stages, which thermalize the inner conductor without attenuating the signal. Figure E.1 shows the resulting cabling between the room-temperature flange and the 40 K stage of the cryostat.

For the connection between the 4 K stage and the mK stage, we have made a deliberate design choice based on signal quality considerations. While Table E.1 shows the theoretical attenuation values needed to achieve various noise temperatures, adding attenuators at the mK stage would significantly reduce the amplitude of detection pulses from our SNSPDs. Since a noise temperature of 4 K to 5 K (the effective noise temperature achieved after the cryogenic amplifier) already represents a substantial

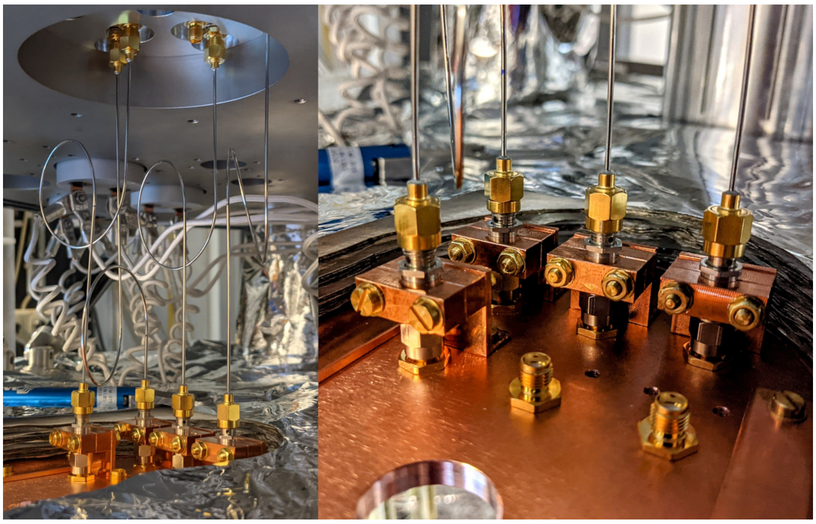

Figure E.1: RF cabling configuration between room temperature and the 40 K stage of the cryostat. Left: Semi-rigid coaxial cupronickel cables connect to SMA vacuum feedthroughs at the cryostat flange and incorporate strain-relief loops before reaching the 40 K stage. Right: At the 40 K stage, the cables terminate in 0 dB attenuators serving as thermal bridges between the inner and outer conductors. These attenuators are mounted to SMA bulkheads and clamped with copper brackets to ensure efficient thermalization to the 40 K stage.

Table E.1: Required attenuation values to achieve target noise temperatures between different cryogenic stages. The values show the theoretical attenuation needed to reduce the effective noise temperature from T_{i-1} to T_i when the attenuator on stage i is thermalized at temperature $T_{i,\mathrm{att}}$.

T_{i-1} (K)	$T_{i,\mathrm{att}}$ (K)	T_i (K)	A_i (1)	A_i (dB)
300	4.0	5.0	296	24.7
300	40.0	41.0	260	24.1
41	4.0	5.0	36	15.7
5	1.0	2.0	4	6.0
5	0.1	0.2	49	16.9

improvement over our previous measurement setups with their noise temperature of 300 K, we have also placed 0 dB attenuators at the mK stage to thermalize the inner conductor without reducing signal strength.

E.2 Perspectives for high-throughput characterization with cryogenic RF switches

The limited cooling power of cryostats restricts the number of RF cables and cryogenic amplifiers that can be deployed simultaneously. Our current configuration integrates four RF channels (three with cryogenic amplifiers and one reference channel without amplification). Despite the cryostat's fast-loading mechanism, the constraint of characterizing only four devices per cooldown significantly limits measurement throughput. Therefore, a solution enabling mass characterization is highly desirable.

RF switches provide an elegant solution by mapping multiple individual devices on the sample puck's PCB to a single RF channel. When implementing such a system, it is critical to select appropriate switches that function reliably under cryogenic conditions. Standard CMOS switches are unsuitable due to carrier freeze-out at low temperatures [197–199]. Instead, GaAs-based devices remain operational even at dilution refrigerator temperatures [200] and are a proven technology for this application. The Macom MASW-011107-DIE [201] exemplifies a suitable commercial option. This GaAs HEMT-based single pole double throw (SPDT) broadband non-reflective switch operates from DC to 26.5 GHz, providing RF performance with < 2 dB insertion loss, > 40 dB isolation, and 20 ns switching times between channels.

By implementing a tree network of such switches, we can expand our characterization capacity from four to potentially dozens of devices per cooldown. Each primary RF channel can address multiple devices sequentially, with the specific device selection controlled via DC bias lines. This approach maximizes the utility of our limited RF resources while maintaining the signal integrity necessary for precise SNSPD characterization.

F Development of a plug-and-play fiber-coupled SNSPD system

Practical deployment of SNSPDs beyond laboratory environments requires robust and efficient optical interfaces as well as convenient cryogenic systems. Fiber coupling is particularly essential as it enables turnkey "plug-and-play" integration of SNSPDs into existing optical systems without complex beam alignment procedures, significantly lowering the barrier to adoption in quantum communication networks, quantum key distribution systems, and other photonic applications. Furthermore, fiber coupling minimizes coupling losses, reduces sensitivity to mechanical vibrations, and protects the detector's active area from environmental contamination. To create a complete and user-friendly detection system, we developed both a fiber coupling solution for our SNSPDs and a specialized dip-stick cryostat that together form an integrated platform for practical single-photon detection at cryogenic temperatures.

To enable practical utilization of our fiber-coupled SNSPDs in various experimental setups, we designed and constructed a dip-stick cryostat that incorporates all necessary feedthroughs for coaxial cables, DC lines, and optical fibers that support wavelengths of 780 nm and 1550 nm, as shown in Figure F.1. With this integrated platform, users can simply insert the stick into a liquid He dewar and connect the appropriate optical and electrical connections without any need for complex alignment procedures.

The heart of this system is our custom fiber coupling solution that securely interfaces optical fibers with the SNSPD active area. Inspired by the approach of [202], we developed a mounting technique that combines deep reactive ion etching (DRIE) to create a "lollipop" structure from the wafer that supports the SNSPD, with a precision-engineered mounting system for reliable and stable optical alignment. The fiber coupling assembly consists of several key components as illustrated in Figure F.2. The main elements include a precisely machined copper mount and a modified FC/APC coupler (Thorlabs ADAFC3). The assembly procedure begins by placing the DRIE-processed lollipop-shaped wafer piece, which contains the SNSPD at its center, onto the designated pillar and slot of the copper block. Next, a zirconia ferrule mating sleeve is carefully slid over both the detector and the copper pillar. A critical design feature is the fillet between the copper pillar and the bulk copper, which matches exactly the

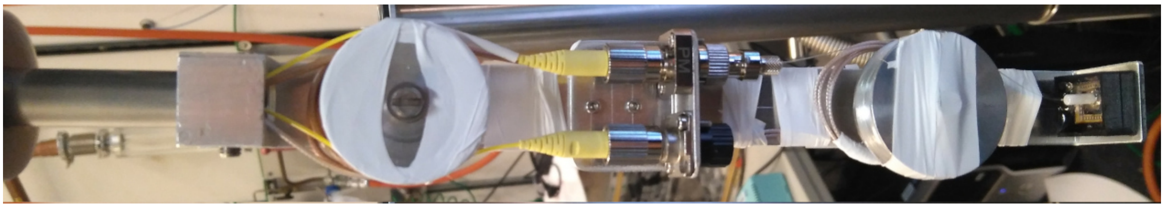

Figure F.1: Open bottom part of the dip-stick cryostat for characterization and use of fiber-coupled detectors. Depending on the use-case, we can connect the SNSPD to either of the built-in single-mode fibers for the wavelengths 780 nm and 1550 nm. The two mandrels are for looping up excess fiber and to simultaneously reduce the dark counts by macrobending loss of thermal radiation traveling through a curved fiber. One coax-line is for the electrical connection of the SNSPD and two lines are for 4-wire sensing of the temperature sensor.

width of the zirconia mating sleeve opening, preventing rotation and protecting the detector from mechanical damage. The printed circuit board (PCB) is then secured to the copper mount, and the detector is wire bonded to the PCB, which incorporates a mini-SMP RF connector for electrical biasing and signal readout. To complete the assembly, a stainless steel coupler is positioned over the zirconia mating sleeve and fastened with four brass screws, ensuring the stability of the entire structure. During development, we experimented with various slot depths to optimize the spacing between the detector and the fiber ferrule end facet. Contrary to initial concerns about potential damage, we discovered that allowing direct contact between the ferrule and the detector provides the most stable coupling without compromising detector integrity. This approach eliminates air gaps and minimizes coupling losses.

The resulting fiber-coupled SNSPD module, leveraging the robustness of the FC/APC connector standard, provides a mechanically stable and user-friendly solution. When integrated with our custom-designed dip-stick cryostat, the system forms a complete, ready-to-use single-photon detection platform operating at 4.2 K.

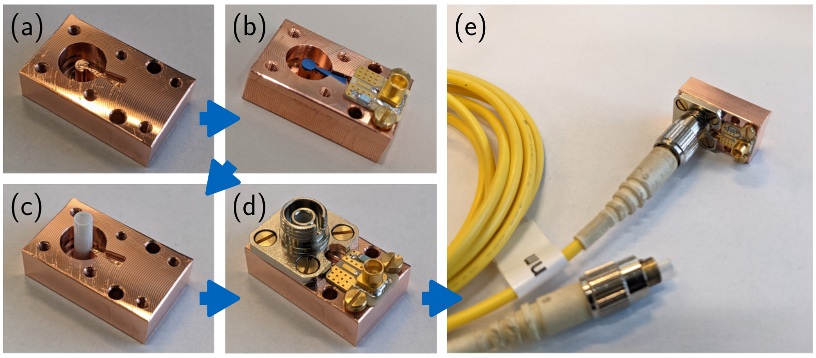

Figure F.2: Assembly of a detector with the self-developed fiber coupling mount. (a) The milled copper mount. (b) Placing of the detector with the supporting deep-reactive-ion etched lollipop silicon structure on the copper mount, mounting of the PCB, and bonding of the detector to the PCB. (c) Sliding the zirconia ferrule over the SNSPD onto the copper pillar (detector and PCB not shown). (d) Mounting the modified FC/APC fiber coupler on the copper mount, securing the zirconia mating sleeve. (e) Final assembly, attached to a fiber with FC/APC connector.

List of abbreviations

ADC Analog-to-digital converter
AFM Atomic force microscope
APD Avalanche photodiode

DAC Digital-to-analog converter
DCR Dark count rate
DRIE Deep reactive ion etching

EDX Energy-dispersive X-ray spectroscopy

FDTD Finite-difference time domain
FWHM Full width at half maximum

HAADF High-angle annular dark-field
He Helium
HIM Helium ion microscope

IDE Intrinsic detection efficiency

MgB_2 Magnesium diboride
MoGe Molybdenum germanium
MoSi Molybdenum silicide

NbN Niobium nitride
NbTiN Niobium titanium nitride

PCB Printed circuit board
PMT Photomultiplier tube

RF Radio frequency
RMS Root mean square

SCPI Standard Commands for Programmable Instruments
SDE System detection efficiency
SEM Scanning electron microscope
SNSPD Superconducting nanowire single-photon detector
SPAD Single-photon avalanche diode
SPDT Single pole double throw
SRIM Stopping and Range of Ions in Matter
STEM Scanning transmission electron microscope

TEM Transmission electron microscope
TES Transition edge sensor

WSi Tungsten silicide

Bibliography

1. Tamimi, A. *et al.* Deep Mouse Brain Two-Photon Near-Infrared Fluorescence Imaging Using a Superconducting Nanowire Single-Photon Detector Array. *ACS Photonics* **11,** 3960–3971 (2024).
2. Wang, F. *et al.* In Vivo Non-Invasive Confocal Fluorescence Imaging beyond 1,700nm Using Superconducting Nanowire Single-Photon Detectors. *Nat. Nanotechnol.* **17,** 653–660 (2022).
3. Xia, F. *et al.* Short-Wave Infrared Confocal Fluorescence Imaging of Deep Mouse Brain with a Superconducting Nanowire Single-Photon Detector. *ACS Photonics* **8,** 2800–2810 (2021).
4. Grein, M. E. *et al.* An Optical Receiver for the Lunar Laser Communication Demonstration Based on Photon-Counting Superconducting Nanowires. *Adv. Photon Count. Tech. IX* **9492,** 949208 (2015).
5. Wollman, E. E. *et al.* Recent Advances in Superconducting Nanowire Single-Photon Detector Technology for Exoplanet Transit Spectroscopy in the Mid-Infrared. *J. Astron. Telesc. Instrum. Syst.* **7,** 011004 (2021).
6. Takesue, H. *et al.* Quantum Key Distribution over a 40-dB Channel Loss Using Superconducting Single-Photon Detectors. *Nat. Photonics* **1,** 343–348 (2007).
7. Chen, J.-P. *et al.* Quantum Key Distribution over 658 Km Fiber with Distributed Vibration Sensing. *Phys. Rev. Lett.* **128,** 180502 (2022).
8. Liu, Y. *et al.* Experimental Twin-Field Quantum Key Distribution over 1000 Km Fiber Distance. *Phys. Rev. Lett.* **130,** 210801 (2023).
9. Slussarenko, S. & Pryde, G. J. Photonic Quantum Information Processing: A Concise Review. *Appl. Phys. Rev.* **6,** 041303 (2019).
10. Gyger, S. *et al.* Reconfigurable Photonics with On-Chip Single-Photon Detectors. *Nat. Commun.* **12,** 1408 (2021).
11. Ferrari, S., Schuck, C. & Pernice, W. Waveguide-Integrated Superconducting Nanowire Single-Photon Detectors. *Nanophotonics* **7,** 1725–1758 (2018).

12. Sprengers, J. P. *et al.* Waveguide Superconducting Single-Photon Detectors for Integrated Quantum Photonic Circuits. *Appl. Phys. Lett.* **99,** 181110 (2011).

13. Reithmaier, G. *et al.* On-Chip Time Resolved Detection of Quantum Dot Emission Using Integrated Superconducting Single Photon Detectors. *Sci. Rep.* **3,** 1901 (2013).

14. Reithmaier, G. *et al.* On-Chip Generation, Routing, and Detection of Resonance Fluorescence. *Nano Lett.* **15,** 5208–5213 (2015).

15. Majety, S. *et al.* Triangular Quantum Photonic Devices with Integrated Detectors in Silicon Carbide. *Mater. Quantum Technol.* **3,** 015004 (2023).

16. Natarajan, C. M., Tanner, M. G. & Hadfield, R. H. Superconducting Nanowire Single-Photon Detectors: Physics and Applications. *Supercond. Sci. Technol.* **25,** 063001 (2012).

17. Wollman, E. E. *et al.* SNSPD-based Detector System for NASA's Deep Space Optical Communications Project. *Opt. Express* **32,** 48185–48198 (2024).

18. Biswas, A. *et al.* Status of NASA's Deep Space Optical Communication Technology Demonstration. in *2017 IEEE International Conference on Space Optical Systems and Applications (ICSOS)* (IEEE, Naha, 2017), 23–27.

19. Hochberg, Y. *et al.* Detecting Sub-GeV Dark Matter with Superconducting Nanowires. *Phys. Rev. Lett.* **123,** 151802 (2019).

20. Chiles, J. *et al.* New Constraints on Dark Photon Dark Matter with Superconducting Nanowire Detectors in an Optical Haloscope. *Phys. Rev. Lett.* **128,** 231802 (2022).

21. Polakovic, T., Armstrong, W., Karapetrov, G., Meziani, Z. E. & Novosad, V. Unconventional Applications of Superconducting Nanowire Single Photon Detectors. *Nanomaterials* **10,** 1198 (2020).

22. Peña, C. *et al.* High Energy Particle Detection with Large Area Superconducting Microwire Array. *J. Instrum.* **20,** P03001 (2025).

23. Shigefuji, M. *et al.* Efficient Low-Energy Single-Electron Detection Using a Large-Area Superconducting Microstrip. arXiv: 2301.11212. (02/10/2023). Pre-published.

24. Zapatero, V. *et al.* Advances in Device-Independent Quantum Key Distribution. *npj Quantum Inf.* **9,** 10 (2023).

25. Trushechkin, A. Security of Quantum Key Distribution with Detection-Efficiency Mismatch in the Multiphoton Case. *Quantum* **6,** 771 (2022).

26. Zhang, Y., Coles, P. J., Winick, A., Lin, J. & Lütkenhaus, N. Security Proof of Practical Quantum Key Distribution with Detection-Efficiency Mismatch. *Phys. Rev. Res.* **3,** 013076 (2021).

27. Shibata, H., Shimizu, K., Takesue, H. & Tokura, Y. Ultimate Low System Dark-Count Rate for Superconducting Nanowire Single-Photon Detector. *Opt. Lett.* **40,** 3428 (2015).

28. Korzh, B. *et al.* Demonstration of sub-3ps Temporal Resolution with a Superconducting Nanowire Single-Photon Detector. *Nat. Photonics* **14,** 250–255 (2020).

29. Cherednichenko, S., Acharya, N., Novoselov, E. & Drakinskiy, V. Low Kinetic Inductance Superconducting MgB_2 Nanowires with a 130ps Relaxation Time for Single-Photon Detection Applications. *Supercond. Sci. Technol.* **34,** 044001 (2021).

30. Mueller, A. *et al.* Time-Walk and Jitter Correction in SNSPDs at High Count Rates. *Appl. Phys. Lett.* **122,** 044001 (2023).

31. Hao, H. *et al.* A Compact Multi-Pixel Superconducting Nanowire Single-Photon Detector Array Supporting Gigabit Space-to-Ground Communications. *Light: Sci. Appl.* **13,** 25 (2024).

32. Marsili, F. *et al.* Efficient Single Photon Detection from 500nm to 5μm Wavelength. *Nano Lett.* **12,** 4799–4804 (2012).

33. Korneev, A., Korneeva, Y., Florya, I., Voronov, B. & Goltsman, G. NbN Nanowire Superconducting Single-Photon Detector for Mid-Infrared. *Physics Procedia* **36,** 72–76 (2012).

34. Wollman, E. E. *et al.* Kilopixel Array of Superconducting Nanowire Single-Photon Detectors. *Opt. Express* **27,** 35279 (2019).

35. McCaughan, A. N. *et al.* The Thermally Coupled Imager: A Scalable Readout Architecture for Superconducting Nanowire Single Photon Detectors. *Appl. Phys. Lett.* **121,** 102602 (2022).

36. Hadfield, R. H. Single-Photon Detectors for Optical Quantum Information Applications. *Nat. Photonics* **3,** 696–705 (2009).

37. Gol'tsman, G. N. *et al.* Picosecond Superconducting Single-Photon Optical Detector. *Appl. Phys. Lett.* **79,** 705–707 (2001).

38. Dorenbos, S. N. *et al.* Low Noise Superconducting Single Photon Detectors on Silicon. *Appl. Phys. Lett.* **93,** 131101 (2008).

39. Baek, B., Lita, A. E., Verma, V. & Nam, S. W. Superconducting a-W_xSi_{1-x} Nanowire Single-Photon Detector with Saturated Internal Quantum Efficiency from Visible to 1850nm. *Appl. Phys. Lett.* **98,** 251105 (2011).

40. Marsili, F. *et al.* Detecting Single Infrared Photons with 93% System Efficiency. *Nat. Photonics* **7,** 210–214 (2013).

41. Verma, V. B. *et al.* Superconducting Nanowire Single Photon Detectors Fabricated from an Amorphous $Mo_{0.75}Ge_{0.25}$ Thin Film. *Appl. Phys. Lett.* **105,** 022602 (2014).

42. Korneeva, Y. P. *et al.* Superconducting Single-Photon Detector Made of MoSi Film. *Supercond. Sci. Technol.* **27,** 095012 (2014).

43. Charaev, I. *et al.* Single-Photon Detection Using Large-Scale High-Temperature MgB_2 Sensors at 20 K. *Nat. Commun.* **15,** 3973 (2024).

44. Miller, A. J. *et al.* Compact Cryogenic Self-Aligning Fiber-to-Detector Coupling with Losses below One Percent. *Opt. Express* **19,** 9102 (2011).

45. Milostnaya, I. *et al.* Superconducting Single-Photon Detectors Designed for Operation at 1.55µm Telecommunication Wavelength. *J. Phys. Conf. Ser.* **43,** 1334 (2006).

46. Li, H. *et al.* Supercontinuum Single-Photon Detector Using Multilayer Superconducting Nanowires. *Photonics Res.* **7,** 1425 (2019).

47. Oripov, B. G. *et al.* A Superconducting Nanowire Single-Photon Camera with 400,000 Pixels. *Nature* **622,** 730–734 (2023).

48. Engel, A., Renema, J. J., Il'In, K. & Semenov, A. Detection Mechanism of Superconducting Nanowire Single-Photon Detectors. *Supercond. Sci. Technol.* **28** (2015).

49. Semenov, A., Engel, A., Hübers, H.-W., Il'in, K. & Siegel, M. Spectral Cut-off in the Efficiency of the Resistive State Formation Caused by Absorption of a Single-Photon in Current-Carrying Superconducting Nano-Strips. *Eur. Phys. J. B* **47,** 495–501 (2005).

50. Lusche, R. *et al.* Effect of Magnetic Field on the Photon Detection in Thin Superconducting Meander Structures. *Phys. Rev. B: Condens. Matter Mater. Phys.* **89,** 1–7 (2014).

51. Engel, A., Schilling, A., Il'In, K. & Siegel, M. Dependence of Count Rate on Magnetic Field in Superconducting Thin-Film TaN Single-Photon Detectors. *Phys. Rev. B: Condens. Matter Mater. Phys.* **86,** 1–4 (2012).

52. Bulaevskii, L. N., Graf, M. J., Batista, C. D. & Kogan, V. G. Vortex-Induced Dissipation in Narrow Current-Biased Thin-Film Superconducting Strips. *Phys. Rev. B* **83,** 144526 (2011).

53. Engel, A., Lonsky, J., Zhang, X. & Schilling, A. Detection Mechanism in SNSPD: Numerical Results of a Conceptually Simple, Yet Powerful Detection Model. *IEEE Trans. Appl. Supercond.* **25,** 1–7 (2015).

54. Engel, A. & Schilling, A. Numerical Analysis of Detection-Mechanism Models of Superconducting Nanowire Single-Photon Detector. *J. Appl. Phys.* **114,** 214501 (2013).

55. Zotova, A. N. & Vodolazov, D. Y. Intrinsic Detection Efficiency of Superconducting Nanowire Single Photon Detector in the Modified Hot Spot Model. *Supercond. Sci. Technol.* **27,** 125001 (2014).

56. Vodolazov, D. Y. Current Dependence of the Red Boundary of Superconducting Single-Photon Detectors in the Modified Hot-Spot Model. *Phys. Rev. B* **90,** 054515 (2014).

57. Kerman, A. J., Rosenberg, D., Molnar, R. J. & Dauler, E. A. Readout of Superconducting Nanowire Single-Photon Detectors at High Count Rates. *J. Appl. Phys.* **113,** 144511 (2013).

58. Liu, D.-K. *et al.* Nonlatching Superconducting Nanowire Single-Photon Detection with Quasi-Constant-Voltage Bias. *Appl. Phys. Express* **5,** 125202 (2012).

59. Brenner, M. W., Roy, D., Shah, N. & Bezryadin, A. Dynamics of Superconducting Nanowires Shunted with an External Resistor. *Phys. Rev. B* **85,** 224507 (2012).

60. Kerman, A. J. *et al.* Kinetic-Inductance-Limited Reset Time of Superconducting Nanowire Photon Counters. *Appl. Phys. Lett.* **88,** 2–5 (2006).

61. Smirnov, K. V. *et al.* Rise Time of Voltage Pulses in NbN Superconducting Single Photon Detectors. *Appl. Phys. Lett.* **109** (2016).

62. Holzman, I. & Ivry, Y. Superconducting Nanowires for Single-Photon Detection: Progress, Challenges, and Opportunities. *Adv. Quantum Technol.* **2,** 1800058 (2019).

63. Vetter, A. *et al.* Cavity-Enhanced and Ultrafast Superconducting Single-Photon Detectors. *Nano Lett.* **16,** 7085–7092 (2016).

64. Taylor, G. G. *et al.* Low-Noise Single-Photon Counting Superconducting Nanowire Detectors at Infrared Wavelengths up to 29μm. *Optica* **10,** 1672–1678 (2023).

65. Inderbitzin, K., Engel, A., Schilling, A., Il'in, K. & Siegel, M. An Ultra-Fast Superconducting Nb Nanowire Single-Photon Detector for Soft X-rays. *Appl. Phys. Lett.* **101,** 162601 (2012).

66. Guo, S. *et al.* High-Timing-Precision Detection of Single X-ray Photons by Superconducting Nanowires. *Natl. Sci. Rev.* **11,** nwad102 (2024).

67. Gourgues, R. *et al.* Superconducting Nanowire Single Photon Detectors Operating at Temperature from 4 to 7 K. *Opt. Express* **27,** 24601–24609 (2019).

68. Itzler, M. A. *et al.* Advances in InGaAsP-based Avalanche Diode Single Photon Detectors. *J. Mod. Opt.* **58,** 174–200 (2011).

69. You, L. Superconducting Nanowire Single-Photon Detectors for Quantum Information. *Nanophotonics* **9,** 2673–2692 (2020).

70. Lita, A. E., Miller, A. J. & Nam, S. W. Counting Near-Infrared Single-Photons with 95% Efficiency. *Opt. Express* **16,** 3032–3040 (2008).

71. Fukuda, D. *et al.* Titanium-Based Transition-Edge Photon Number Resolving Detector with 98% Detection Efficiency with Index-Matched Small-Gap Fiber Coupling. *Opt. Express* **19,** 870–875 (2011).

72. Chen, S. *et al.* Time-of-Flight Laser Ranging and Imaging at 1550nm Using Low-Jitter Superconducting Nanowire Single-Photon Detection System. *Appl. Opt.* **52,** 3241 (2013).

73. Guan, Y. *et al.* Lidar with Superconducting Nanowire Single-Photon Detectors: Recent Advances and Developments. *Opt. Lasers Eng.* **156,** 107102 (2022).

74. Kaifler, B., Geach, C., Büdenbender, H. C., Mezger, A. & Rapp, M. Measurements of Metastable Helium in Earth's Atmosphere by Resonance Lidar. *Nat. Commun.* **13,** 6042 (2022).

75. Ceccarelli, F. *et al.* Recent Advances and Future Perspectives of Single-Photon Avalanche Diodes for Quantum Photonics Applications. *Adv. Quantum Technol.* **4,** 2000102 (2021).

76. Lita, A. E., Reddy, D. V., Verma, V. B., Mirin, R. P. & Nam, S. W. Development of Superconducting Single-Photon and Photon-Number Resolving Detectors for Quantum Applications. *J. Lightwave Technol.* **40,** 7578–7597 (2022).

77. De Lucia, M. *et al.* Transition Edge Sensors: Physics and Applications. *Instruments* **8,** 47 (4 2024).

78. Chang, J. *et al.* Detecting Telecom Single Photons with 99.5-2.07+0.5% System Detection Efficiency and High Time Resolution. *APL Photonics* **6,** 036114 (2021).

79. Excelitas Technologies Corp. Timing Resolution Optimized Single Photon Counting Module. SPCM-AQRH-XX-TR. `https://www.excelitas.com/file-download/download/public/60596?filename=Excelitas_SPCM-AQRH-TR_Family_datasheet.pdf` (05/05/2025).

80. Korzh, B., Walenta, N., Lunghi, T., Gisin, N. & Zbinden, H. Free-Running InGaAs Single Photon Detector with 1 Dark Count per Second at 10% Efficiency. *Appl. Phys. Lett.* **104,** 081108 (2014).
81. Manenti, L. *et al.* Dark Counts in Optical Superconducting Transition-Edge Sensors for Rare-Event Searches. *Phys. Rev. Appl.* **22,** 024051 (2024).
82. Sanzaro, M. *et al.* Single-Photon Avalanche Diodes in a 0.16μm BCD Technology With Sharp Timing Response and Red-Enhanced Sensitivity. *IEEE J. Sel. Topics Quantum Electron.* **24,** 1–9 (2018).
83. Lamas-Linares, A. *et al.* Nanosecond-Scale Timing Jitter for Single Photon Detection in Transition Edge Sensors. *Appl. Phys. Lett.* **102,** 231117 (2013).
84. Scarcella, C., Boso, G., Ruggeri, A. & Tosi, A. InGaAs/InP Single-Photon Detector Gated at 1.3GHz With 1.5% Afterpulsing. *IEEE J. Sel. Topics Quantum Electron.* **21,** 17–22 (2015).
85. Kobayashi, R., Hattori, K., Inoue, S. & Fukuda, D. Development of a Fast Response Titanium-Gold Bilayer Optical TES With an Optical Fiber Self-Alignment Structure. *IEEE Trans. Appl. Supercond.* **29,** 1–5 (2019).
86. Xu, H., Pancheri, L., Betta, G.-F. D. & Stoppa, D. Design and Characterization of a p+/n-Well SPAD Array in 150nm CMOS Process. *Opt. Express* **25,** 12765–12778 (2017).
87. Lakew, B., Brasunas, J. C., Aslam, S. & Pugel, D. E. High-T_c, Transition-Edge Superconducting (TES) Bolometer on a Monolithic Sapphire Membrane—Construction and Performance. *Sens. Actuators, A* **114,** 36–40 (2004).
88. Jaha, R. *et al.* Kinetic Inductance and Jitter Dependence of the Intrinsic Photon Number Resolution in Superconducting Nanowire Single-Photon Detectors. arXiv: 2410.23162. (11/03/2024). Pre-published.
89. Zhang, J., Itzler, M. A., Zbinden, H. & Pan, J.-W. Advances in InGaAs/InP Single-Photon Detector Systems for Quantum Communication. *Light: Sci. Appl.* **4,** e286 (2015).
90. Lolli, L., Taralli, E. & Rajteri, M. Ti/Au TES to Discriminate Single Photons. *J. Low Temp. Phys.* **167,** 803–808 (2012).
91. TOF Range-Imaging Cameras (eds Remondino, F. & Stoppa, D.) (Springer Berlin Heidelberg, Berlin, Heidelberg, 2013).
92. Magnelli, B. *et al.* The IRAM/GISMO 2mm Survey in the COSMOS Field. *Astrophys. J.* **877,** 45 (2019).
93. Clem, J. R. & Berggren, K. K. Geometry-Dependent Critical Currents in Superconducting Nanocircuits. *Phys. Rev. B* **84** (2011).

94. Jönsson, M. *et al.* Current Crowding in Nanoscale Superconductors within the Ginzburg-Landau Model. *Phys. Rev. Appl.* **17,** 064046 (2022).

95. Akhlaghi, M. K., Atikian, H., Eftekharian, A., Loncar, M. & Majedi, A. H. Reduced Dark Counts in Optimized Geometries for Superconducting Nanowire Single Photon Detectors. *Opt. Express* **20,** 23610 (2012).

96. Henrich, D. *et al.* Detection Efficiency of a Spiral-Nanowire Superconducting Single-Photon Detector. *IEEE Trans. Appl. Supercond.* **23,** 2200405–2200405 (2013).

97. Charaev, I. *et al.* Current Dependence of the Hot-Spot Response Spectrum of Superconducting Single-Photon Detectors with Different Layouts. *Supercond. Sci. Technol.* **30,** 025016 (2017).

98. Baghdadi, R. *et al.* Enhancing the Performance of Superconducting Nanowire-Based Detectors with High-Filling Factor by Using Variable Thickness. *Supercond. Sci. Technol.* **34,** 035010 (2021).

99. Xiong, J.-M. *et al.* Reducing Current Crowding in Meander Superconducting Strip Single-Photon Detectors by Thickening Bends. *Supercond. Sci. Technol.* **35,** 055015 (2022).

100. Steinhauer, S., Gyger, S. & Zwiller, V. Progress on Large-Scale Superconducting Nanowire Single-Photon Detectors. *Appl. Phys. Lett.* **118,** 100501 (2021).

101. Cheng, R., Wang, S. & Tang, H. X. Superconducting Nanowire Single-Photon Detectors Fabricated from Atomic-Layer-Deposited NbN. *Appl. Phys. Lett.* **115,** 241101 (2019).

102. Knehr, E. *et al.* Nanowire Single-Photon Detectors Made of Atomic Layer-Deposited Niobium Nitride. *Supercond. Sci. Technol.* **32,** 125007 (2019).

103. Cheng, R., Wright, J., Xing, H. G., Jena, D. & Tang, H. X. Epitaxial Niobium Nitride Superconducting Nanowire Single-Photon Detectors. *Appl. Phys. Lett.* **117,** 132601 (2020).

104. Zhang, W. *et al.* Saturating Intrinsic Detection Efficiency of Superconducting Nanowire Single-Photon Detectors via Defect Engineering. *Phys. Rev. Appl.* **12,** 044040 (2019).

105. Esmaeil Zadeh, I. *et al.* Superconducting Nanowire Single-Photon Detectors: A Perspective on Evolution, State-of-the-Art, Future Developments, and Applications. *Appl. Phys. Lett.* **118,** 190502 (2021).

106. Zou, K. & Hu, X. Fabrication Development of High-Performance Fractal Superconducting Nanowire Single-Photon Detectors. *IEEE J. Sel. Topics Quantum Electron.,* 1–10 (2024).

107. Ward, B. W., Notte, J. A. & Economou, N. P. Helium Ion Microscope: A New Tool for Nanoscale Microscopy and Metrology. *J. Vac. Sci. Technol. B: Microelectron. Nanom. Struct. Process. Meas. Phenom.* **24,** 2871–2874 (2006).

108. Notte, J. *et al.* An Introduction to the Helium Ion Microscope. in *AIP Conference Proceedings* **931** (AIP, Gaithersburg, MD, 2007), 489–496.

109. Hlawacek, G., Veligura, V., Van Gastel, R. & Poelsema, B. Helium Ion Microscopy. *J. Vac. Sci. Technol. B Nanotechnol. Microelectron.: Mater. Process. Meas. Phenom.* **32,** 020801 (2014).

110. Allen, F. I. A Review of Defect Engineering, Ion Implantation, and Nanofabrication Using the Helium Ion Microscope. *Beilstein J. Nanotechnol.* **12,** 633–664 (2021).

111. Strohauer, S. *et al.* Site-Selective Enhancement of Superconducting Nanowire Single-Photon Detectors via Local Helium Ion Irradiation. *Adv. Quantum Technol.* **6,** 2300139 (2023).

112. Hortensius, H. L., Driessen, E. F. C. & Klapwijk, T. M. Possible Indications of Electronic Inhomogeneities in Superconducting Nanowire Detectors. *IEEE Trans. Appl. Supercond.* **23,** 2200705–2200705 (2013).

113. Noat, Y. *et al.* Unconventional Superconductivity in Ultrathin Superconducting NbN Films Studied by Scanning Tunneling Spectroscopy. *Phys. Rev. B* **88,** 014503 (2013).

114. Sacépé, B. *et al.* Disorder-Induced Inhomogeneities of the Superconducting State Close to the Superconductor-Insulator Transition. *Phys. Rev. Lett.* **101,** 157006 (2008).

115. Kirtley, J. R., Raider, S. I., Feenstra, R. M. & Fein, A. P. Spatial Variation of the Observed Energy Gap in Granular Superconducting NbN Films. *Appl. Phys. Lett.* **50,** 1607–1609 (1987).

116. Allman, M. S. *et al.* A Near-Infrared 64-Pixel Superconducting Nanowire Single Photon Detector Array with Integrated Multiplexed Readout. *Appl. Phys. Lett.* **106,** 192601 (2015).

117. Gaudio, R., op 't Hoog, K. P. M., Zhou, Z., Sahin, D. & Fiore, A. Inhomogeneous Critical Current in Nanowire Superconducting Single-Photon Detectors. *Appl. Phys. Lett.* **105,** 222602 (2014).

118. Kerman, A. J. *et al.* Constriction-Limited Detection Efficiency of Superconducting Nanowire Single-Photon Detectors. *Appl. Phys. Lett.* **90,** 101110 (2007).

119. Xu, G.-Z. *et al.* Superconducting Microstrip Single-Photon Detector with System Detection Efficiency over 90% at 1550nm. *Photonics Res.* **9,** 958 (2021).

120. Zhang, W.-J. *et al.* Sixteen-Channel Fiber Array-Coupled Superconducting Single-Photon Detector Array with Average System Detection Efficiency over 60% at Telecom Wavelength. *Opt. Lett.* **46,** 1049 (2021).

121. Zhang, X. *et al.* NbN Superconducting Nanowire Single-Photon Detector with 90.5% Saturated System Detection Efficiency and 14.7ps System Jitter at 1550nm Wavelength. *IEEE J. Sel. Topics Quantum Electron.* **28,** 1–8 (5: Lidars and Photonic Radars 2022).

122. Flaschmann, R. *et al.* The Dependence of Timing Jitter of Superconducting Nanowire Single-Photon Detectors on the Multi-Layer Sample Design and Slew Rate. *Nanoscale* **15,** 1086–1091 (2023).

123. Van der Pauw, L. J. A Method of Measuring the Resistivity and Hall Coefficient on Lamellae of Arbitrary Shape. *Philips Tech. Rev.* **20,** 220–224 (1958).

124. Miccoli, I., Edler, F., Pfnür, H. & Tegenkamp, C. The 100th Anniversary of the Four-Point Probe Technique: The Role of Probe Geometries in Isotropic and Anisotropic Systems. *J. Phys.: Condens. Matter* **27,** 223201 (2015).

125. Martinez, G. D. *et al.* Superconducting Nanowire Fabrication on Niobium Nitride Using Helium Ion Irradiation. arXiv: `2003.02898`. (06/15/2020). Pre-published.

126. Seifert, P. *et al.* A High-T_c van der Waals Superconductor Based Photodetector with Ultra-High Responsivity and Nanosecond Relaxation Time. *2D Mater.* **8,** 035053 (2021).

127. Merino, R. L. *et al.* Two-Dimensional Cuprate Nanodetector with Single Telecom Photon Sensitivity at T = 20K. *2D Mater.* **10,** 021001 (2023).

128. Sidorova, M. *et al.* Magnetoconductance and Photoresponse Properties of Disordered NbTiN Films. *Phys. Rev. B* **104,** 184514 (2021).

129. Semenov, A. *et al.* Optical and Transport Properties of Ultrathin NbN Films and Nanostructures. *Phys. Rev. B* **80,** 054510 (2009).

130. Banerjee, A. *et al.* Optical Properties of Refractory Metal Based Thin Films. *Opt. Mater. Express* **8,** 2072 (2018).

131. Zhang, L., You, L., Ying, L., Peng, W. & Wang, Z. Characterization of Surface Oxidation Layers on Ultrathin NbTiN Films. *Physica C* **545,** 1–4 (2018).

132. Korneeva, Y. P. *et al.* Optical Single-Photon Detection in Micrometer-Scale NbN Bridges. *Phys. Rev. Appl.* **9,** 64037 (2018).

133. Clem, J. R. & Kogan, V. G. Kinetic Impedance and Depairing in Thin and Narrow Superconducting Films. *Phys. Rev. B* **86,** 174521 (2012).

134. Il'in, K. *et al.* Current-Induced Critical State in NbN Thin-Film Structures. *J. Low Temp. Phys.* **151,** 585–590 (2008).

135. Il'in, K., Siegel, M., Semenov, A., Engel, A. & Hübers, H.-W. Critical Current of Nb and NbN Thin-film Structures: The Cross-section Dependence. *phys. status solidi (c)* **2,** 1680–1687 (2005).

136. Hortensius, H. L., Driessen, E. F. C., Klapwijk, T. M., Berggren, K. K. & Clem, J. R. Critical-Current Reduction in Thin Superconducting Wires Due to Current Crowding. *Appl. Phys. Lett.* **100,** 182602 (2012).

137. Henrich, D. *et al.* Geometry-Induced Reduction of the Critical Current in Superconducting Nanowires. *Phys. Rev. B* **86,** 144504 (2012).

138. Pearl, J. Current Distribution in Superconducting Films Carrying Quantized Fluxoids. *Appl. Phys. Lett.* **5,** 65–66 (1964).

139. Bartolf, H. Fluctuation Mechanisms in Superconductors (Springer Fachmedien Wiesbaden, Wiesbaden, 2016).

140. Tinkham, M. Introduction to Superconductivity 2 ed. 454 pp. (Dover Publ, Mineola, NY, 2004).

141. Alkemade, P. F. A. & van Veldhoven, E. Deposition, Milling, and Etching with a Focused Helium Ion Beam. in *Nanofabrication* (eds Stepanova, M. & Dew, S.) 275–300 (Springer, Vienna, 2012).

142. Li, N. *et al.* He Ion Irradiation Damage in Al/Nb Multilayers. *J. Appl. Phys.* **105,** 123522 (2009).

143. Shimizu, J., Yasuda, K. & Kinoshita, C. Formation Process of Defect Clusters in Copper and Nickel under Irradiation with Helium Ions. *J. Nucl. Mater.* **212–215,** 207–211 (1994).

144. Behrisch, R. & Eckstein, W. Sputtering by Particle Bombardment 1st ed. *Topics in Applied Physics* **110.** 507 pp. (Springer, Berlin, Heidelberg, 2007).

145. Ivry, Y. *et al.* Universal Scaling of the Critical Temperature for Thin Films near the Superconducting-to-Insulating Transition. *Phys. Rev. B* **90,** 214515 (2014).

146. Haviland, D. B., Liu, Y. & Goldman, A. M. Onset of Superconductivity in the Two-Dimensional Limit. *Phys. Rev. Lett.* **62,** 2180–2183 (1989).

147. Bezryadin, A., Lau, C. N. & Tinkham, M. Quantum Suppression of Superconductivity in Ultrathin Nanowires. *Nature* **404,** 971–974 (2000).

148. Ruhtinas, A. & Maasilta, I. J. Highly Tunable NbTiN Josephson Junctions Fabricated with Focused Helium Ion Beam. arXiv: `2303.17348`. (04/14/2023). Pre-published.

149. Engel, A. *et al.* Tantalum Nitride Superconducting Single-Photon Detectors with Low Cut-off Energy. *Appl. Phys. Lett.* **100,** 98–101 (2012).

150. Chockalingam, S. P., Chand, M., Jesudasan, J., Tripathi, V. & Raychaudhuri, P. Superconducting Properties and Hall Effect of Epitaxial NbN Thin Films. *Phys. Rev. B* **77,** 214503 (2008).

151. Radebaugh, R. Cryocoolers: The State of the Art and Recent Developments. *J. Phys.: Condens. Matter* **21,** 164219 (2009).

152. Strohauer, S. *et al.* Current Crowding–Free Superconducting Nanowire Single-Photon Detectors. *Sci. Adv.* **11,** eadt0502 (2025).

153. Meng, Y. *et al.* Fractal Superconducting Nanowires Detect Infrared Single Photons with 84% System Detection Efficiency, 1.02 Polarization Sensitivity, and 20.8ps Timing Resolution. *ACS Photonics* **9,** 1547–1553 (2022).

154. Frasca, S. *et al.* Determining the Depairing Current in Superconducting Nanowire Single-Photon Detectors. *Phys. Rev. B* **100,** 054520 (2019).

155. Semenov, A. *et al.* Asymmetry in the Effect of Magnetic Field on Photon Detection and Dark Counts in Bended Nanostrips. *Phys. Rev. B* **92,** 174518 (2015).

156. Zhang, L. *et al.* Characterization of Superconducting Nanowire Single-Photon Detector with Artificial Constrictions. *AIP Adv.* **4,** 067114 (2014).

157. Zhang, X. *et al.* Geometric Origin of Intrinsic Dark Counts in Superconducting Nanowire Single-Photon Detectors. *Superconductivity* **1,** 100006 (2022).

158. Wang, Y.-Z. *et al.* Free-Space Coupled, Large-Active-Area Superconducting Microstrip Single-Photon Detector for Photon-Counting Time-of-Flight Imaging. *Appl. Opt.* **63,** 3130 (2024).

159. Kahl, O. *et al.* Waveguide Integrated Superconducting Single-Photon Detectors with High Internal Quantum Efficiency at Telecom Wavelengths. *Sci. Rep.* **5,** 10941 (2015).

160. Shibata, H., Shimizu, K., Takesue, H. & Tokura, Y. Superconducting Nanowire Single-Photon Detector with Ultralow Dark Count Rate Using Cold Optical Filters. *Appl. Phys. Express* **6,** 072801 (2013).

161. Shibata, H., Honjo, T. & Shimizu, K. Quantum Key Distribution over a 72 dB Channel Loss Using Ultralow Dark Count Superconducting Single-Photon Detectors. *Opt. Lett.* **39,** 5078 (2014).

162. Strohauer, S. *et al.* Origin of Performance Enhancement of Superconducting Nanowire Single-Photon Detectors by He-ion Irradiation. *APL Quantum* **2,** 026131 (2025).

163. Batson, E. *et al.* Effects of Helium Ion Exposure on the Single-Photon Sensitivity of MgB_2 and NbN Detectors. *IEEE Trans. Appl. Supercond.* **34,** 0600906 (2024).

164. Raineri, V., Coffa, S., Szilágyi, E., Gyulai, J. & Rimini, E. He-Vacancy Interactions in Si and Their Influence on Bubble Formation and Evolution. *Phys. Rev. B* **61,** 937–945 (2000).

165. Livengood, R., Tan, S., Greenzweig, Y., Notte, J. & McVey, S. Subsurface Damage from Helium Ions as a Function of Dose, Beam Energy, and Dose Rate. *J. Vac. Sci. Technol. B: Microelectron. Nanom. Struct.* **27,** 3244 (2009).

166. Abrams, K. J. *et al.* Helium Irradiation Effects in Polycrystalline Si, Silica, and Single Crystal Si. *J. Appl. Phys.* **111,** 083527 (2012).

167. Ziegler, J. F., Ziegler, M. D. & Biersack, J. P. SRIM – The Stopping and Range of Ions in Matter (2010). *Nucl. Instrum. Methods Phys. Res. B: Beam Interact. Mater. At.* **268,** 1818–1823 (2010).

168. Oya, G.-i. & Onodera, Y. Transition Temperatures and Crystal Structures of Single-Crystal and Polycrystalline NbN_x Films. *J. Appl. Phys.* **45,** 1389–1397 (1974).

169. Brauer, G. & Jander, J. Die Nitride des Niobs. *Z. Anorg. Allg. Chem.* **270,** 160–178 (1952).

170. Yamamoto, T., Kikkawa, S., Takahashi, M., Miyamoto, Y. & Kanamaru, F. High Pressure Synthesis of B1-type Solid Solutions $Nb_{1-x}M_xN$ (M = Ga, Ti). *Physica C* **185–189,** 2719–2720 (1991).

171. Custer, J. S. *et al.* Density of Amorphous Si. *Appl. Phys. Lett.* **64,** 437–439 (1994).

172. Yoon, H.-S., Kim, C.-S., Lee, H.-T. & Ahn, S.-H. Advanced Scanning Paths for Focused Ion Beam Milling. *Vacuum* **143,** 40–49 (2017).

173. Bachmann, M. D. Manipulating Anisotropic Transport and Superconductivity by Focused Ion Beam Microstructuring (Springer International Publishing, Cham, 2020).

174. Kajita, S., Yoshida, N., Yoshihara, R., Ohno, N. & Yamagiwa, M. TEM Observation of the Growth Process of Helium Nanobubbles on Tungsten: Nanostructure Formation Mechanism. *J. Nucl. Mater.* **418,** 152–158 (2011).

175. Snoeks, E., Polman, A. & Volkert, C. A. Densification, Anisotropic Deformation, and Plastic Flow of SiO_2 during MeV Heavy Ion Irradiation. *Appl. Phys. Lett.* **65,** 2487–2489 (1994).

176. Volkert, C. A. Stress and Plastic Flow in Silicon During Amorphization by Ion-Bombardment. *MRS Proc.* **157,** 635 (1989).

177. Volkert, C. A. Density Changes and Viscous Flow during Structural Relaxation of Amorphous Silicon. *J. Appl. Phys.* **74,** 7107–7113 (1993).

178. Volkert, C. A. Stress and Plastic Flow in Silicon during Amorphization by Ion Bombardment. *J. Appl. Phys.* **70,** 3521–3527 (1991).

179. Iosad, N. N. *et al.* Optimization of RF- and DC-sputtered NbTiN Films for Integration with Nb-based SIS Junctions. *IEEE Trans. Appiled Supercond.* **9,** 1716–1719 (1999).

180. Cecil, T. W., Weikle, R. M., Kerr, A. R. & Lichtenberger, A. W. Investigation of NbTiN Thin Films and AlN Tunnel Barriers With Ellipsometry for Superconducting Device Applications. *IEEE Trans. Appl. Supercond.* **17,** 3525–3528 (2007).

181. Yamamori, H., Sasaki, H. & Kohjiro, S. Preparation of Overdamped NbTiN Josephson Junctions with Bilayered Ti–TiN Barriers. *J. Appl. Phys.* **108,** 113904 (2010).

182. Shan, W., Sekimoto, Y. & Noguchi, T. Microwave Loss of DC Sputtered NbTiN Microstrip Lines. *Jpn. J. Appl. Phys.* **54,** 090303 (2015).

183. Karimi, A., La Grange, D., Goebbels, N. & Santana, A. Structural and Mechanical Properties of $Nb_{1-x}Ti_xN$ Thin Films Deposited by RF Magnetron Sputtering. *Thin Solid Films* **607,** 14–24 (2016).

184. EerNisse, E. P. Viscous Flow of Thermal SiO_2. *Appl. Phys. Lett.* **30,** 290–293 (1977).

185. Xu, T. *et al.* Enhancing SNSPDs Detection Efficiency via Suspended SiO_2 Membrane. *Appl. Phys. Lett.* **123,** 082602 (2023).

186. Stockhausen, A. *et al.* Adjustment of Self-Heating in Long Superconducting Thin Film NbN Microbridges. *Supercond. Sci. Technol.* **25,** 035012 (2012).

187. Sidorova, M., Semenov, A. D., Hübers, H.-W., Gyger, S. & Steinhauer, S. Phonon Heat Capacity and Self-Heating Normal Domains in NbTiN Nanostrips. *Supercond. Sci. Technol.* **35,** 105005 (2022).

188. Xu, T. *et al.* Effect of Buffer Layer on Thermal Recovery of Superconducting Nanowire Single-Photon Detector. *Supercond. Sci. Technol.* **34,** 074002 (2021).

189. Dane, A. *et al.* Self-Heating Hotspots in Superconducting Nanowires Cooled by Phonon Black-Body Radiation. *Nat. Commun.* **13,** 5429 (2022).

190. Xu, G.-z. *et al.* Millimeter-Scale Active Area Superconducting Microstrip Single-Photon Detector Fabricated by Ultraviolet Photolithography. *Opt. Express* **31,** 16348 (2023).

191. Zink, B. L., Pietri, R. & Hellman, F. Thermal Conductivity and Specific Heat of Thin-Film Amorphous Silicon. *Phys. Rev. Lett.* **96,** 055902 (2006).

192. Thompson, J. C. & Younglove, B. A. Thermal Conductivity of Silicon at Low Temperatures. *J. Phys. Chem. Solids* **20,** 146–149 (1961).

193. Kozorezov, A. G. *et al.* Fano Fluctuations in Superconducting-Nanowire Single-Photon Detectors. *Phys. Rev. B* **96,** 054507 (2017).

194. Catelani, G. & Pekola, J. P. Using Materials for Quasiparticle Engineering. *Mater. Quantum Technol.* **2,** 013001 (2022).

195. Krinner, S. *et al.* Engineering Cryogenic Setups for 100-Qubit Scale Superconducting Circuit Systems. *EPJ Quantum Technol.* **6** (2019).

196. Gardiner, C. W. & Zoller, P. Quantum Noise: A Handbook of Markovian and Non-Markovian Quantum Stochastic Methods with Applications to Quantum Optics. *Springer Ser. Synergetics* **16,** xxii, 449 p. (2004).

197. Hu, C. Modern Semiconductor Devices for Integrated Circuits. 351 pp. (Prentice Hall, New Jersey, 2010).

198. Pires, R. G., Dickstein, R. M., Titcomb, S. L. & Anderson, R. L. Carrier Freezeout in Silicon. *Cryogenics* **30,** 1064–1068 (1990).

199. Saks, N. S. & Nordbryhn, A. Time Dependence of Depletion Region Formation in Phosphorus-doped Silicon MOS Devices at Cryogenic Temperatures. *J. Appl. Phys.* **50,** 6962–6968 (1979).

200. Lee, S., Hashisaka, M., Akiho, T., Kobayashi, K. & Muraki, K. Cryogenic GaAs High-Electron-Mobility-Transistor Amplifier for Current Noise Measurements. *Rev. Sci. Instrum.* **92,** 023910 (2021).

201. Macom. GaAs SPDT Non-Reflective Switch DC - 26.5 GHz. MASW-011107-DIE. `https://cdn.macom.com/datasheets/MASW-011107-DIE.pdf` (04/27/2025).

202. Meng, Y. *et al.* Fractal Superconducting Nanowires Detect Infrared Single Photons with 84% System Detection Efficiency, 1.02 Polarization Sensitivity, and 20.8ps Timing Resolution. *ACS Photonics* **9,** 1547–1553 (2022).

Acknowledgments

As this journey comes to an end, I wish to express my profound gratitude to everyone who supported me throughout my years at the Walter Schottky Institute and beyond.

First and foremost, I am deeply grateful to Prof. Dr. Jonathan Finley for providing me the opportunity to work on the fascinating field of single-photon detectors. Your enthusiasm for new ideas, combined with the scientific and financial freedom you offered, created a fertile ground for exciting results and novel research directions. I particularly value your contagious excitement and expertise when discussing unexpected findings, the warm atmosphere, and your open-door policy that made you always approachable and supportive. Your mentorship has not only shaped this research but also my development as a scientist.

I am particularly thankful to Prof. Dr. Stefan Filipp for kindly agreeing to referee this dissertation.

My sincere appreciation goes to Prof. Dr. Kai Müller for your valuable mentorship during the past six years. Your enthusiasm for our SNSPD team's discoveries consistently maintained our motivation, even during challenging periods when equipment failed or faced extended downtime. I am very grateful for your generous financial support that not only enabled us to pursue our experimental visions but also allowed me to present our findings at more international conferences than I could have anticipated.

A special acknowledgment is due to Fabian Wietschorke for your outstanding work and perseverance throughout these years. I am genuinely grateful that you joined me on this exciting journey of He ion irradiation of SNSPDs, beginning with your Master thesis and continuing with your PhD research. Your presence made the countless long days and nights in the laboratory considerably more enjoyable, and your contributions significantly enhanced the success of this research. I wish you continued excitement and success as you explore new frontiers in He ion irradiation of SNSPDs, and most importantly, that you maintain your positive spirit!

I would also like to express my gratitude to my other students, Noah Ploch and Prahlad Iyengar. Thank you for your significant contributions to the foundation of this work by joining the development of the transport measurement setup and simulations.

For valuable collaborations and enlightening scientific discussions, I am indebted to many colleagues. In particular, I am grateful to Markus Döblinger and Steffen Schmidt for performing the TEM measurements presented in this work, and to Rudolf Gross and Matthias Althammer for your insightful discussions and contributions to interpreting the superconducting physics involved. My research was also enriched by successful collaborations with Sridhar Majety, Pranta Saha, and Marina Radulaski at UC Davis, as well as Jan Spallek and Alexander Regnat at kiutra GmbH—thank you all for the productive projects we accomplished together.

The work presented in this dissertation was greatly enriched by the entire Team SNSPD: Fabian Wietschorke, Stefanie Grotowski, Lucio Zugliani, Christian Schmid, Björn Jonas, Alessandro Palermo, Hadrien Le Petit, Damjan Pecijareski, Johannes Reiprich, Mirco Metz, Sven Ernst, Simone Spedicato, and David Busse. Thank you for your assistance with fabrication processes, problem-solving in the laboratory, stimulating discussions during lunch and coffee breaks, and occasional pizza & beer nights when measurement days got long—all of which contributed significantly to the success of this project.

The daily work environment was made more enjoyable by my office mates: William Rauhaus, Stefan Kresta, Frederik Bopp, Friedrich Sbresny, and Carolin Calcagno. Thank you for the scientific discussions, rating matplotlib color schemes, spontaneous snack exchanges, and refreshing dives into the Isar!

Special thanks to Sonya Gzyl for your exceptional organization of the IMPRS-QST program. Your efforts created valuable networking opportunities and seminars that significantly enriched my PhD experience beyond the Walter Schottky Institute.

Several individuals merit explicit acknowledgment: Jonathan Becker for providing a strong start in the laboratory; Sergej Fust for the great time when sharing lab and transport setup; Jakob Wierzbowski for dragging me from a coffee room encounter to joining WSI; Hubert Riedl and Adolf Ziegltrum, the technicians and magicians whose invaluable input ranged from laboratory constructions to kitchen assembly; Daniela Huber for being the most supportive secretary imaginable; Claudia Paulus for maintaining best conditions in the OT and the clean room; Sergey Zherebtsov for maintaining the HIM, a crucial instrument for this research; Johannes Seitz and Nick Schröder for their great work in the engineering workshop; and all other WSI members for their continuous support and the warm atmosphere over the past six years. Thanks to Fabian Wietschorke, Stefan Kresta, Michelle Lienhart, Tobias Schreitmüller, and Hyowon Jeong for being wonderful travel companions at the conferences in Yokohama and San Francisco!

This dissertation has been significantly improved by the careful reviews of Christian Lenz, Friedrich Sbresny, Fabian Wietschorke, Dominik Irber, Valentina Faihs, and Carolin Calcagno. Thank you all for your invaluable feedback.

Beyond the academic realm, I would like to thank my friends who have shared mountain adventures, cooking and music sessions, and other experiences with me. Your presence during both the memorable highlights and challenging moments of life has been invaluable. Special thanks go to Christian Lenz, Tobias Grosch, Jennifer Schäfer-Jasinski, and Dominik Irber. I also wish to recognize Florian Burger, Timo Sommer, Fabian Becker, Marco Dembecki, Andreas Thurn, William Rauhaus, Fabian Wietschorke, Stefanie Grotowski, Manuel Rieger, Lina Todenhagen, Friedrich Sbresny, and Carolin Calcagno for being exceptional colleagues and friends. To Daniel Meyer, Angela Knoll, Caroline d'Anglade, Axel Humbert, and Julia Martin—thank you for enriching these recent years with your friendship and support. I am also grateful to Valentina Faihs for brightening the final months of this journey.

I would also like to thank Lutz Blöser, my grandfather Florian Kuschner, and my mother Monika Strohauer for fostering my early interest in physics and encouraging the curiosity that has guided my scientific journey.

For technical assistance, I am grateful to the generative AI tools Claude.ai, ChatGPT, and Perplexity.ai, which helped with structuring and revising this dissertation, assisted with developing analysis scripts, facilitated literature research, and contributed to the creation of the artistic background for the quotation page.

I gratefully acknowledge support from the German Federal Ministry of Education and Research (BMBF) via the funding program "Photonics Research Germany" (projects MOQUA (13N14846) and MARQUAND (BN106022)) and the funding program "Quantum technologies – from basic research to market" (projects PhotonQ (13N15760), SPINNING (13N16214), QPIS (16K1SQ033), QPIC-1 (13N15855) and SEQT (13N15982)), as well as from the German Research Foundation (DFG) under Germany's Excellence Strategy EXC-2111 (390814868) with the projects PQET (INST 95/1654-1) and MQCL (INST 95/1720-1). This research is part of the "Munich Quantum Valley", supported by the Bavarian state government through the "Hightech Agenda Bayern Plus".

I am also thankful to the piano in ZNN that transformed tedious cryostat waiting hours into delightful musical interludes. Credit to Prof. Dr. Martin Brandt for donating it and Prof. Dr. Alexander Holleitner for giving it a home in the seminar room.

Finally, my deepest gratitude goes to my family for their unconditional support throughout my life, especially during these recent years. Thank you, Monika Strohauer and Helmut Strohauer, for your unwavering presence and support.

List of publications

This thesis is based on the following published manuscripts:

1. **Strohauer, S.,** Wietschorke, F., Döblinger, M., Schmid, C., Grotowski, S., Zugliani, L., Jonas, B., Müller, K. & Finley, J. J. Origin of Performance Enhancement of Superconducting Nanowire Single-Photon Detectors by He-ion Irradiation. *APL Quantum* **2,** 026131 (2025).
2. **Strohauer, S.,** Wietschorke, F., Schmid, C., Grotowski, S., Zugliani, L., Jonas, B., Müller, K. & Finley, J. J. Current Crowding–Free Superconducting Nanowire Single-Photon Detectors. *Sci. Adv.* **11,** eadt0502 (2025).
3. **Strohauer, S.,** Wietschorke, F., Zugliani, L., Flaschmann, R., Schmid, C., Grotowski, S., Müller, M., Jonas, B., Althammer, M., Gross, R., Müller, K. & Finley, J. J. Site-Selective Enhancement of Superconducting Nanowire Single-Photon Detectors via Local Helium Ion Irradiation. *Adv. Quantum Technol.* **6,** 2300139 (2023).

Additional publications to which I have contributed:

4. Grotowski, S., Zugliani, L., Jonas, B., Flaschmann, R., Schmid, C., **Strohauer, S.,** Wietschorke, F., Bruckmoser, N., Müller, M., Althammer, M., Gross, R., Müller, K. & Finley, J. Optimizing the Growth Conditions of Superconducting MoSi Thin Films for Single Photon Detection. *Sci. Rep.* **15,** 2438 (2025).
5. Zugliani, L., Schmid, C., Wietschorke, F., Jonas, B., Spedicato, S., **Strohauer, S.,** Grotowski, S., Flaschmann, R., Müller, M., Althammer, M., Gross, R., Finley, J. & Müller, K. Tailoring Superconducting Nanowire Single-Photon Detectors for Quantum Technologies. in *2023 IEEE Globecom Workshops* (2023), 1051–1056.
6. Flaschmann, R., Schmid, C., Zugliani, L., **Strohauer, S.,** Wietschorke, F., Grotowski, S., Jonas, B., Müller, M., Althammer, M., Gross, R., Finley, J. J. & Müller, K. Optimizing the Growth Conditions of Al Mirrors for Superconducting Nanowire Single-Photon Detectors. *Mater. Quantum Technol.* **3,** 035002 (2023).

7. Majety, S., **Strohauer, S.,** Saha, P., Wietschorke, F., Finley, J. J., Müller, K. & Radulaski, M. Triangular Quantum Photonic Devices with Integrated Detectors in Silicon Carbide. *Mater. Quantum Technol.* **3,** 015004 (2023).

8. Flaschmann, R., Zugliani, L., Schmid, C., Spedicato, S., **Strohauer, S.,** Wietschorke, F., Flassig, F., Finley, J. J. & Müller, K. The Dependence of Timing Jitter of Superconducting Nanowire Single-Photon Detectors on the Multi-Layer Sample Design and Slew Rate. *Nanoscale* **15,** 1086–1091 (2023).

9. Flassig, F., Flaschmann, R., Kainz, T., Ernst, S., **Strohauer, S.,** Schmid, C., Zugliani, L., Müller, K. & Finley, J. J. Automated, Deep Reactive Ion Etching Free Fiber Coupling to Nanophotonic Devices. in *Quantum Sensing and Nano Electronics and Photonics XVIII* (eds Razeghi, M., Khodaparast, G. A. & Vitiello, M. S.) (SPIE, San Francisco, United States, 2022), 54.

Declaration of authorship

I declare that I have composed this PhD thesis independently, using only the stated sources and aids. The work has not been submitted, in whole or in part, for any other degree or professional qualification.

Munich, May 8, 2025 Stefan Strohauer